Hardin, R.A., and Beckermann, C., "Effect of Cooling Rate and Microporosity on Mechanical Performance of a High Strength Steel," in Proceedings of the 70th SFSA Technical and Operating Conference, Paper No. 5.2, Steel Founders' Society of America, Chicago, IL, 2016.

Effect of Cooling Rate and Microporosity on Mechanical Performance of a High Strength Steel

Richard A. Hardin and Christoph Beckermann

Department of Mechanical and Industrial Engineering
The University of Iowa, Iowa City, 52242

Abstract

Tensile and microscopy measurements for high strength steel specimens show that its mechanical performance and ductility are dependent upon porosity level and cooling rate during solidification. Even porosity levels below 0.1% in the steel considered here will impact ductility. The data also show that if an elongation to failure of 10% or greater is desired, the porosity should be limited to 0.04% or less. Tensile specimens were taken from castings produced over a range of solidification cooling rates from 0.03 to 4 °C/s. The data for cooling rate and ductility indicate that a cooling rate threshold of at least 0.08 °C/s results in optimal ductility and an elongation of 10% or greater. It is shown that higher cooling rate results in a finer microstructure with secondary dendrite arm spacing (SDAS) less than 100 μm. This contributes to the better ductility. Micro X-Ray computed tomography (CT) performed on four specimens is used to visualize the microporosity distributions. Analysis of this CT data gives the porosity in the fractured regions of the specimen as 30% to 63% greater than the overall average porosity. CT data shows that ductility increases with decreasing porosity. An elongation predictor using cooling rate is proposed for use in casting simulation for this high strength steel to guide casting process design. To provide a means for increasing cooling rates and better control of solidification conditions, temperature dependent chill and mold material properties are determined by inverse modeling of casting experiments. These materials are: solid steel chills, molds made from steel shot, steel shot mixed 50/50 by volume with chromite sand, and steel shot mixed 50/50 by volume with zircon sand, and silica sand mold for baseline comparison. A study is performed comparing the ability of these mold materials to increase ductility. It is found that at the mid-thickness of a 2" thick section for this steel, the elongation to failure predicted for the mold materials are: 2.5% for silica mold, 10% for solid steel chill, 8.75% for steel shot mold, and 8% for the steel shot/sand mixes.

Introduction

This paper investigates variables that influence the mechanical performance of a high strength steel. Previous work has shown that porosity and microstructural characteristics resulting from increasing solidification rate affect the mechanical properties and ductility of cast metals [1-7]. Since porosity and cooling rate are quantities that can be predicted by casting simulation, the goal of the present work was to investigate whether these or some other result from casting simulation could allow the prediction of mechanical performance of cast high strength steels.

Van Aken et al. [1] have shown how the measured ductility of high strength steels is reduced by porosity, inclusions and hydrogen. They propose that the adverse effect of porosity on ductility of high strength steels is explained by notch sensitivity. Under static and dynamic loading materials yield first at the root of a notch or stress concentration feature like a pore (as shown in Figure 1 (a)) described using an elastic stress concentration factor K_t giving a peak stress at the notch root. In fatigue analysis calculations for materials with a notch [8], higher yield strength steels are notch sensitive resulting in fatigue notch factors K_f that are closer to K_t than lower yield strength steels. Softer lower strength materials yield at lower stresses σ_y and blunt the effect of the notch by lowering the stress from plastic yielding and distributing the stress over a volume of the material as shown by the dashed curve in Figure 1(a). As a result, for softer materials the stress used in the fatigue life calculation is lower than the stress that would result from using the elastic concentration factor K_t. Calculated fatigue lives can be longer for a given notch or feature for softer materials. For high strength steels, their fatigue notch factors can approach the value of K_t, and they are said to be fully notch sensitive if $K_f = K_t$. The dependency of ductility properties on microporosity for high strength steels also arises from incapacity to tolerate and blunt the effect of material failure at micropores and forming microcracks. Note there is also a notch size effect, since the volume of material subject to high stress concentration will increase with notch size as seen in Figure 1 (b). In the figure there is a feature that produces the same maximum stress at the notch root σ_{max} for large and small notches. The larger volume of material subject to high stress results in a greater probability that the material will fail. As a result, this notch size effect is included when calculating Neuber fatigue notch factors that are used in strain-life calculations, giving lower fatigue lives for larger notches at a given stress level. These concepts were used to predict fatigue life in 8630 quenched and tempered steel with relatively large porosity levels ranging from 8 to 21 percent porosity [9]. All equations

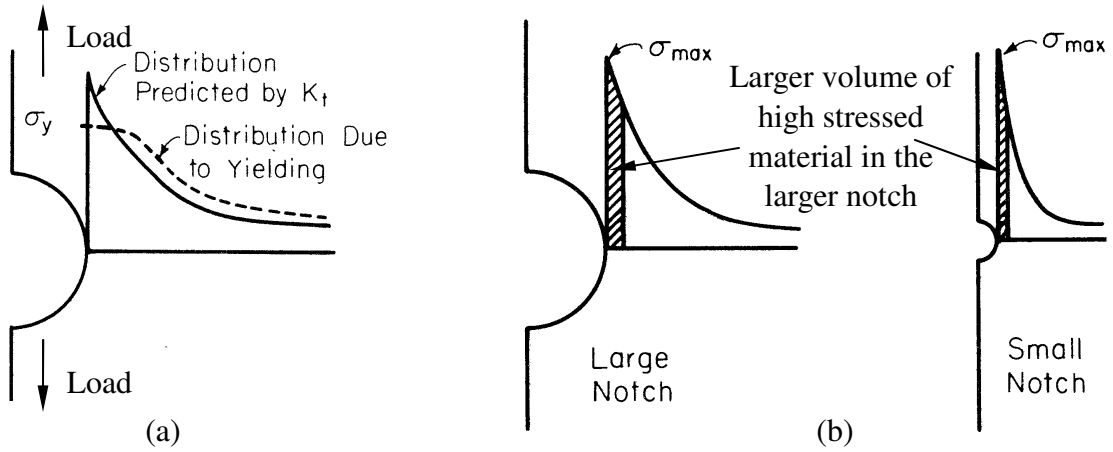

Figure 1 (a) Stress distribution without yielding (solid curve) and stress distribution with yielding (dashed curve) resulting in the notch blunting effect for lower yield strength materials. (b) Effect of notch size on increasing the volume of material subject to higher stress and an in crease in the probability of failure (graphics from [8]).

for applying strain-life fatigue calculations in the presence of notches are given in the reference. The effect of porosity on tensile behavior of steel has been simulated using a ductile failure micromechanical-based model to predict the ductile fracture of cast steel with centerline porosity [2]. Here the porous metal plasticity model was used as implemented in the commercial finite element analysis software *ABAQUS*, and the steel considered is ASTM A216 Grade WCB steel. Note this steel has about one third of the tensile strength of the steel studied here. The porous metal plasticity model parameters were determined first for the steel without porosity by matching the measured and simulated tensile test results. Then the porosity distribution in each specimen was determined by quantitative radiography with average porosity levels ranging from 0.1 to 0.27 % in the gage section. The porosity determined for each specimen was transferred to stress models. The predicted elongations to failure ranging from 12% to 20% were in agreement with measurements demonstrating that the effect of centerline porosity on tensile properties can be realistically simulated.

Local solidification conditions and cooling rate affects mechanical properties in castings. This leads to variations in mechanical properties throughout cast components which are not typically considered in their design. For aluminum alloys there is strong evidence that tensile and ductility properties can be improved through higher solidification cooling rates [3-6]. Higher cooling rates in aluminum alloy castings produce finer microstructures with smaller secondary dendrite arm spacing (SDAS) and refined eutectic particles resulting in ductility and tensile property improvements in A356 and A357 alloys [3,4]. Ceschini et al. [4] present equations for predicting yield strength *YS*, ultimate strength *UTS* and elongation *EL%* as functions of hardness, defect area on fracture surface, area of eutectic Si particles and SDAS. They found that yield strength depended primarily on hardness, while elongation and ultimate strength depended strongly on SDAS and area of eutectic particles. Ceschini et al. envision “co-engineered” design of cast aluminum alloy components using combined casting and structural simulation. Similarly, equations are provided in [6] for *YS*, *UTS* and *EL%* as functions of SDAS. For a zinc-based alloy Turhal and Savaskan [7] show that as SDAS decreases all tensile properties increase, but *EL%* in particular is strongly affected by SDAS.

In the paper that follows, the high strength cast steel and the experiments and trials used to produce material for this study are described first. Tensile and microscopy measurements for high strength steel specimens are analyzed. Ductility is determined to be a difficult mechanical property to achieve for this steel, and limits its performance. The most important variables affecting ductility are identified. Variables that can be computed using casting simulation such as microporosity and cooling rate are of particular interest. Effects of these variables on ductility are analyzed in detail. Micro X-ray computed tomography results for four tensile specimens are presented and compared with their tensile properties. A ductility predictor for this high strength steel is developed based on cooling rate. Measured and predicted ductility results are compared. Lastly, the results of an investigation into use of chills and steel shot mold materials for increasing solidification cooling rates and improving ductility is provided.

Experiments and Trials for Production of Cast High Strength Steel Specimens

The high strength cast steel used in the current study has the following threshold properties: yield strength 180 to 185 ksi (1241 to 1276 MPa), tensile strength 230 to 240 ksi (1586 to 1655 MPa), elongation 12%, and Charpy impact test at -40 °F of 36 to 40 ft-lbs. The chemistry of the steel is given in Table I. A heat treatment for this steel was developed by the Missouri University of Science and Technology (MS&T) to optimize for the relatively high ductility desired from this material considering its high strength. As reported by Van Aken et al. [1], "the best ductility was obtained using the following heat treatment: a hydrogen bake at 600°F (315°C) for 7 hours, a nonstandard normalization at 2100°F (1149°C) for 2 hours with an oil or water quench to produce a martensitic microstructure, an intermediate temper at 1200°F (649°C) for 4 hours, an austenitization at 1900°F (1038°C) for 1 hour with a water quench, and a temper at either 375°F (190°C) for 4 hours or 380°F (193°C) for 5 hours."

Table I Steel chemistry cast in this work

	Composition by Element (wt%)												
	C	Cr	Cu	Mn	Mo	N	Ni	O	P	S	Si	V	W
Min	0.24	1.5	-	0.65	0.3	-	0.9	-	-	-	0.85	0.05	0.8
Max	0.28	3	0.5	0.85	0.55	0.005	1.2	0.005	0.01	0.01	1.1	0.3	1
Aim	0.25	2.6	LAP	0.75	0.4	LAP	1	LAP	LAP	LAP	1	0.1	0.9

The data presented in this paper was generated using four casting rigging configurations. One configuration was produced in the foundry of the Metals Casting Group at the University of Alabama-Birmingham (UAB). This configuration produced a range of solidification cooling rates from 0.1 to 4 °C/s in the specimen material. The 28 specimens from this casting configuration are by far the largest number of specimens analyzed in this study. As shown in Figure 2, the configuration is a vertical wedge-shaped casting with a chill is positioned at the base of the casting. In addition to chilled material, cast material was produced without a chill at UAB. This wedge casting is 30 mm thick at the chill contact tapering to 50 mm thick at the riser neck, 203 mm from the chill. The casting weighs about 33 pounds (15 kg). A 80 mm x 100 mm x 156 mm copper chill was used. Note that virtual/simulated thermocouple (TC) positions are indicated in Figure 2. In one of the chilled castings, two TCs were placed in the sand mold and one in the chill at the locations indicated in Figure 2. These temperature measurements were performed at UAB using K-type thermocouples, and provided data to confirm the accuracy of simulation temperature predictions for this configuration. UAB also performed porosity measurements to compare with the porosity predictions. One specimen from a chilled wedge casting nearest the chill location was scanned using computed x-ray tomography to provide volumetric porosity data as described in the results section. The 28 tensile specimens and their data from this configuration will be referred to as "wedge" specimens and data.

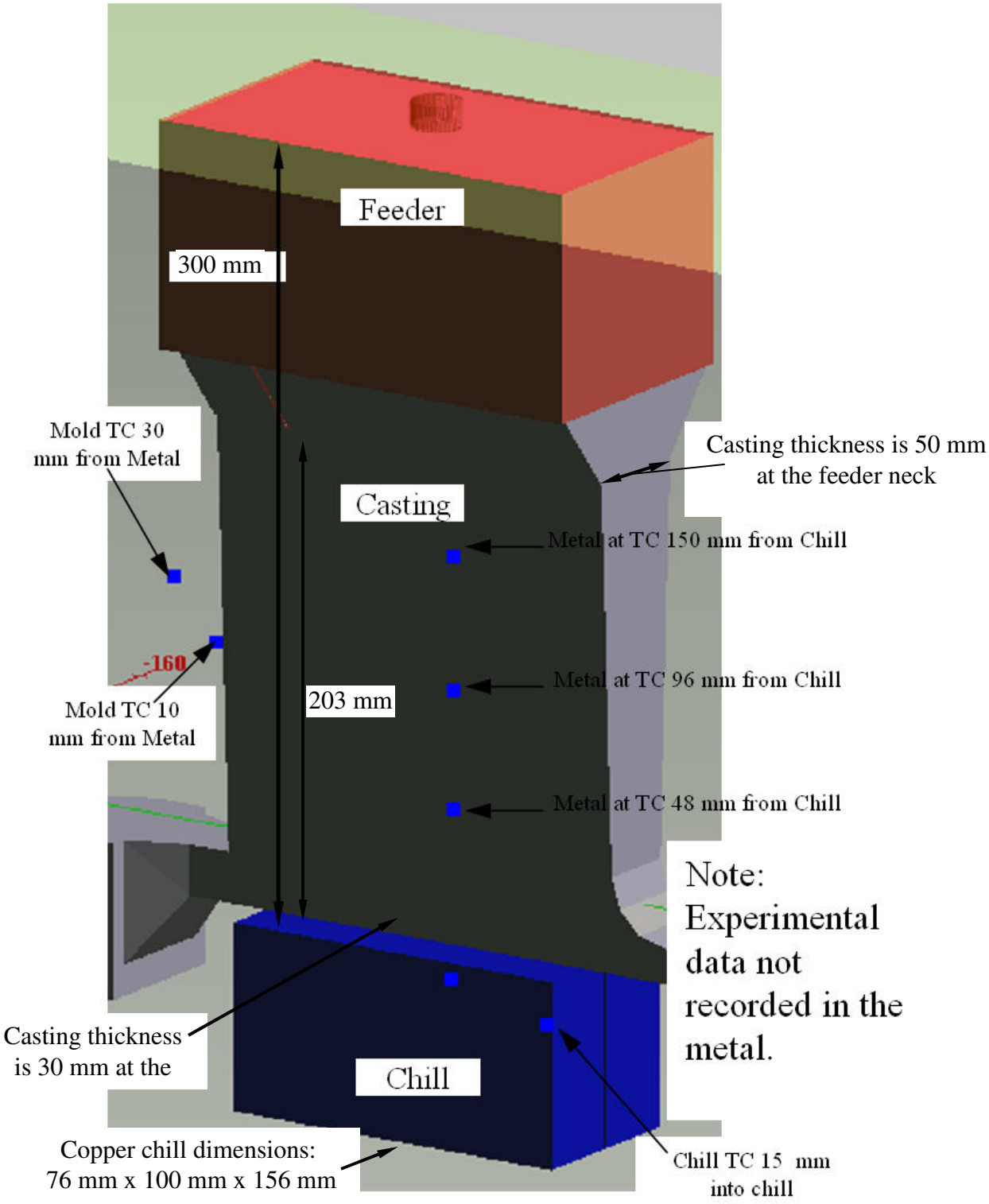

Figure 2 Casting simulation model of UAB wedge casting experiment with chill. Virtual (simulated) thermocouple (TC) positions are indicated. However, no metal thermocouples were used in the actual experiments.

The three other casting rigging configurations used to produce specimens for this study were produced at SFSA member foundries during high strength steel casting trials. The average solidification cooling rates for these specimen sections were consistently lower than the wedge configuration, and were typically in the 0.1 to 0.2 °C/s range. One of these configurations is shown in Figure 3, where the casting is a tapered circular disc with a single feeder. The plate has a diameter of 68 inches and 20% taper from its outer diameter to the riser diameter. The thickness of the plate is 2 inches at the outer diameter. The total weight of metal poured was about 900 pounds (408 kg). The specimen data from this configuration will be referred to as "disc" data. Two tensile specimens from this configuration were scanned using computed x-ray tomography and tested as described in the results section below.

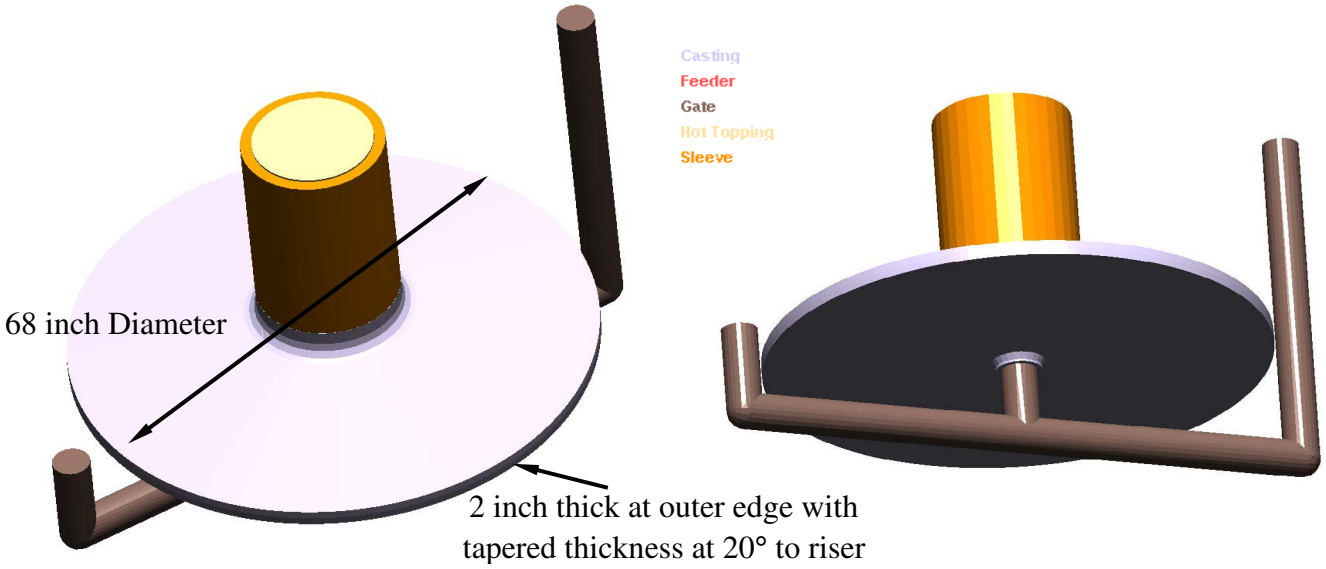

Figure 3 Casting model of the 68 inch diameter tapered circular disc plate. The casting was filled using centered bottom tile gating, and was cast with riser sleeve and hot topping.

The second configuration cast by an SFSA member to produce CT and tensile data presented in this study was a 4 foot square plate as shown in Figure 4. This square 4 foot x 4 foot plate casting was 2-3/4 inch (70 mm) thick a drag mold made from zircon with embedded compressed air lines to assist in cooling. In order to further promote directional solidification. The top of the casting was insulated as shown in Figure 4. The total weight of metal poured for this casting was about 2533 pounds (1149 kg). One tensile specimen from this plate was scanned using CT and tested in the data presented here. It will be referred to here as "4 foot plate" data. The third configuration cast by an SFSA member to produce tensile data for this paper is shown in Figure 5 and will be referred to here as "weld plate" data. It is a four-on casting rigging with each casting 2" thick x 4.5" wide x 15" long (50 mm x 381 mm x 114 mm). The total weight of metal poured to produce four castings was about 445 pounds (202 kg). The rigging shown in

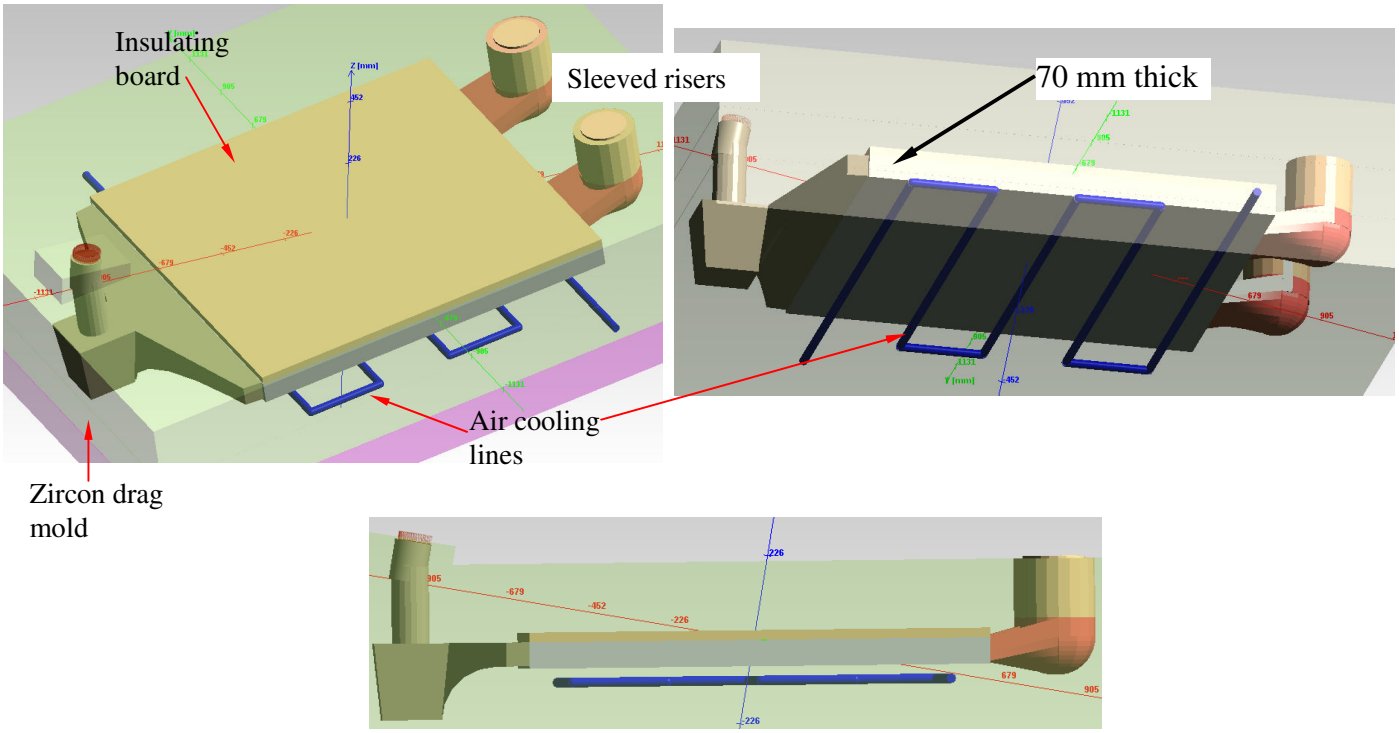

Figure 4 Three views of the casting simulation model for a 4 foot square plate, 70 mm (2-3/4 inch) thick. The drag is zircon with compressed air lines cooling the drag side as shown above.

Figure 5 was also cast to study the use of steel shot molds and mixes of shot and specialty sands to create composite mold materials to control and increase the solidification cooling rates of steel castings. The casting properties of these mold materials were

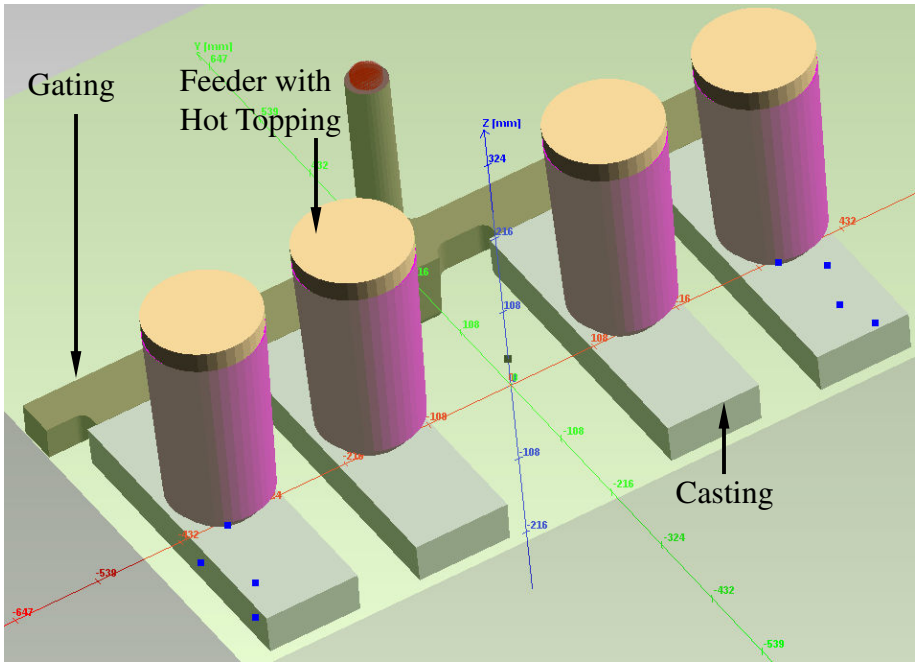

Figure 5 Simulation model of four weld plates used to produce tensile test specimens and for determination of temperature dependent properties for simulating steel shot mold materials.

determined such that good agreement was obtained between measured and predicted temperature data from the weld plate castings. Results of the steel shot mold investigation are summarized in the section of this paper titled "Results Section 2: Mold Materials for Increased Cooling Rates".

Results Section 1: Microporosity and Cooling Rate Effects on Mechanical Performance

Simulation Results and Analysis of Wedge Casting Data

The UAB wedge castings provide the largest data set presented here for investigating solidification conditions, porosity, cooling rate and mechanical properties. Simulations were performed and temperature dependent property data and heat transfer coefficients for modeling the wedge castings experiments were determined. Correspondence between measured and predicted temperatures in the casting simulations provides confidence that the thermal conditions in the simulations agree with actual casting conditions such as cooling rates and thermal effects on porosity predictions. This correspondence was as established by demonstrating agreement between the measured and predicted thermocouple data in the mold and chill seen in Figures 6 (a) and (b).

Porosity measurements were performed by UAB using optical microscopy and analysis [10] and at the Missouri University of Science and Technology (MS&T) using ASPEX SEM imaging with PICA 1020 software using automated feature analysis [11] as described in [1]. Casting simulations for the wedge castings were performed by the authors, producing porosity predictions using *MAGMAsoft's* "Microporosity" results. The development of the "Microporosity" result is described in [12] and uses a dimensionless Niyama Criterion to produce a quantitative porosity prediction. The porosity predictions for the wedge castings with and without the chill were quite low, less than 0.1%. Porosity at this level cannot be detected by standard NDE methods, such as radiography techniques performed on the casting, and would also be difficult to detect but ultrasonic testing of the casting. However, the porosity can be detected using micro x-ray CT as will be presented shortly. The porosity predictions were found to agree with the measured average porosity levels for the wedge chilled castings for three micrographs specimens performed at UAB as seen in Figures 7 to 9. In these figures the area averaged porosity measured by UAB and the predicted "Microporosity" results are given (the red text). The measured and predicted porosity is lowest at the chill in Figure 7, the porosity appears to be slightly over predicted in the Figure 8 comparison, and the porosity range predicted farthest from the chill in Figure 9 encompasses the measured value.

In Figure 10 the comparison of porosity predictions for the mid-thickness plane of the wedge casting with and without chill are shown, and there is a remarkable reduction in predicted microporosity at the base owing to the chill. The chill appears to reduce porosity to the mid-height of the casting. UAB and MS&T porosity measurements [10, 11] were performed on polished sections of the wedge castings at various positions from the base of the casting for cases with and without chill. These porosity

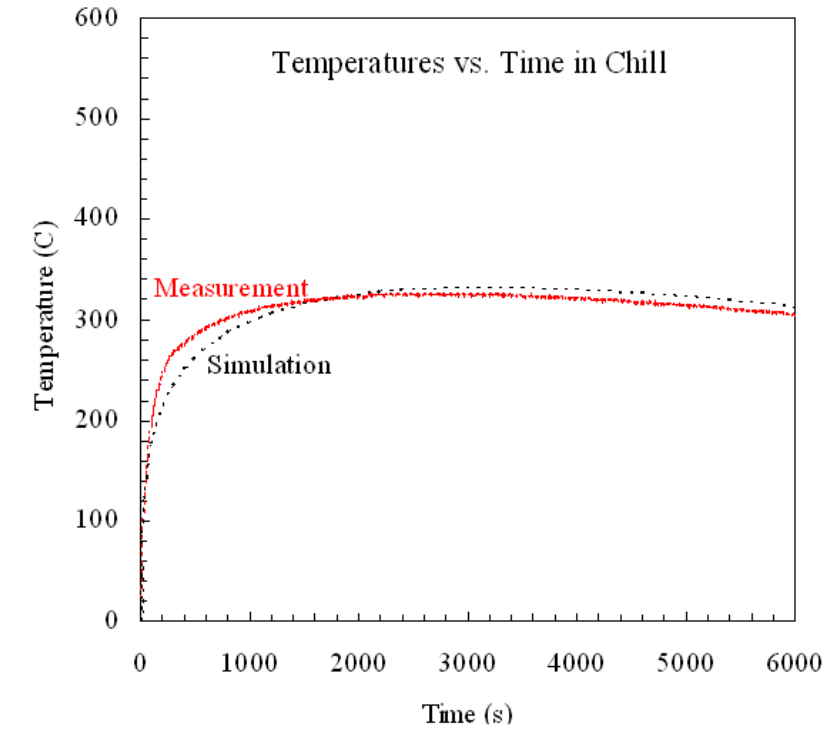

(a)

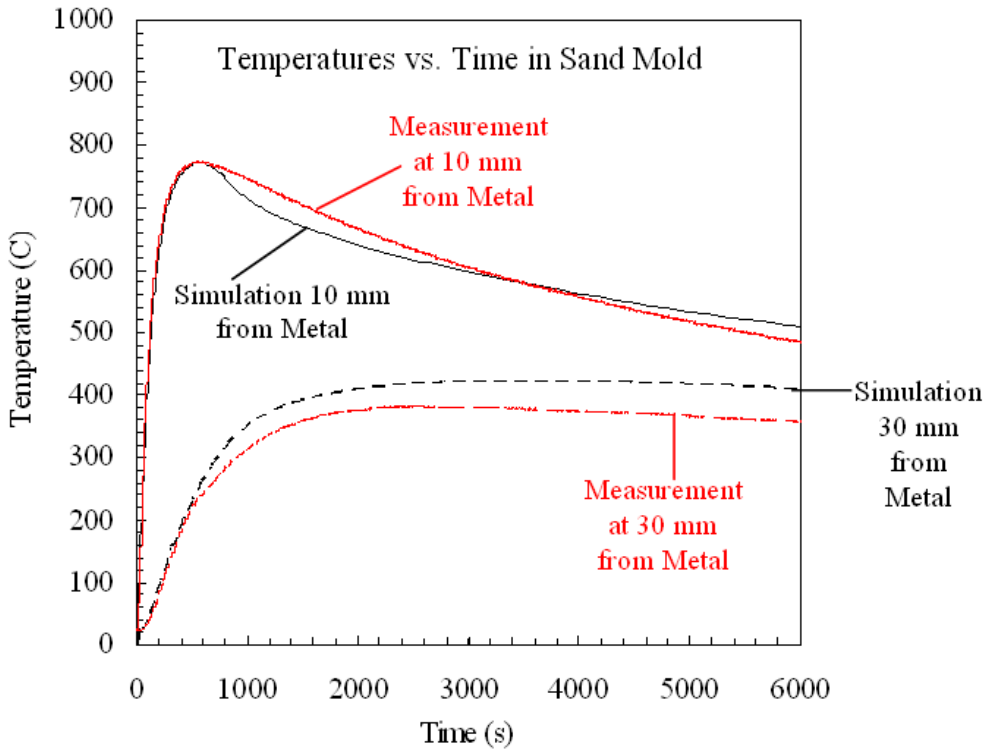

(b)

Figure 6 Measured (red) and simulated (black) temperature versus time curves for thermocouples in the (a) chill and (b) sand mold.

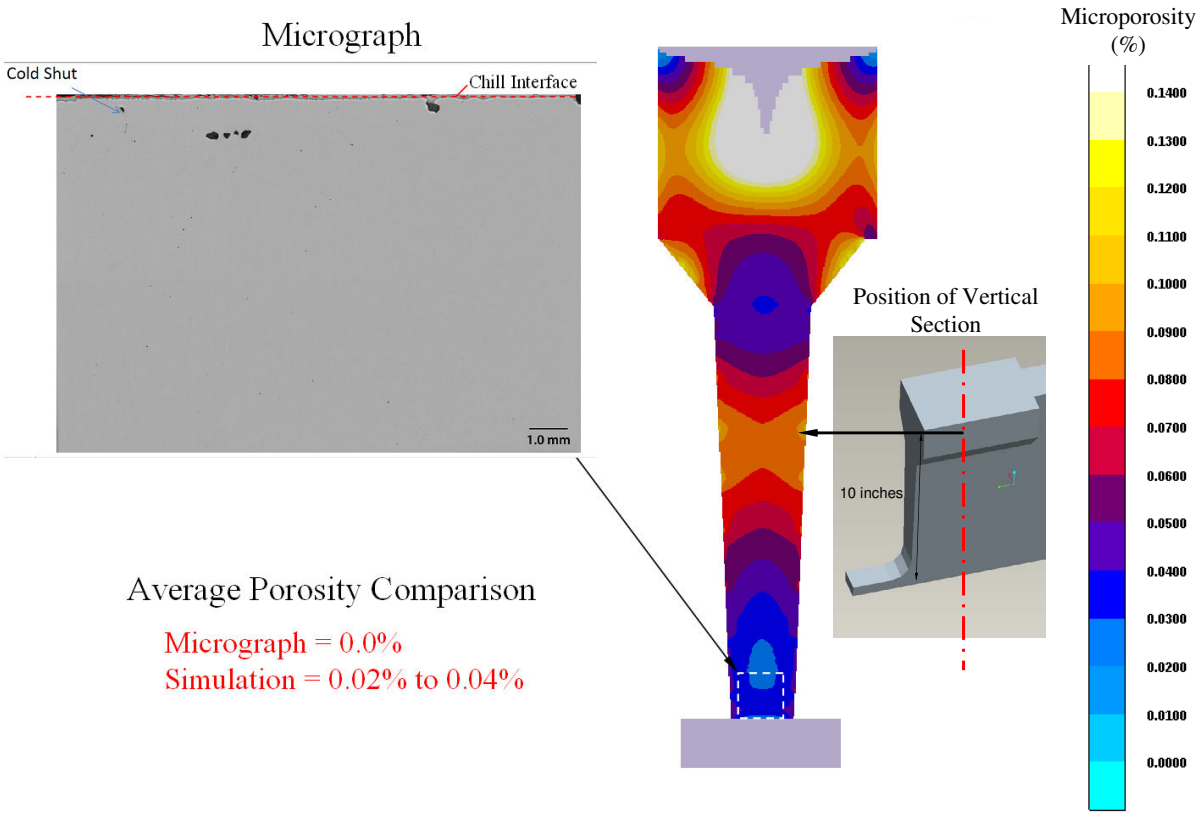

Figure 7 Predicted porosity for wedge casting with chill at its base. Micrograph (above left) of region indicated by the white box. Measured porosity is 0% and prediction is from 0.02 to 0.04%.

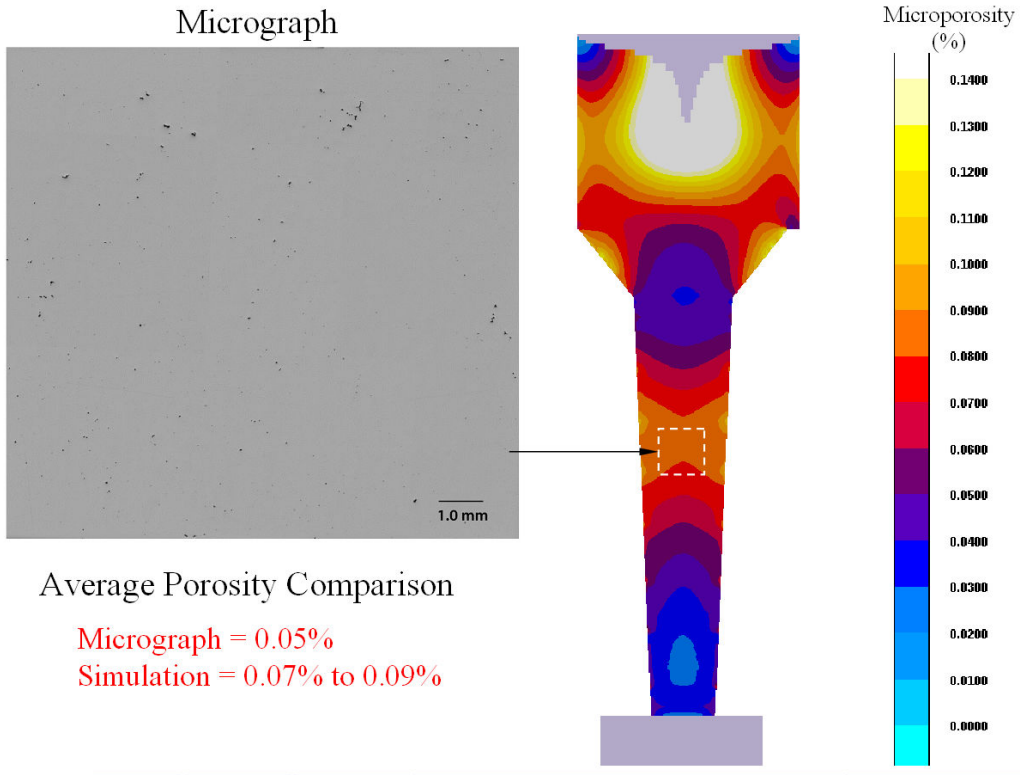

Figure 8 Predicted porosity for wedge casting with chill. Micrograph (above left) is taken at region in white box. Measured porosity is 0.05% and prediction is from 0.07 to 0.09%.

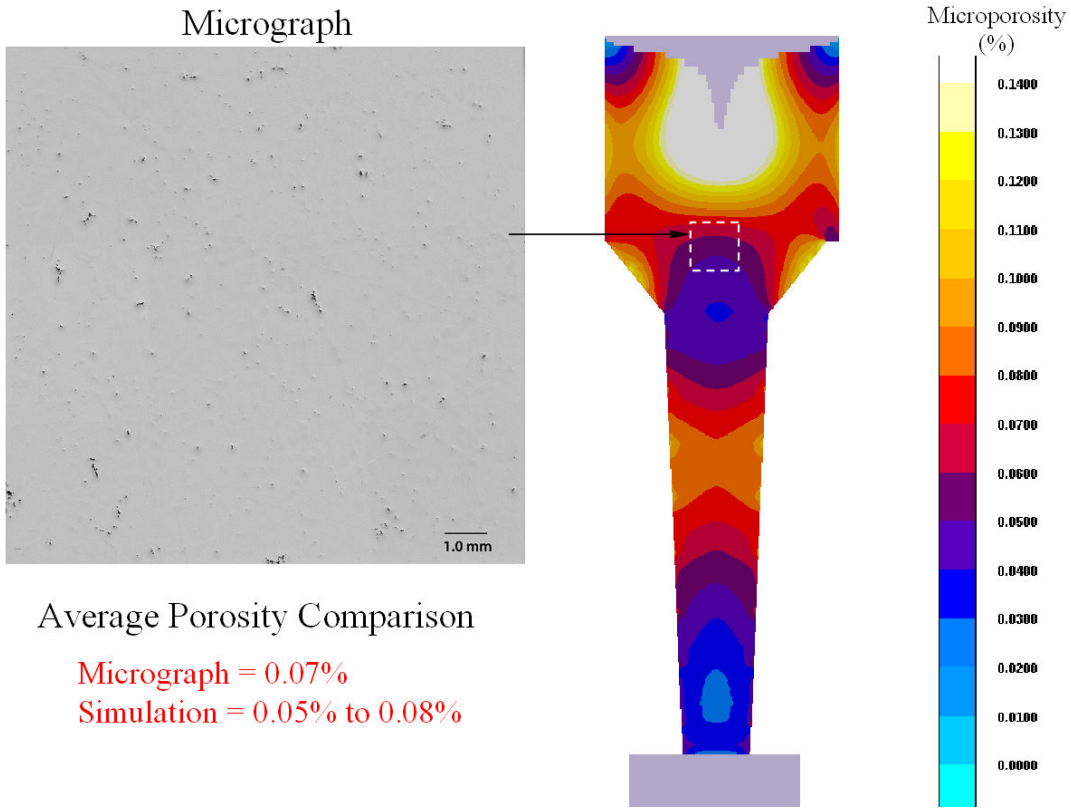

Figure 9 Predicted porosity for wedge casting with chill. Micrograph (above left) taken in region in the white box. Measured porosity in region is 0.07% and prediction ranges from 0.05 to 0.08%.

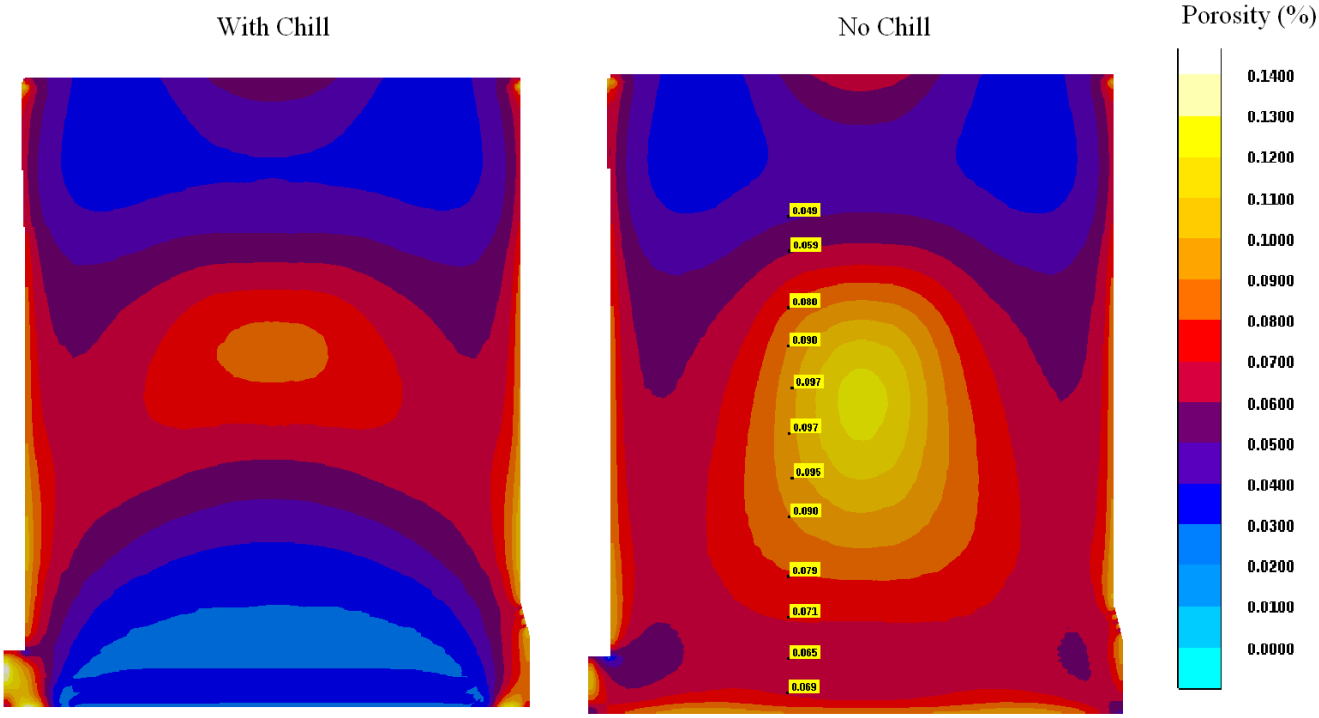

Figure 10 Predicted porosity on mid-thickness plane for wedge casting with chill at its base (above left side) and with chill (above right side).

measurements and the predicted porosity are compared directly versus distance from the casting base in Figures 11 and 12 for wedge castings produced without a chill and with a chill, respectively. The measurements and predictions both show a trend for the porosity measurements to be lowest near the base of the casting and at the chill (seen in Figure 12). Predicted and measured porosity increase as the data move farther away from the base/chill up to about 5 to 6 inches from it, but then both decrease with additional distance from the base/chill. Comparing the predictions in with and without chill by themselves in Figure 13, note that the effect of the chill is predicted to lower the porosity in the casting up to a distance of about 4 inches from the casting base/chill. The simulation is predicting the same trend versus distance from the casting base as the observed porosity. These results, and the direct comparison of the measured and predicted porosity in Figure 14, demonstrate that the "Microporosity" prediction has the same magnitudes and trends as the measured microporosity. Note that in the plots of predictions that follow below, the error bars indicate the range of predictions within a specimen.

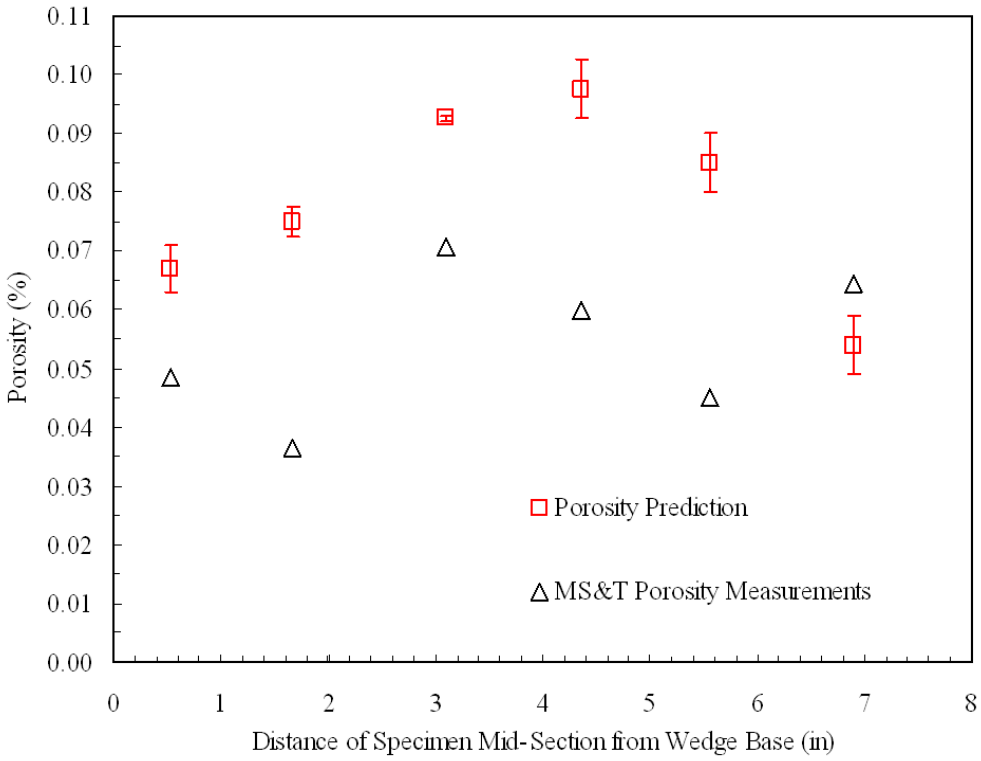

Figure 11 Predicted and measured porosity versus distance from the casting base for wedge casting **without** chill at its base.

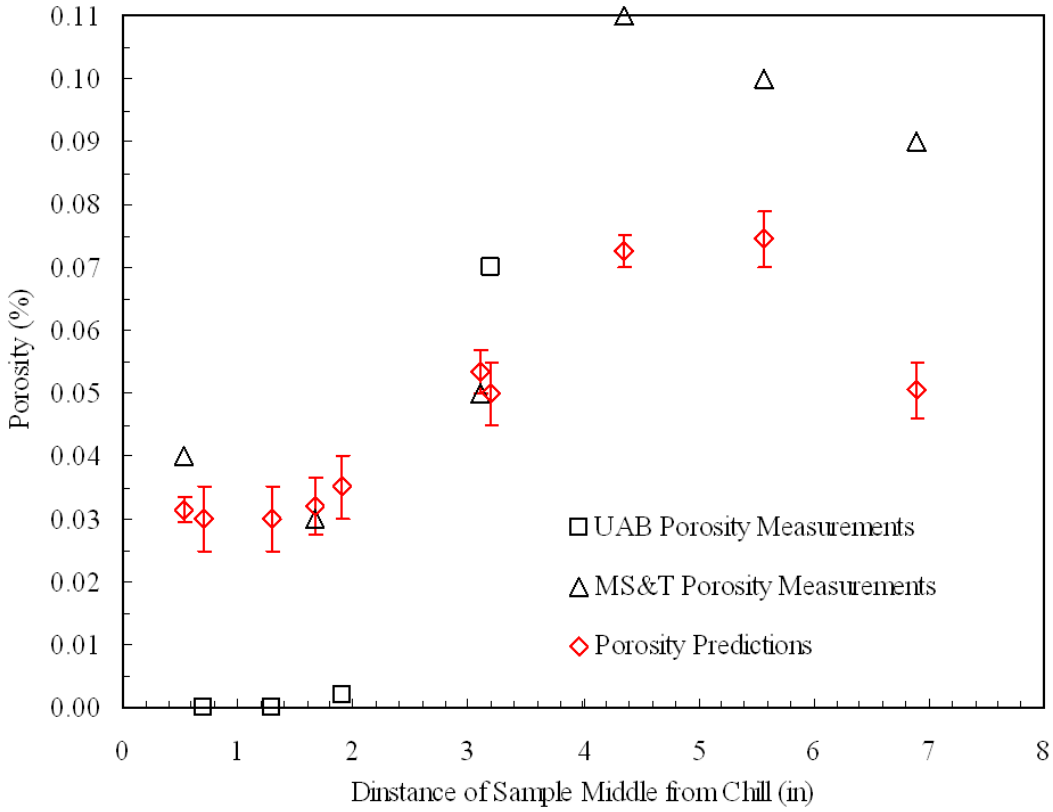

Figure 12 Predicted and measured porosity versus distance from the casting base for wedge casting **with** chill at its base.

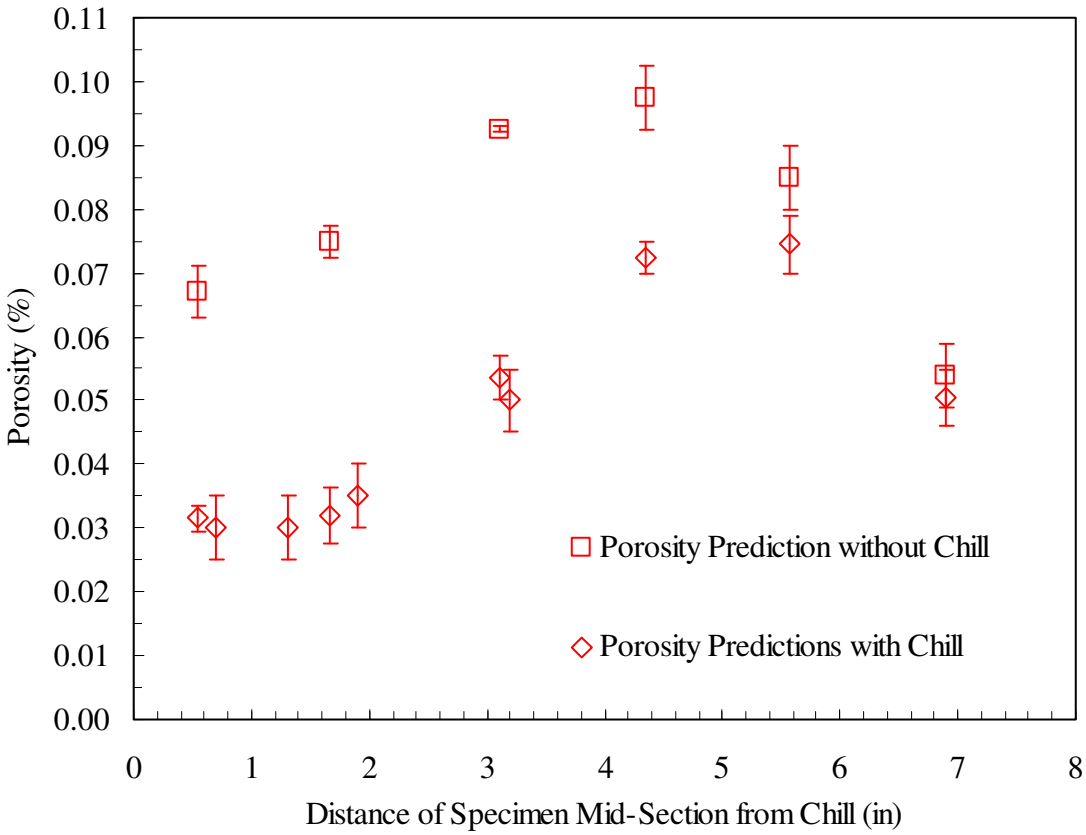

Figure 13 Predicted porosity versus distance from the casting base for wedge casting **with and without** chill positioned at the base.

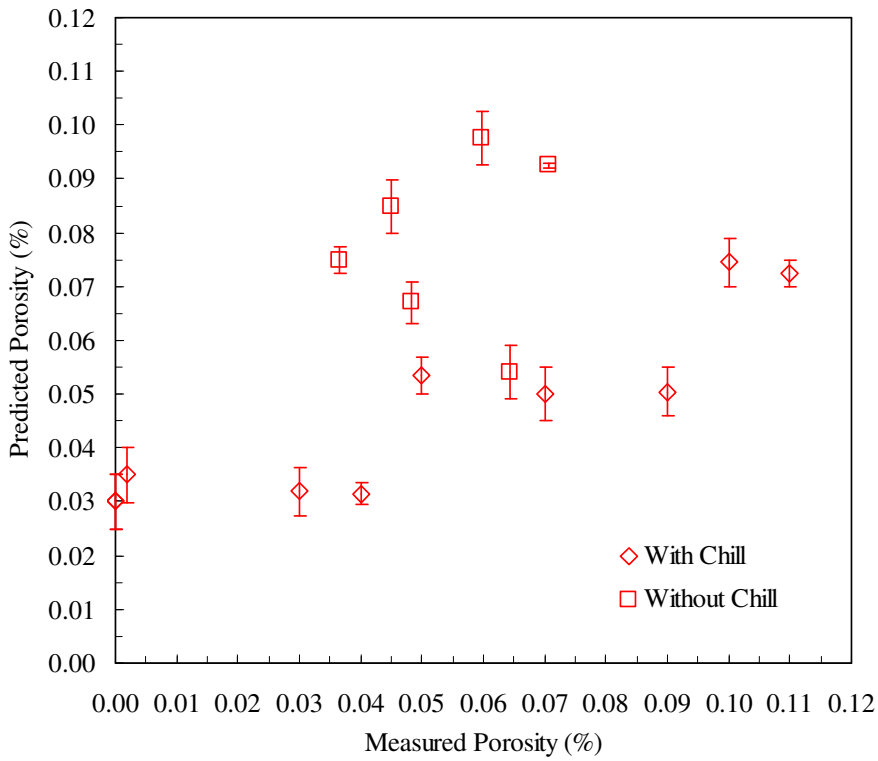

Figure 14 Predicted versus measured porosity for wedge castings **with and without** chill.

Tensile data reported here was measured by Westmorland Mechanical Testing & Research, Inc. in Youngstown, Ohio using ASTM E8-15a. The authors compiled this data and the measurements by UAB and MS&T and performed statistical analysis to establish correlations between mechanical properties, optical microscopy, Aspex scanning electron microscopy and simulation data. Statistical Analysis System (SAS) Enterprise Guide 5.1 software was used for the statistical analysis. Tensile strength and yield strength were not found to correlate as highly as the ductility measures with the microscopy and simulation data. Also, it was determined that ductility was a key property limiting the performance of the steel, and a means of achieving good consistent ductility needed to be developed. The most highly correlated variables were identified, and a correlation matrix was determined for elongation (*EL%*) and reduction of area (*RA%*) and eight other variables. Five variables are determined from microscopy on the fracture surface or on polished specimen surfaces near the fracture: *fracture surface porosity %, maximum pore cluster size on the fracture surface, polished porosity %, maximum diameter of pore on polished surface,* and *secondary arm spacing (SDAS)*. Three other variables are solidification simulation results: *temperature gradient, cooling rate* (from the Niyama Criterion calculation) and *solidification rate* (over the entire solidification range). The correlation matrix is given in Table II. Each variable combination in the correlation matrix provides three entries from the analysis as shown in the red outlined box in the uppermost right of the table for the "Fracture Porosity (%)" and "Solidification Rate (°C/s)" variable combination: 1) correlation coefficient, 2) probability that correlation is

Table II Correlation matrix between mechanical properties and microscopy, Aspex and simulation data. Circled numbers are probability of obtaining correlation by chance where **color signifies significance level** from highest (lowest probability it is by chance) to least (highest probability that correlation is by chance).

Highest Correlation | High Correlation 99.9% Level | Correlation Significant at 99% Level | Correlation Significant at 95% Level | Correlation Significant at 90% Level | Correlation Significant at 80% Level | Below 80% Level *Nothing!*

Most significant → Least significant

Variables →	Fracture Porosity (%)	Polished Porosity (%)	Polished Max Diam. (µm)	Fracture Max Cluster (mm)	Elongation %	Reduction in Area %	SDAS Avg (µm)	Thermal Gradient (°C/mm)	Cooling Rate (°C/s)	Solidification Rate (°C/s)
Fracture Porosity (%)	1	0.11583	0.36325	0.86672	-0.73261	-0.68899	0.41254	-0.64507	-0.61575	-0.58988
		0.681	0.0574	<.0001	<.0001	<.0001	0.0291	0.0002	0.0005	0.001
	28	15	28	28	28	28	28	28	28	28
Polished Porosity %	0.11583	1	0.81563	0.09132	-0.36357	-0.39305	0.24376	-0.10891	-0.14278	-0.27602
	0.681		0.0002	0.7462	0.1828	0.1472	0.3813	0.6992	0.6117	0.3194
	15	15	15	15	15	15	15	15	15	15
Polished Max Diam. (µm)	0.36325	0.81563	1	0.40677	-0.30976	-0.38684	0.27595	-0.40265	-0.40677	-0.41071
	0.0574	0.0002		0.0317	0.1087	0.042	0.1552	0.0336	0.0317	0.0299
	28	15	28	28	28	28	28	28	28	28
Fracture Max Cluster (mm)	0.86672	0.09132	0.40677	1	-0.69532	-0.74996	0.40897	-0.59275	-0.55013	-0.50593
	<.0001	0.7462	0.0317		<.0001	<.0001	0.0307	0.0009	0.0024	0.006
	28	15	28	28	28	28	28	28	28	28
Elongation %	-0.73261	-0.36357	-0.30976	-0.69532	1	0.91705	-0.63992	0.57324	0.53316	0.52312
	<.0001	0.1828	0.1087	<.0001		<.0001	0.0002	0.0014	0.0035	0.0043
	28	15	28	28	28	28	28	28	28	28
Reduction in Area %	-0.68899	-0.39305	-0.38684	-0.74996	0.91705	1	-0.60302	0.5798	0.50946	0.49395
	<.0001	0.1472	0.042	<.0001	<.0001		0.0007	0.0012	0.0056	0.0076
	28	15	28	28	28	28	28	28	28	28
SDAS Avg (µm)	0.41254	0.24376	0.27595	0.40897	-0.63992	-0.60302	1	-0.30367	-0.29811	-0.34756
	0.0291	0.3813	0.1552	0.0307	0.0002	0.0007		0.1162	0.1234	0.0699
	28	15	28	28	28	28	28	28	28	28
Thermal Gradient (°C/mm)	-0.64507	-0.10891	-0.40265	-0.59275	0.57324	0.5798	-0.30367	1	0.98291	0.94523
	0.0002	0.6992	0.0336	0.0009	0.0014	0.0012	0.1162		<.0001	<.0001
	28	15	28	28	28	28	28	28	28	28
Cooling Rate (°C/s)	-0.61575	-0.14278	-0.40677	-0.55013	0.53316	0.50946	-0.29811	0.98291	1	0.97965
	0.0005	0.6117	0.0317	0.0024	0.0035	0.0056	0.1234	<.0001		<.0001
	28	15	28	28	28	28	28	28	28	28
Solidification Rate (°C/s)	-0.58988	-0.27602	-0.41071	-0.50593	0.52312	0.49395	-0.34756	0.94523	0.97965	1
	0.001	0.3194	0.0299	0.006	0.0043	0.0076	0.0699	<.0001	<.0001	
	28	15	28	28	28	28	28	28	28	28

Each Variable Combination has 3 entries:
1-Correlation Coefficient
2- Probability that Correlation is due to Random Chance
3-Sample size

Each Variable Correlates Perfectly with itself!

due to random chance, and 3) sample size. For the this variable combination the correlation coefficient is -0.59, the probability that correlation is due to random chance is 0.1%, and data sample size is 28. Negative correlation indicates that as one variable increases as the other variable decreases

Focusing on the variables that correlate with the ductility performance variables *EL%* and *RA%*, the strongest correlations are with the fracture surface porosity % (*FSP*) and maximum pore cluster size measured on the fracture surface. Since they are physically related, it is not surprising that *EL%* and *RA%* are strongly correlated with each other. Since the two fracture surface variables are a direct reflection of the "weakest links" along the specimen gage section and this determines ductility and failure of the material, it is not surprising that they show the strongest correlation. Unfortunately, casting simulation cannot predict fracture surface porosity *FSP*; it can predict volumetric averaged porosity. The *FSP* cannot be predicted since it is an outcome of stochastic factors such as how the porosity is locally distributed relative to the loading of the specimen, and the size and orientation of pores relative to the load. Since the *FSP* cannot be predicted, it cannot be used along with casting simulation to predict mechanical performance. The fracture surface variables do provide insight into the material behavior, and Figures 15 and 16 show the *EL%* and *RA%* versus the *FSP*, respectively. From Figure 15, one can see that at a given *FSP* level there is a range of ductility performance, and lower *FSP* results in higher ductility. In these plots, and similar plots that follow, the wedge casting data produced

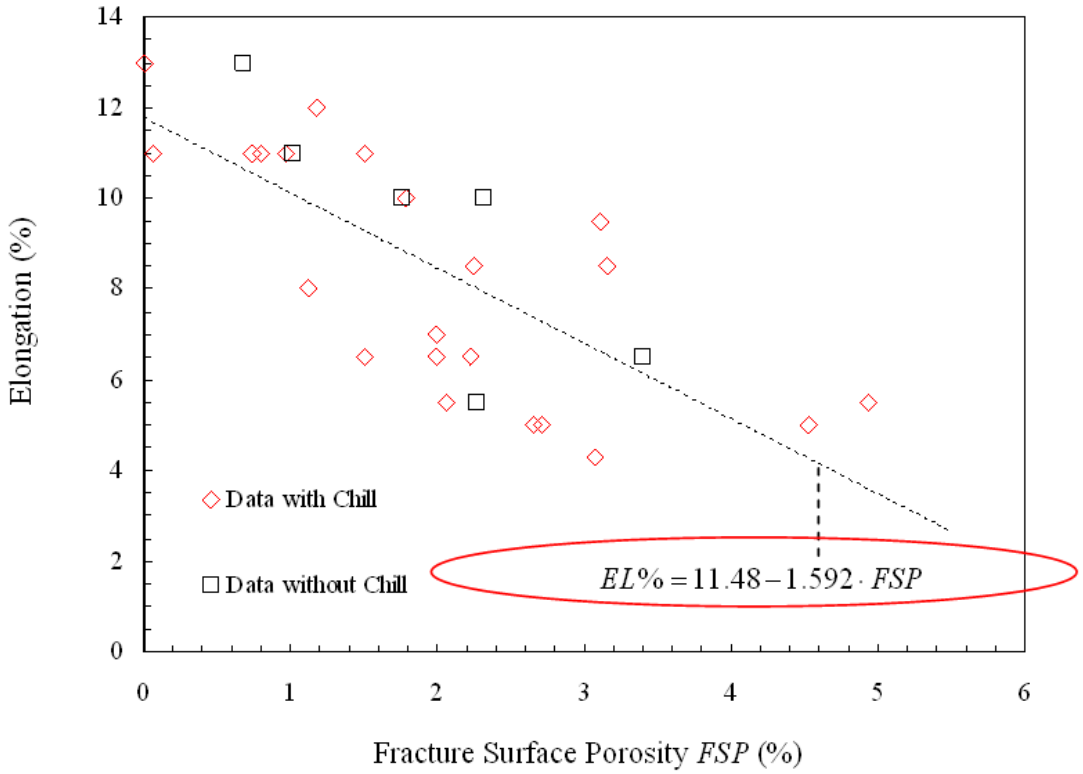

Figure 15 Elongation to failure for UAB wedge castings with and without the base chills was found to be highly correlated with measured porosity on the fracture surface. A linear best-fit between them is circled in red.

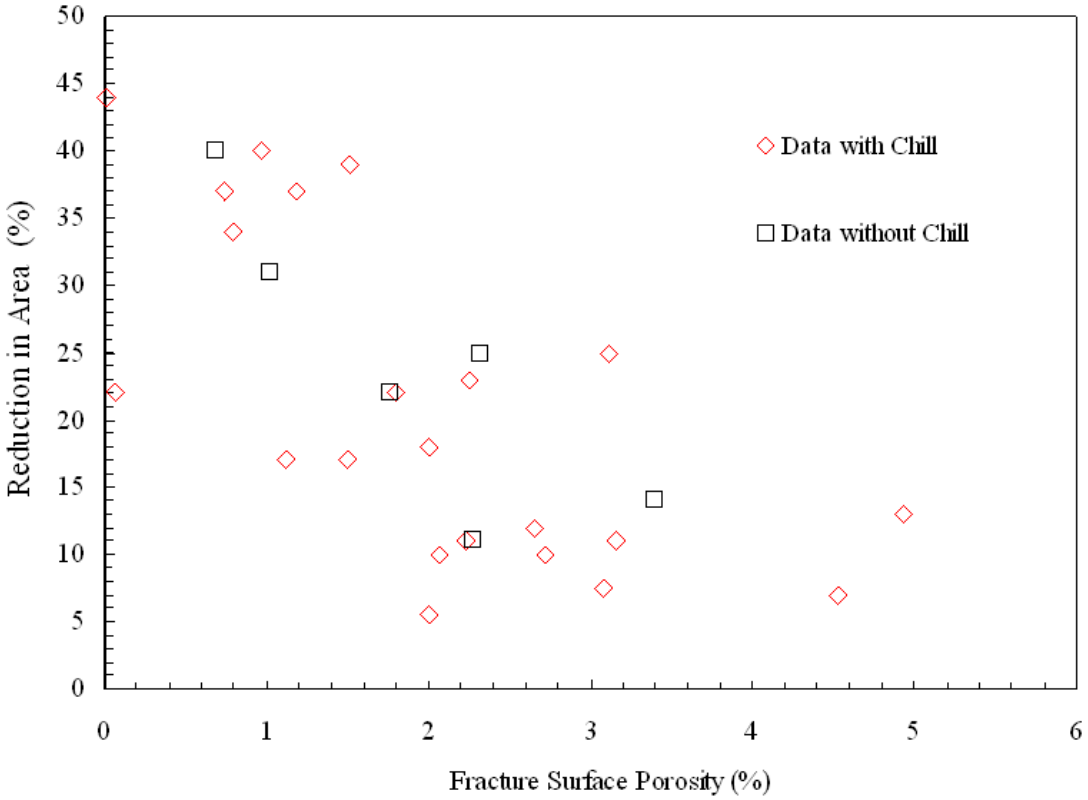

Figure 16 Reduction in area for UAB wedge castings with and without the base chills was found to be highly correlated with measured porosity on the fracture surface.

with and without the chill have been indicated separately to see whether there are any trends or outlying behavior that might be explained by use of the chill.

From stereology, the porosity measured using microscopy on cut and polished specimen surfaces are a measure of the volumetric porosity predicted by casting simulation. This assumes that the surface slice is representative of the typical porosity and that the porosity is uniformly distributed in the specimen. Note that the porosity measured on polished specimen surfaces is uncorrelated with the *FSP* as seen in the upper left of Table II. Again, this is because the *FSP* is not a measure of randomly distributed porosity but the largest and weakest link of material along the specimen gage length. Note that the polished surface porosity was found to not correlate with any of the individual simulation determined variables (thermal gradient, cooling rate and solidification rate). These variables in isolation by themselves do not predict porosity. The polished surface porosity measurements are correlated at the 80% confidence level with the ductility variables *EL%* and *RA%*. This data is plotted in Figures 17 and 18. The data show that if an *EL%* of 10% or greater is desired, the porosity should be limited to 0.04% or less for this high strength steel. This was also a finding of Van Aken et al. [1].

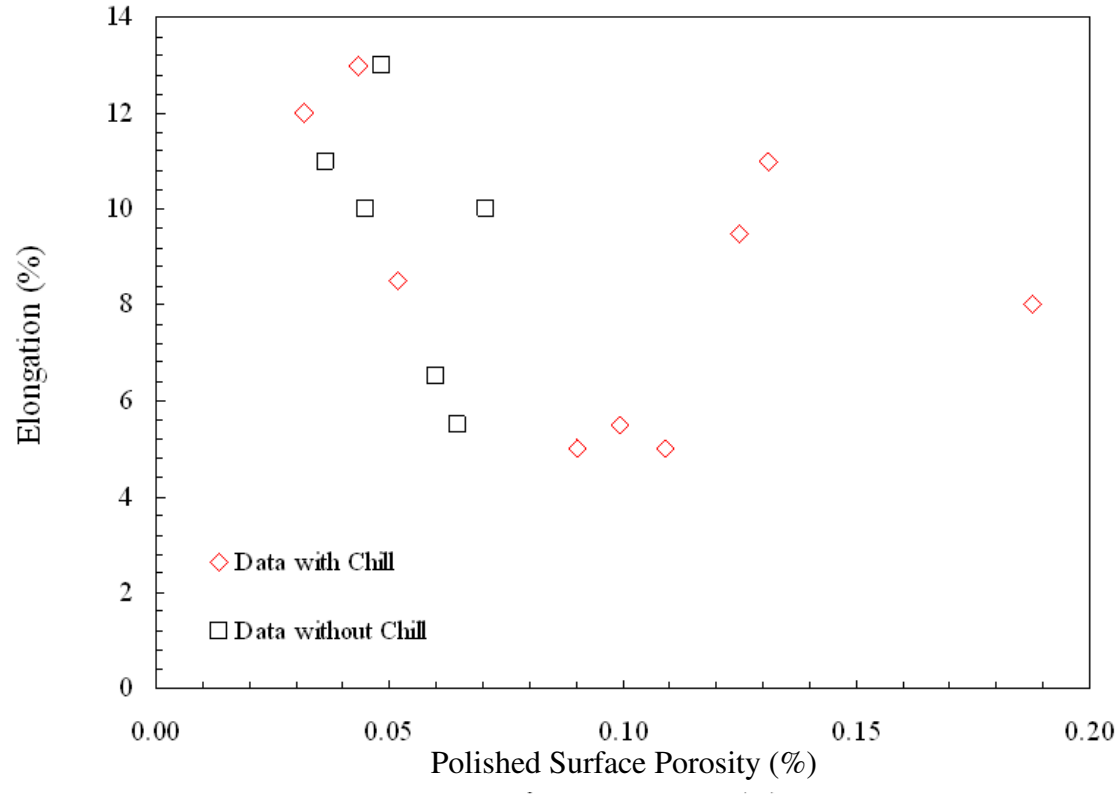

Figure 17 Measured polished surface porosity from specimens and elongation for UAB wedge castings. This data is correlated at the 80% confidence level.

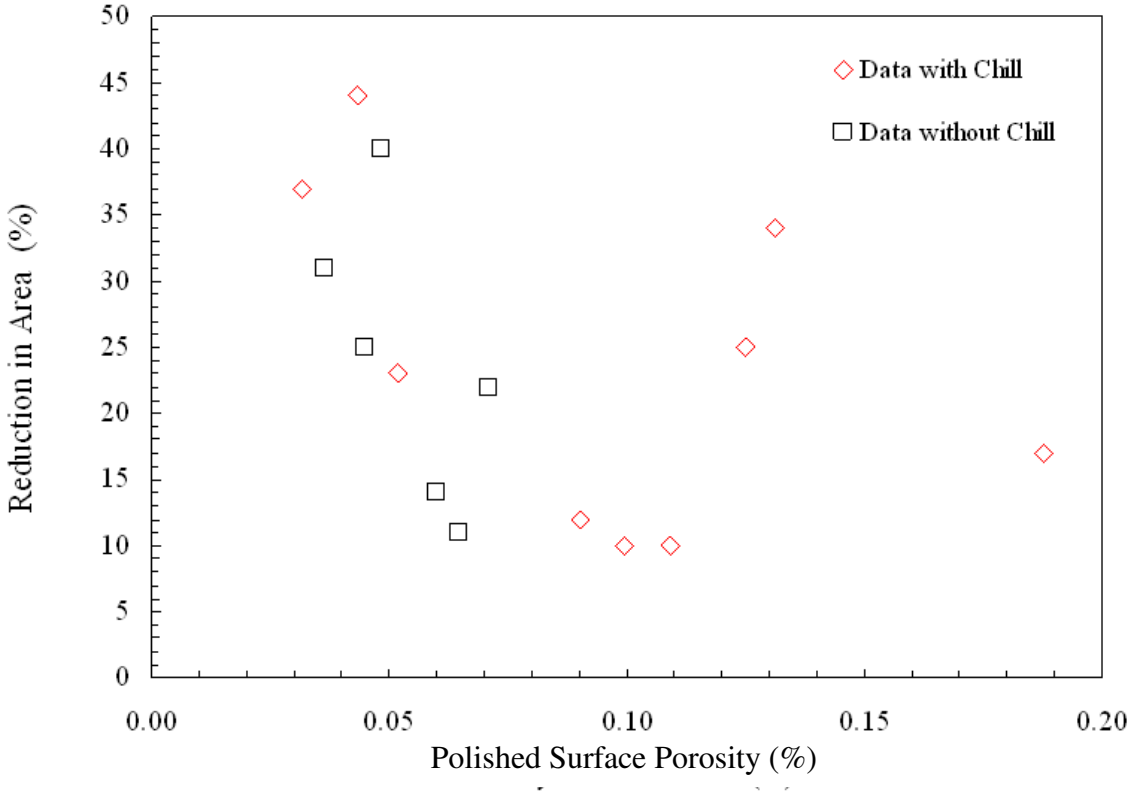

Figure 18 Measured polished surface porosity from specimens and reduction in area for UAB wedge castings. This data is correlated at the 80% confidence level.

The simulations variables (thermal gradient, cooling rate and solidification rate) correlated with the ductility (*EL%* and *RA%*) at the 99% level, and with measured secondary dendrite arm spacing (SDAS) at the 99.9% level. As will be discussed shortly, SDAS is directly related to the solidification cooling rate, but non-linearly. This is perhaps the reason that the SDAS and solidification cooling rate are correlated at the 90% level, and is not more strongly correlated. The elongation and reduction in area versus measured secondary dendrite arm spacing (SDAS) is plotted in Figures 19 and 20, respectively. These results, and the data in Figures 17 and 18, indicate that both SDAS (a fine microstructure) and porosity are important in the resulting ductility behavior of this high strength steel. The predicted porosity for the UAB wedge castings is not included in the correlation matrix, Table II. The predicted porosity did not show a highly significant correlation with measured ductility. Data for measured elongation versus predicted porosity is shown in Figure 21. The scatter in the data contributes to the low correlation. Data for wedge castings without chill appear to have about the same ductility range as data from castings with chill even though the predicted porosity is higher for some casting data points produced without chill. With additional data points for castings produced without chills, the outlying "without chill" data apparent in Figure 21 might be explained and clarified. It would be advantageous to explain how such good ductility properties were produced from material that should have had higher porosity and larger SDAS. Note from Figure 19, it appears that a SDAS less than 100 μm should result in good ductility and *EL%* 10% or greater. Note that Figure 21 shows that if the porosity predictions are less than 0.04% then casting simulation can be used with that threshold to develop production processes for optimizing the ductility of parts cast with this high strength steel. The casting process and rigging can be designed to give the best possible properties in high strength steel castings where they are most needed.

The cooling rate during solidification and the carbon content for steel are empirically related to the SDAS, for example as expressed by Won and Thomas [13]

$$\lambda_2 = \begin{cases} (169.1 - 720.9 \cdot C_C) \times \dot{T}^{-0.4935} & \text{for } 0 < C_C < 0.15 \\ 143.9 \cdot C_C{}^{(0.5501 - 1.996\ pctC_C)} \cdot \dot{T}^{-0.3616} & \text{for } 0.15 < C_C \end{cases} \quad (1)$$

where λ_2 is the SDAS in units (μm), $\dot{T}$ is the solidification cooling rate is in units (°C-s^{-1}), and C_C is the weight percentage of carbon in the steel. Using a power law dependency on solidification cooling rate like Equation (1), but fitted specifically for the high strength steel chemistry in Table I, the following relationship was found for λ_2

$$\lambda_2 = 106.5\left(\dot{T}\right)^{-0.1669} \quad (2)$$

where this curve and the data used to determine the best-fit are plotted in Figure 22 on a log-log scale. The measured and predicted SDAS data using Equation (2) are plotted in Figure 23 and the predictions appear to be within 20 μm of the measurements over the range of SDAS, from 70 to 180 μm. A user result was added to the result database in *MAGMAsoft* using Equation (2) for SDAS as plotted on the wedge casting mid-thickness plane in Figure 24. The user results shown in Figure 24 can be used to develop casting processes where SDAS can be target for 100 μm or less in regions of castings where superior ductility is required.

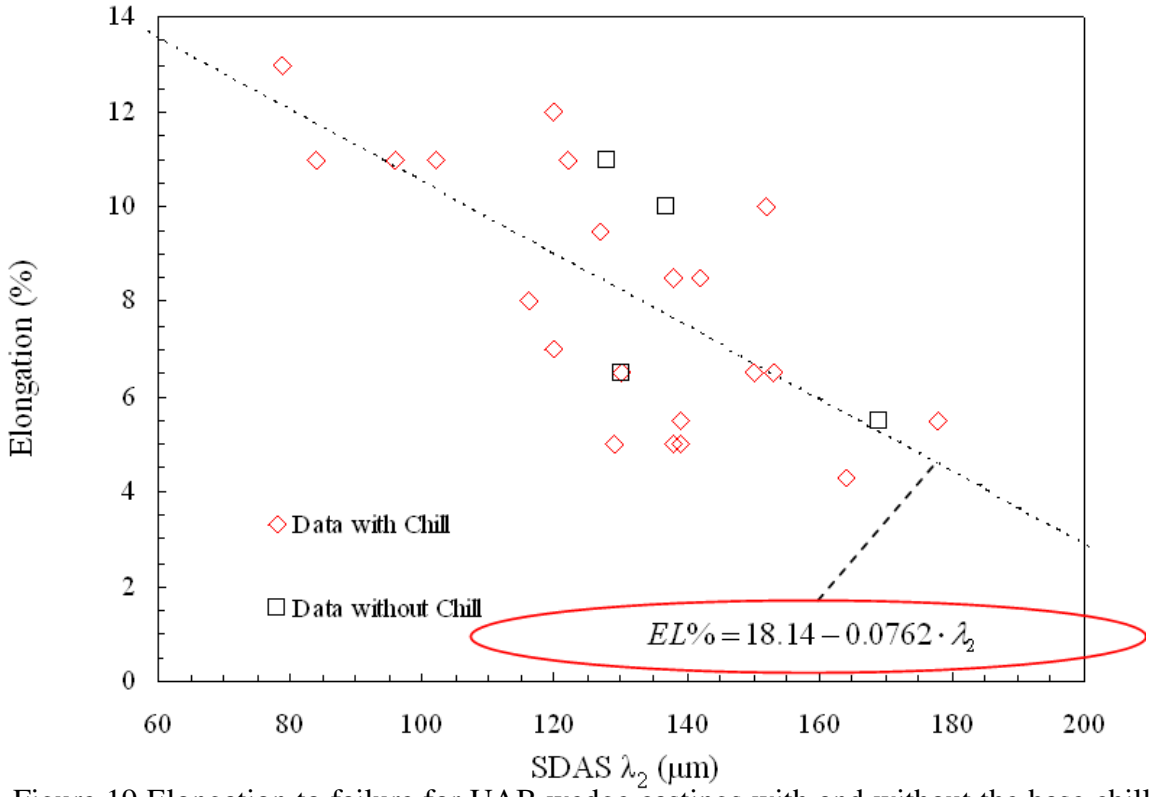

Figure 19 Elongation to failure for UAB wedge castings with and without the base chills was found to be highly correlated (99.9% level) with measured SDAS on specimen surface. The linear curve fit between them is circled in red.

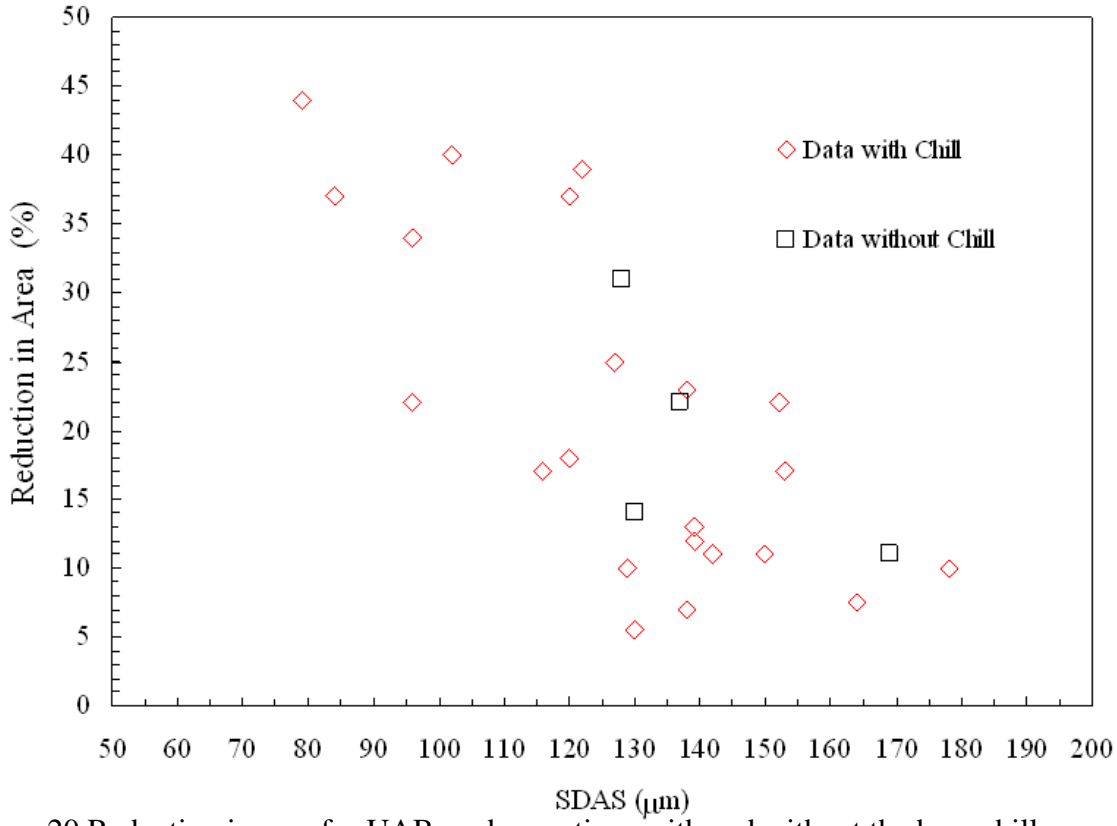

Figure 20 Reduction in area for UAB wedge castings with and without the base chills was found to be highly correlated with measured SDAS on specimen surface.

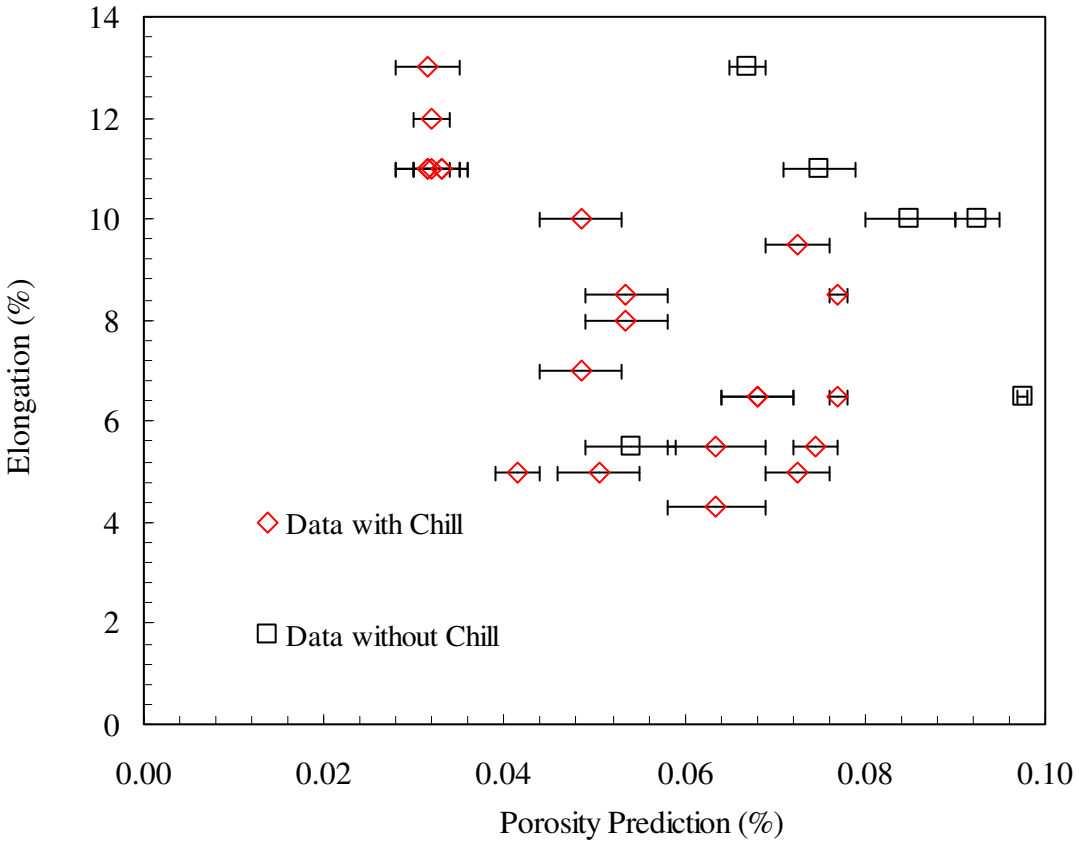

Figure 21 Elongation to failure and porosity prediction (median, minimum and maximum are plotted) were not significantly correlated for the wedge castings.

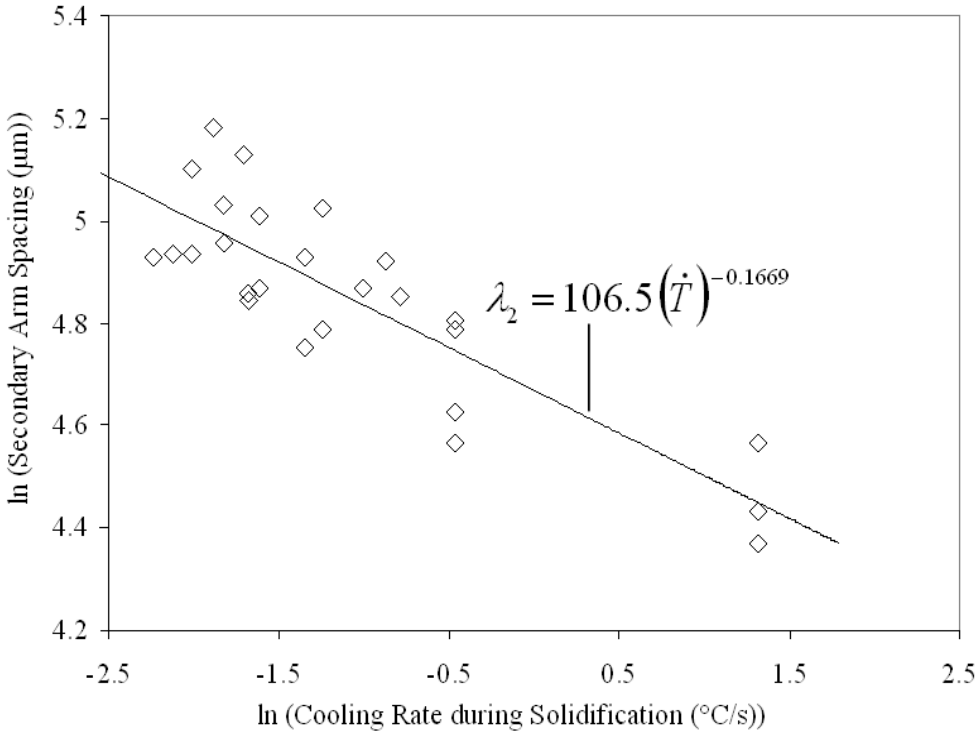

Figure 22 Measured SDAS versus predicted cooling rate for the UAB wedge castings. Correlating equation between them also shown.

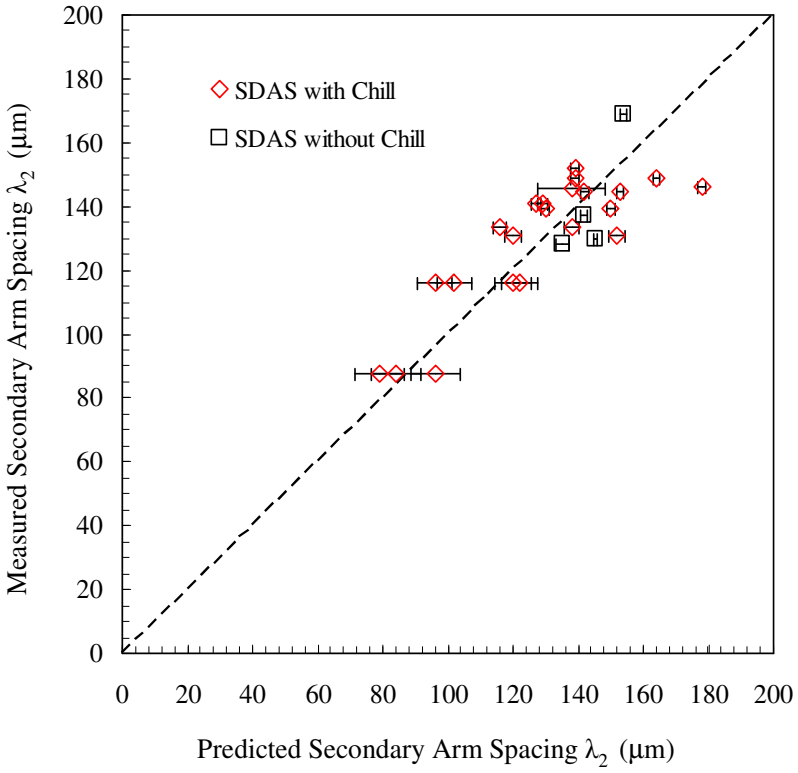

Figure 23 Measured versus predicted SDAS for the UAB wedge castings using local cooling rate in predictions and Equation (2).

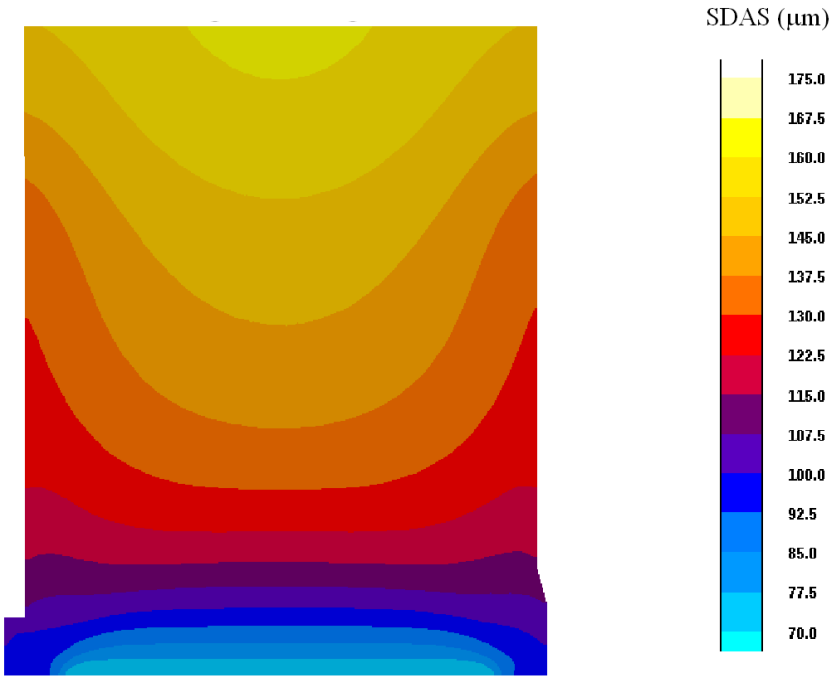

Figure 24 The *MAGMAsoft* user results for SDAS plotted on the wedge casting mid-thickness plane.

Results of X-Ray Computed Tomography

X-Ray computed tomography scanning (or CT scanning) is becoming a powerful and more commonly used tool in non-destructive testing and evaluation. It provides an internal three-dimensional volumetric set of data for visualization and analysis of the internal features, density and voids of cast components. In this case it was used to collect such data on four of the tensile test specimens prior to testing. As part of the SFSA research program that sponsored this work, Chesapeake Testing in Belcamp, MD was contracted to perform the CT scans, and they provided the data files along with software to visualize the scans. The scans were performed using a resolution of 0.0249 mm (0.001"), so the individual voxels in the volumetric scan are cubes of 25 μm on a side. The scans for each specimen have total dimensions of approximately 12 mm x 12 mm x 45 mm, and there is approximately 3 gigabytes of data in each scan. The scan data are organized as stacks of 32-bit gray scale image slices that can be used with the vendor-provided software to view the data as shown in Figure 25. In this figure is a screen image of CT scan data visualized using the software. The top image shows an axial slice along the specimen gage section length corresponding the position along the length indicated by the blue line in the lower figure showing the specimen length perspective. Note that several porosity indications are circled on the cross sectional slice. The user can make measurements of the size and other geometric features of individual indications on the slices. However, the software is limited and cannot be used to analyze the porosity data throughout the specimen volume.

In order to visualize the porosity volumetric distribution and make quantitative measurements on it, additional image data processing is required. For this the authors used the public domain software *ImageJ* [14] which has been developed by the U. S. National Institutes of Health. The gray scale images of the axial cross sections of the specimen are processed to produce binary (black/white) images which are assembled in a stack along the specimen length in order to visualize and measure the porosity. As shown in Figure 26(a), the initial gray scale image for a given slice is filtered so only data in the specimen cross section remains. All images in the stack of approximately 1800 images are filtered using a 12 pixel rolling ball to subtract the background, shadows and CT artifacts (such as the one circled with red in Figure 26(a)), and the a binary threshold of 229 on an 8-bit gray scale is applied. The threshold creates a binary image by converting gray scale levels at 229 and above to black and below it to white as shown in Figure 26(b). The black voxels can then be visualized and rendered in the 3D volumetric visualization tools in *ImageJ*. Also the area percentage of porosity of the images like Figure 26(b) can be calculated, and the volume average porosity is found by averaging this porosity for all slices.

The four specimens that were scanned using CT are labeled and described as: "UAB-3" a wedge casting specimen taken from the base of the casting at the chill contact, "A1" a tapered disc casting specimen taken from material about half way from the outer edge to the center, "F1" a tapered disc casting specimen taken near outer edge of the disc in the end-effected zone, and "C1" a 4 foot x 4 foot plate specimen taken from a region inside from the end-effected zone. Output from the *ImageJ* volumetric visualization tool for the porosity distributions in specimens "UAB-3", "A1", "F1", and "C1" are shown in Figures 27, 28, 29 and 30, respectively.

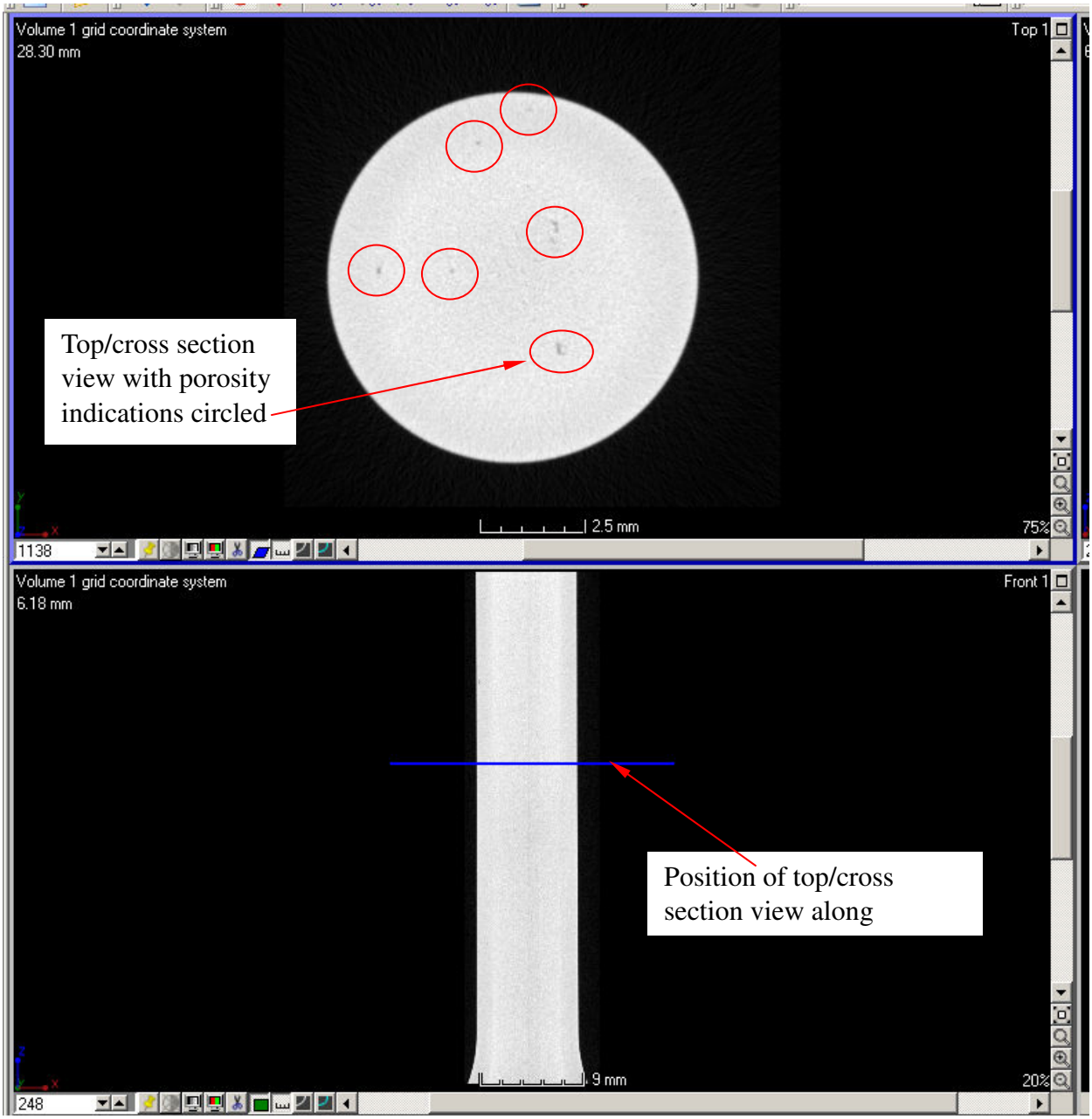

Figure 25 Screen image of CT scan data visualized using the software provided by the CT scan vendor. Top image shows an axial slice along the specimen gage section length with several porosity indications circled.

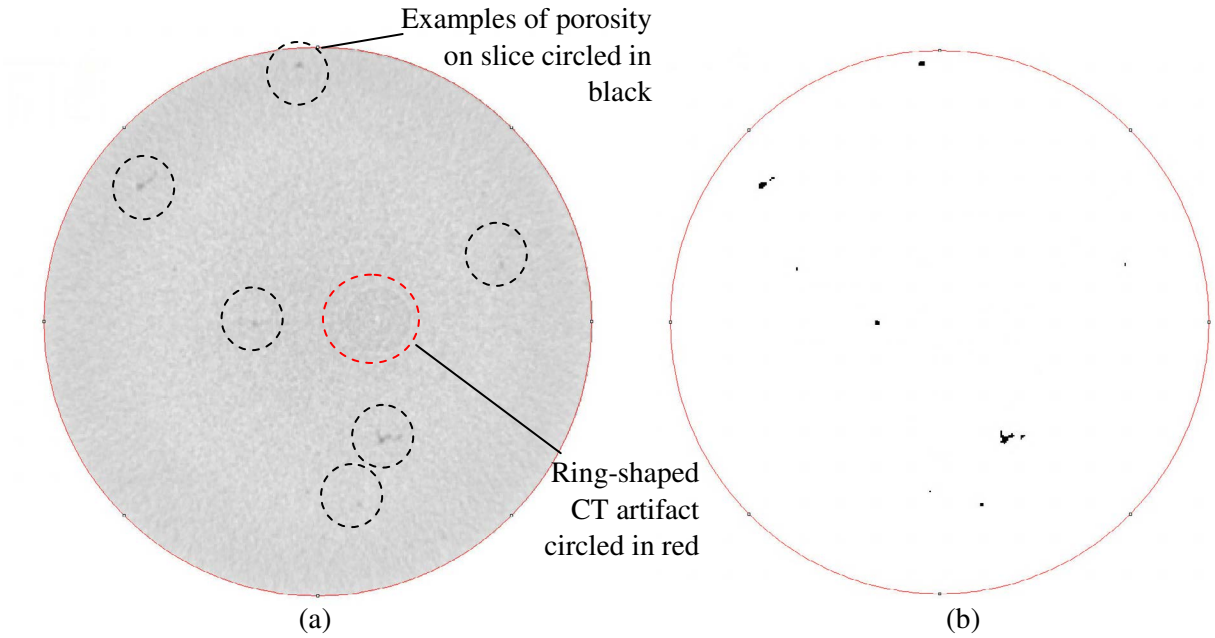

Figure 26 Image of porosity distribution at middle of gage length for specimen UAB-3 taken from UAB wedge casting nearest to the chill.

.

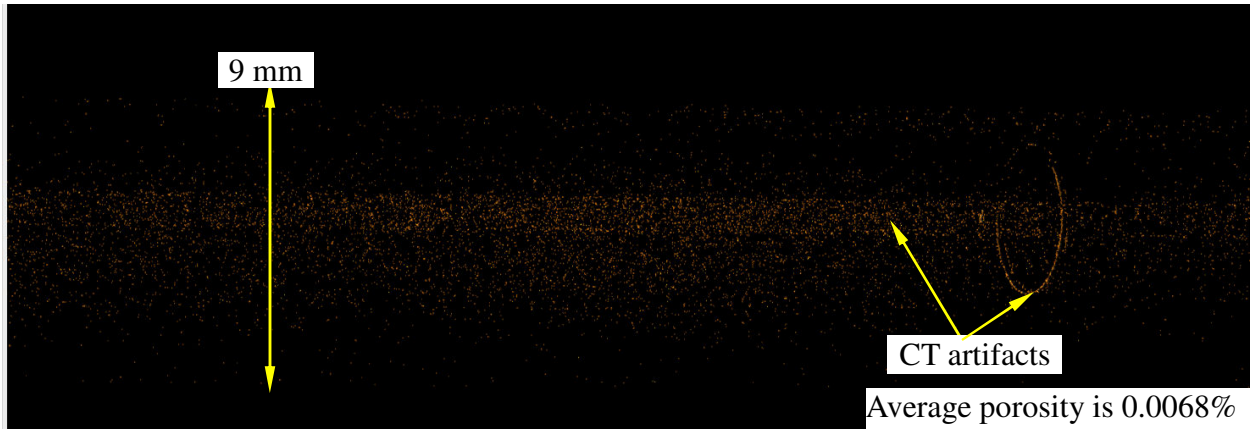

Figure 27 Image of porosity distribution at middle of gage length for specimen UAB-3 taken from UAB wedge casting nearest to the chill.

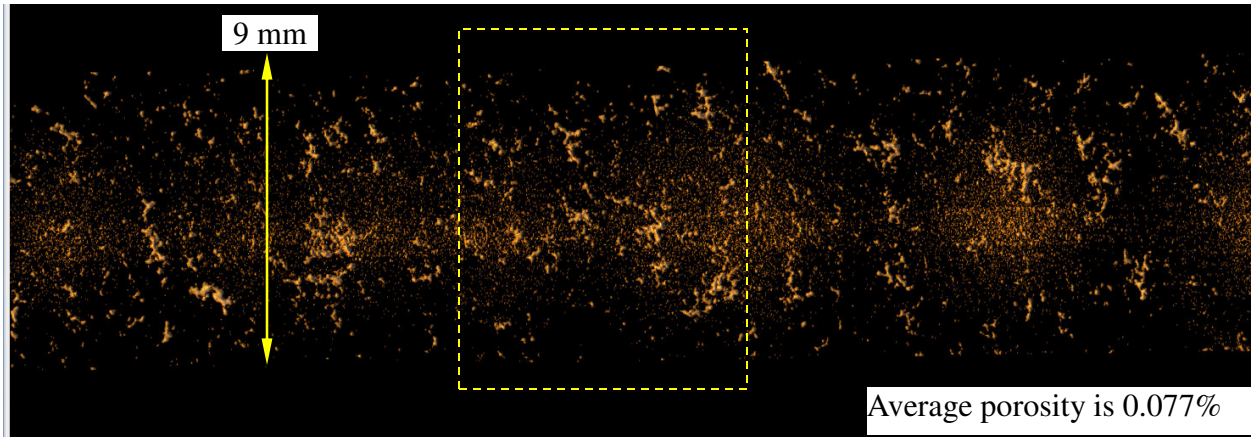

Figure 28 Image of porosity distribution at middle of gage length for specimen A1 taken from tapered disc casting. Area outlined in yellow is shown below in more detail.

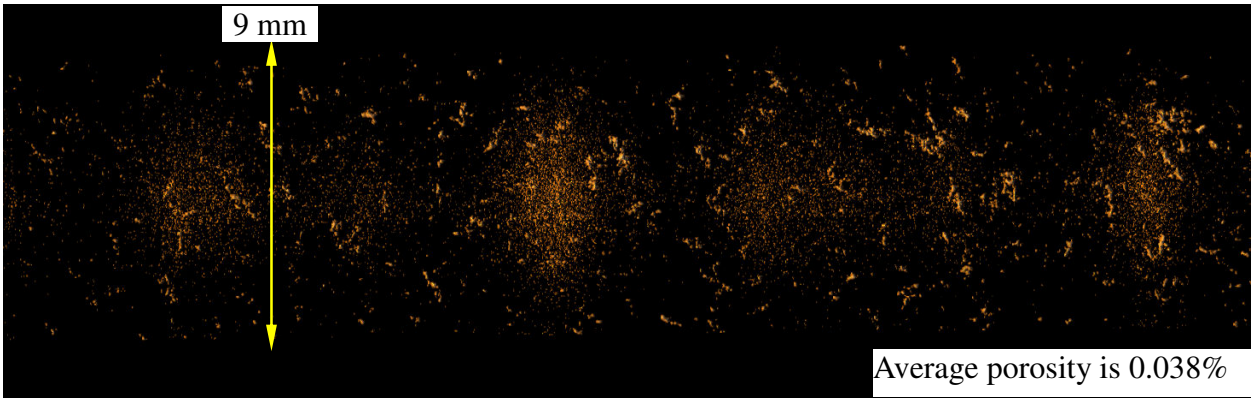

Figure 29 Image of porosity distribution at middle of gage length for specimen F1 taken from tapered disc casting near outer edge.

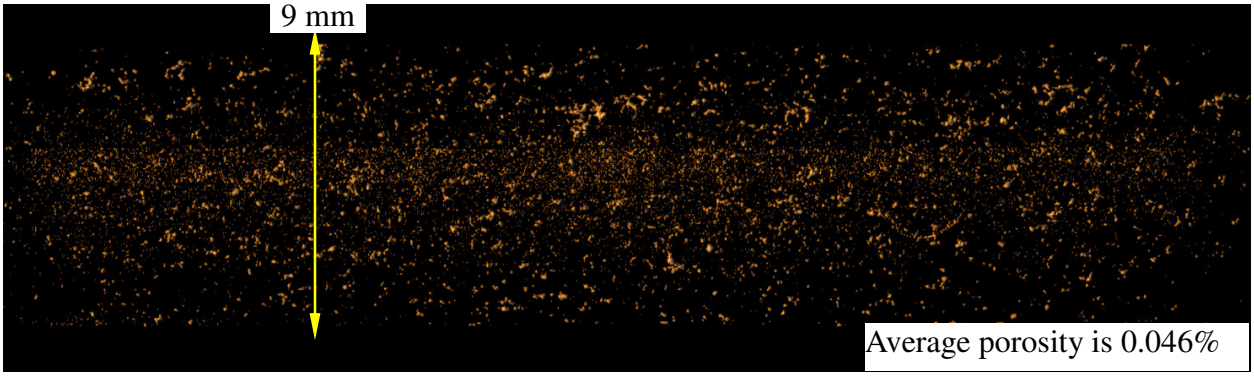

Figure 30 Image of porosity distribution at middle of gage length for specimen C1 taken from 4'x4' plate casting.

The views in these figure show the through thickness distribution of porosity along the middle of the gage length with the specimen length in the horizontal direction. The 9 mm diameter of the specimen is indicated in the figures. Note that only the porosity is visualized, and the average porosity in the specimen volume is shown in the lower right of each figure. The porosity in the wedge casting specimen shown in Figure 27 is extremely fine and is the lowest amount in the CT

specimens analyzed here with an average porosity of 0.007%. The ring CT artifacts that are circled in Figure 27 are caused by miscalibration detectors in the CT hardware. The larger diameter artifact is clearly a ring, while the smaller diameter artifact is an extruded ring or tube extending along the specimen length. Unfortunately, these artifacts were impossible to remove by filtering the images, and they result in an increase in the measured porosity. Still, the porosity level in the wedge specimen is much lower than the material shown in Figures 28 to 30 that were taken from the castings in Figures 3 and 4. The highest porosity level analyzed here 0.077% is in specimen A1 shown in Figure 28 which was from the casting in Figure 3 from a position about halfway between the edge of the disc and the feeder. The porosity in Figure 29 from specimen F1 was taken from the same casting, but near the edge of the diameter. The end effect creates more sound material in specimen F1, and its porosity is about 50% less than specimen A1 (0.038%). The porosity distributions in Figures 28 and 29 are interesting in that both larger pore structures and much finer porosity are present. The fine porosity also appears sometimes in groupings that appear cloud-like, particularly in Figure 29. The yellow boxed region in Figure 28 is magnified in Figure 31 to show the wide range of pore sizes. The shapes of the largest pore structures in this figure are clearly void spaces between the solidifying dendrites forming late in solidification when there is no longer feeding liquid. In comparison with the tapered disc casting porosity, the porosity from the flat 4'x4' plate in specimen C1 in Figure 30 appears more uniformly distributed with less size variation. The porosity level of the flat plate specimen is 0.046% and is in between the two specimens from the tapered disc casting. There do not appear to be the clouds of fine porosity and clusters of larger porosity observed in the tapered disc in the flat plate specimen in Figure 30.

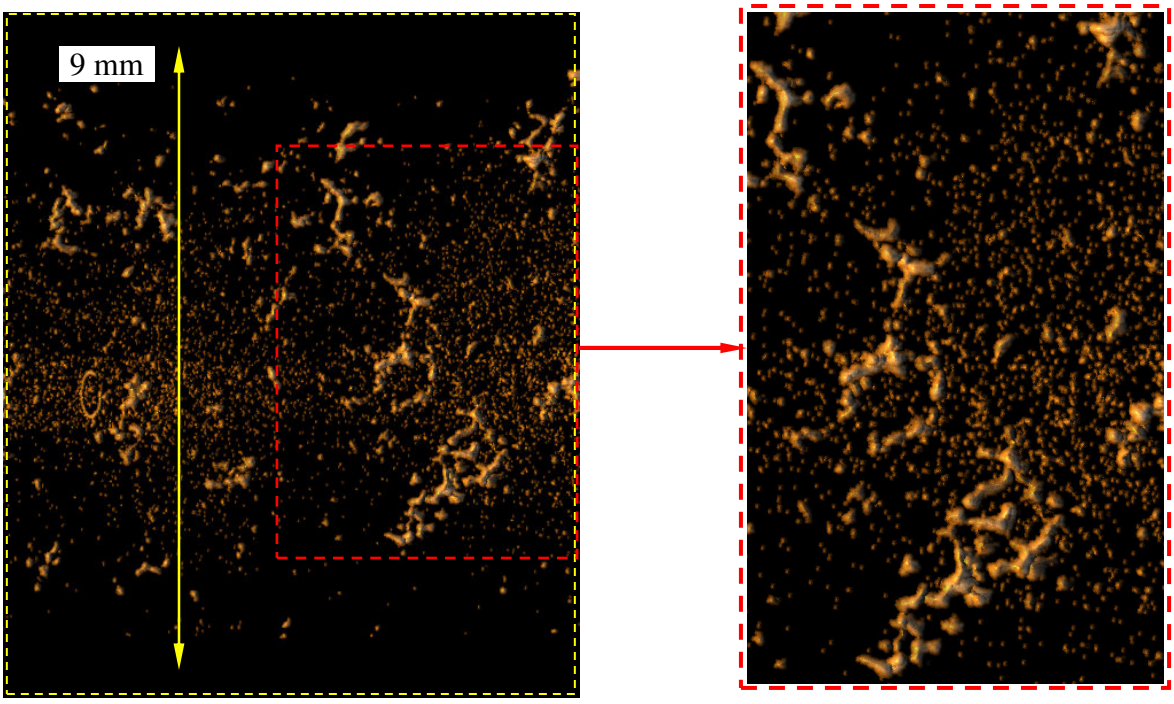

Figure 31 Image of porosity distribution at middle of gage length for specimen A1 taken from tapered disc casting.

Three dimensional measurements of the pore size distributions and characteristics of the pore shapes were not determined with the *ImageJ* software. However, quantitative comparisons of the average cross sectional porosity distributions along the length of the specimens were performed. As shown in Figures 32 to 35, the average porosity in each cross section slice along the specimen length is compared to the volume average porosity. Also where possible, the region of the fracture along the length and the average porosity in the fracture region of the specimen is given. Both ends of the UAB-3 wedge casting specimen were cut for microscopy analysis, so the fracture region in Figure 32 is not indicated. The location of the fracture for specimen UAB-3 might not provide much additional information, since the variation in porosity in Figure 32 is not as great as it is for the other specimens. For specimens A1, F1 and C1, the average porosity in the fracture region is noticeable larger than the average porosity in the specimen being 30%, 63% and 46% greater than the average for the three specimens respectively. For these three specimens, the variability in the specimens' porosity reflected by the standard deviation of the cross section porosity distribution is lowest for specimen C1, from the flat plate at 0.024%, and highest for specimen A1 at 0.052% and the cross section porosity standard deviation is 0.038% for specimen F1.

Ductility measurements *EL%* (black squares) and *RA%* (red triangles) for the high strength steel versus the average specimen porosity from the CT data are shown in Figure 36. The data show a nice trend of increasing ductility with increasing porosity, except for the F1 data points (data points shown connected by a dashed line). Clearly even a small amount of porosity can adversely affect the ductility. Note, however, that there is physically contradictory behavior

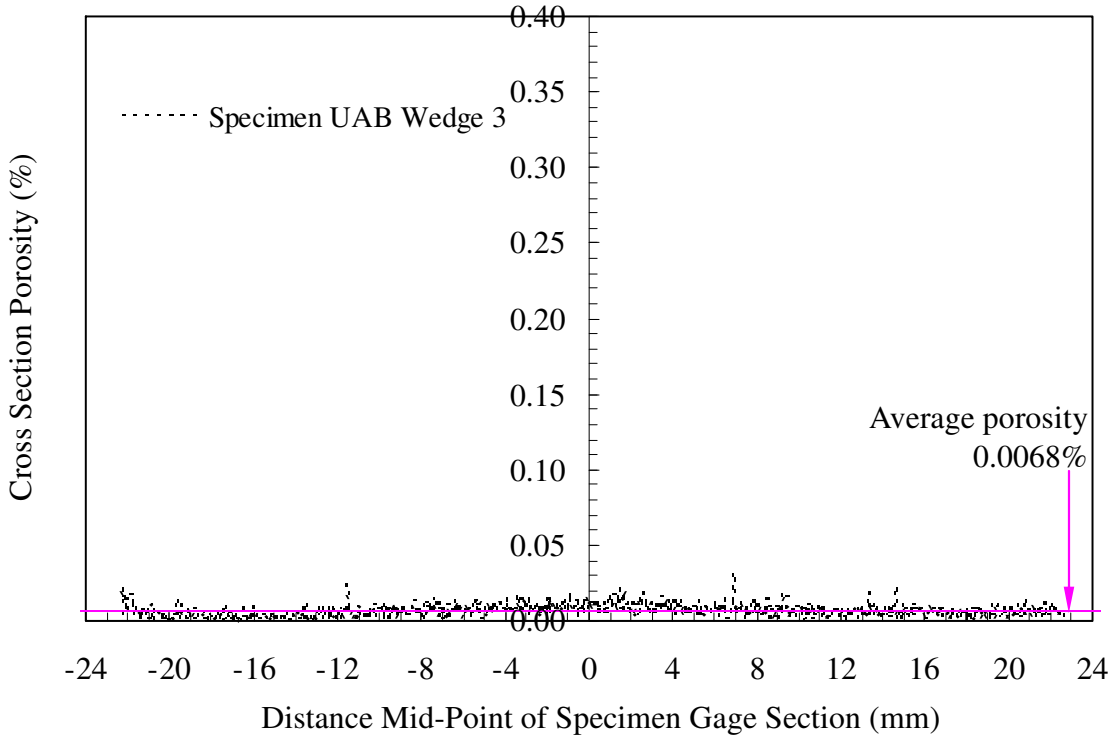

Figure 32 Average porosity in cross section slices along the UAB-3 wedge casting specimen length is compared to the average porosity in the specimen volume (magenta line).

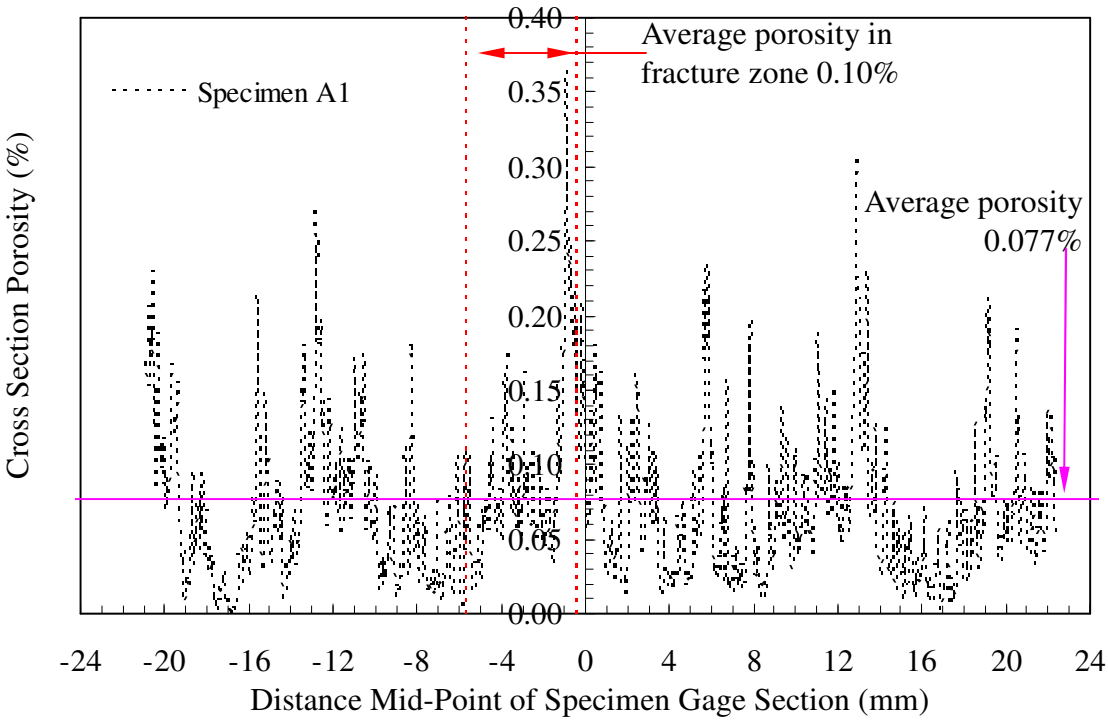

Figure 33 Cross section porosity slices along the specimen length compared to the volume average porosity (magenta line) and the fracture region porosity for A1 tapered disc specimen.

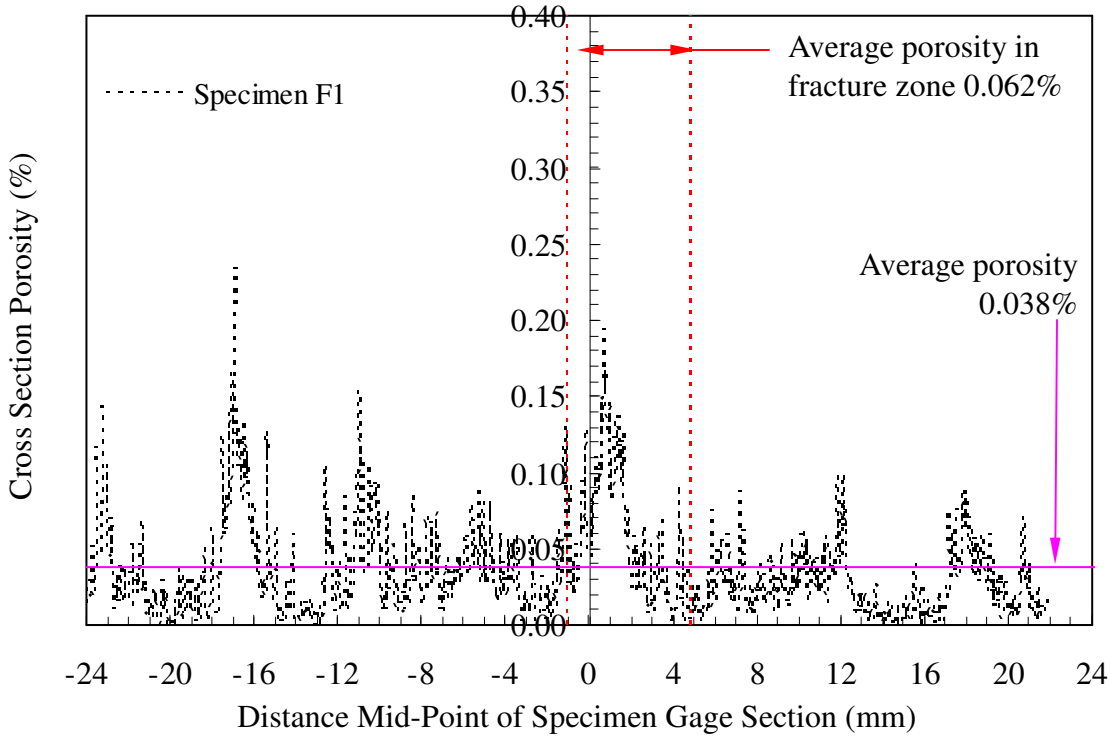

Figure 34 Cross section porosity slices along the specimen length compared to the volume average porosity (magenta line) and the fracture region porosity for F1 tapered disc specimen.

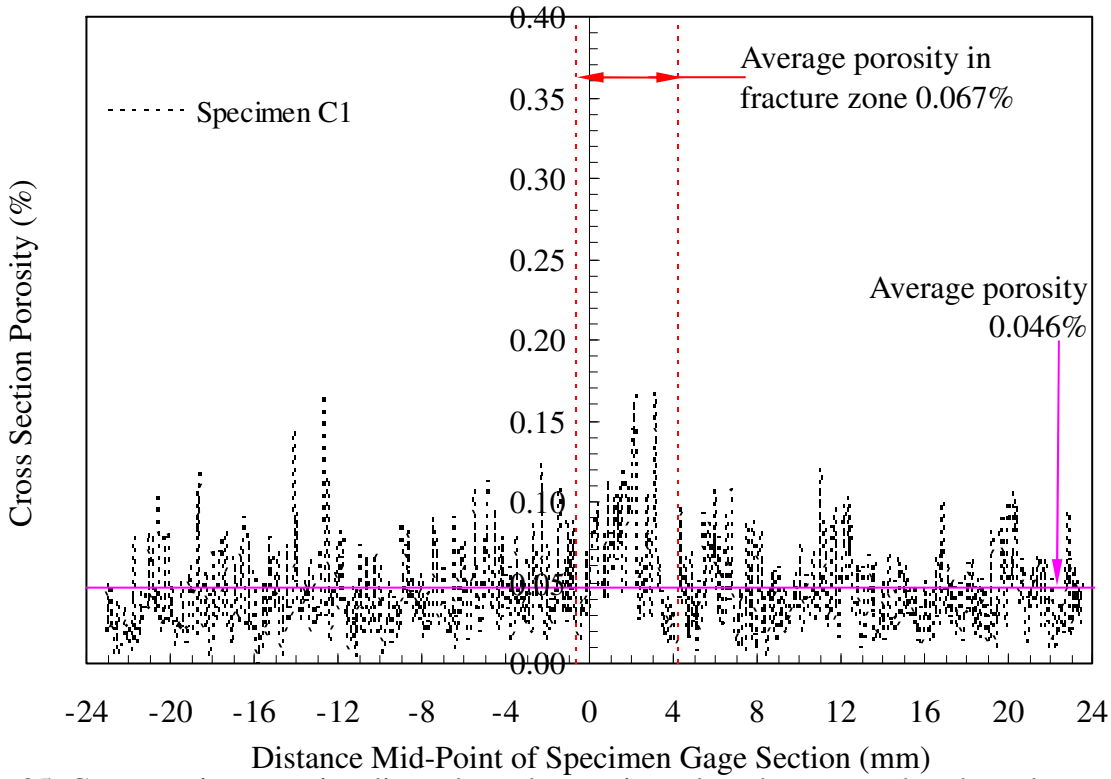

Figure 35 Cross section porosity slices along the specimen length compared to the volume average porosity (magenta line) and the fracture region porosity for C1 the 4' x 4' plate specimen.

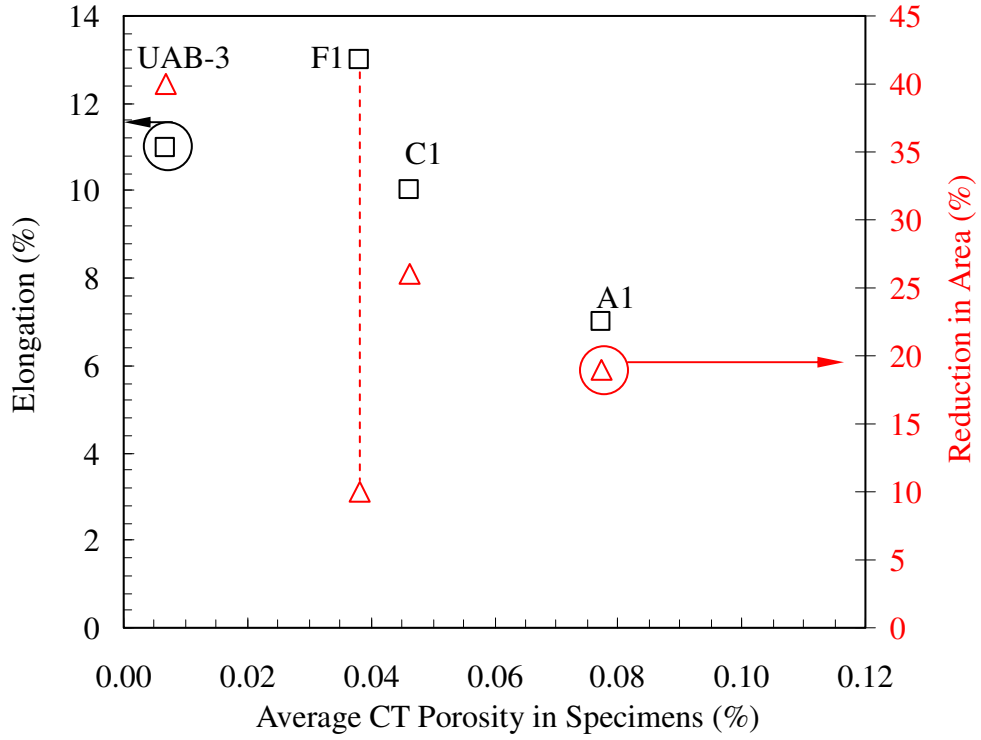

Figure 36 Ductility measurements *EL%* (black squares) and *RA%* (red triangles) for the high strength steel versus average specimen porosity.

in the ductility data for specimen F1. Looking at the data values from Table III, specimen F1 has the highest elongation and the lowest reduction in area of the specimens; the measurements do make physical sense. The only one half of the broken specimen was available to re-measure the *RA%*, and this was performed multiple times by the authors. The largest *RA%* measured out of ten repeated measurements was 13%. Without the other half of the specimen *EL%* could not be re-measured. The plot of ductility measures *EL%* and *RA%* are plotted versus the average porosity in the fracture region in Figure 37, except for specimen UAB-3 where the average specimen porosity is re-plotted from Figure 36. Note the scale change from Figure 36, and that the data shifts to higher values when plotting the average porosity in the fracture region.

Table III Porosity measured from CT data in entire specimen and in the fracture zone region, and tensile test measurements for specimens scanned using x-ray CT.

Specimen	**Average CT Porosity (%)**	**Average CT in Fracture Zone Porosity (%)**	**UTS (ksi)**	**YS (ksi)**	***%EL***	***%RA***
UAB-3	0.0068	-	235.9	180.6	11	40
A1	0.0773	0.1	236.9	204.1	7	19
C1	0.0464	0.062	237	182.2	10	26
F1	0.038	0.067	268.1	194.6	13	10

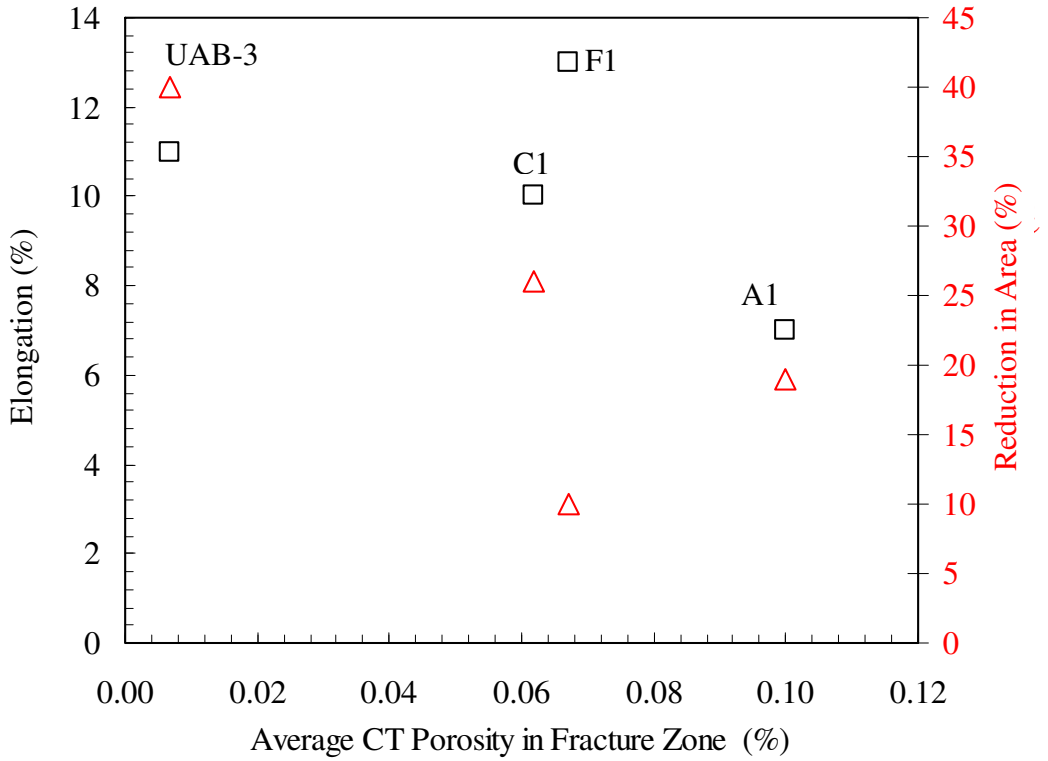

Figure 37 *EL%* and *RA%* plotted versus the average porosity in the fracture region, except for specimen UAB-3 where the average specimen porosity is re-plotted from Figure 35.

The predicted porosity fields at the CT specimen locations are shown in Figures 7 and 38 using sensitive microporosity level scales. The range of porosity was determined within the specimen region, and the mid-point of the predicted range is plotted in Figure 39 where it is compared to the CT measured average porosity. In this figure the error bars for the predictions indicate the range of the predicted porosity. In Figure 7 a vertical slice through the casting is shown on the mid-width plane for the UAB-3 wedge casting specimen, where the predicted porosity is higher than the porosity determined from the CT scan. The porosity predicted in the tapered disc specimens are shown in Figures 38 (a) and (b) (A1 and F1, respectively). This shows perfect agreement for the predicted and measured porosity in specimen F1. While for specimen A1, the measured porosity is higher than the predicted. For specimen C1 from the flat 4' x 4' plate in Figure 38 (c), the porosity is overpredicted, but the prediction within the specimen region has a wide range. The correlation between the predicted and measured porosity from the CT scan is not strong, as seen in Figure 40. In this figure it is clear that for predicted porosity data around 0.04% one can obtain a large range of ductility properties. More data for comparison from trial castings in foundries, as was shown for the wedge casting in Figure 21, might provide a better answer as to whether porosity predictions can be used to predict mechanical properties. However, based on the data available, as was plotted for example in Figures 19, 20, 22 and 23 for the wedge castings, it was decided by the authors in consultation with the SFSA to use cooling rate directly as the basis of developing a ductility predictor for this high strength steel instead of SDAS.

Development and Results of a High Strength Steel Ductility Predictor Based on Cooling Rate

Given the significant correlation between ductility and SDAS (Figure 19), and SDAS and cooling rate (Figure 22 and Equation 2), a ductility predictor for use in casting simulation software was developed based on cooling rate for the high strength steel considered here. This predictor is only useful for the high strength steel given in Table I when heat treated according to best practices determined by Van Aken et al. [1]. Here the predictor is used in the casting simulation software *MAGMAsoft's* based on its solidification cooling rate result to predict the elongation to failure varying throughout the casting. The predictor is general and applicable in any solidification simulation software as solidification cooling rate is a common result; it is the solidification temperature interval (difference between the liquidus and solidus temperatures) divided by the solidification time interval. Elongation is chosen as the measure of ductility to be calculated using predicted cooling rates from casting simulations.

The predicted cooling rates at the tensile specimen locations are given in Figures 41 to 44 for the wedge castings, the tapered disc casting, the flat 4' x 4' plate casting and the weld plate casting, respectively. The range of cooling rates in the wedge castings is the largest, from 0.12 to over 3.5 (°C/s) as seen in Figure 41, where the tensile test ductility data are given for the seven specimen locations for comparison to the cooling rate plot. The consistently lowest *EL%* data was found in the weld plate casting where the elongation ranged from 2% to 3% in Figure 44. Collecting all the elongation data, numerous forms of best-fit equations using cooling rate as the independent variable were tested. The data are plotted in Figure 45. It was decided to use an equation form that would reach a limiting value of elongation in order for the prediction to be conservative at high cooling rates. The best-fit equation used for *EL%* versus cooling rate is

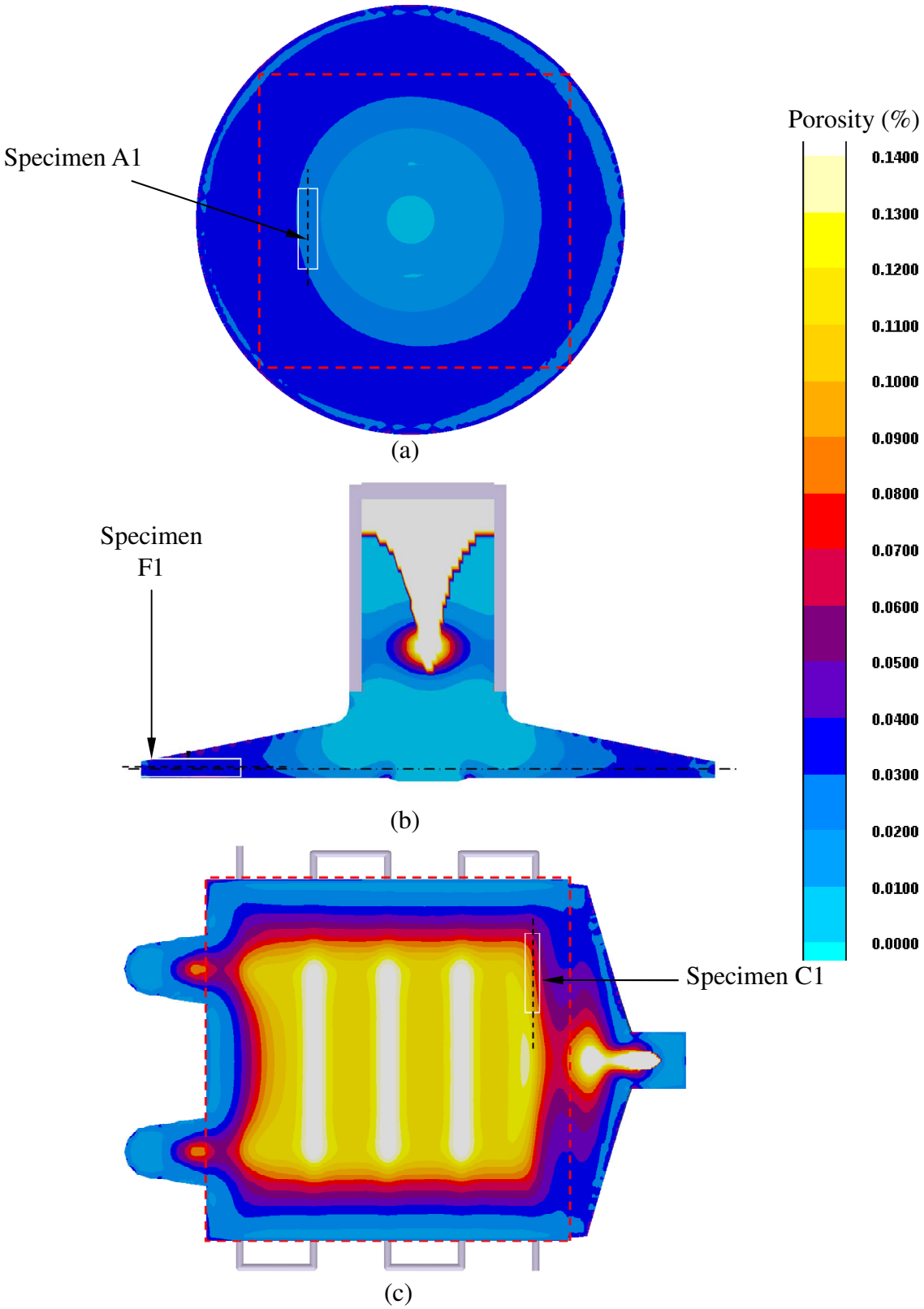

Figure 38 Porosity predictions at CT specimen locations on microporosity scale for (a) A1 and (b) F1 the tapered disc, and (c) in the flat 4' x 4' plate.

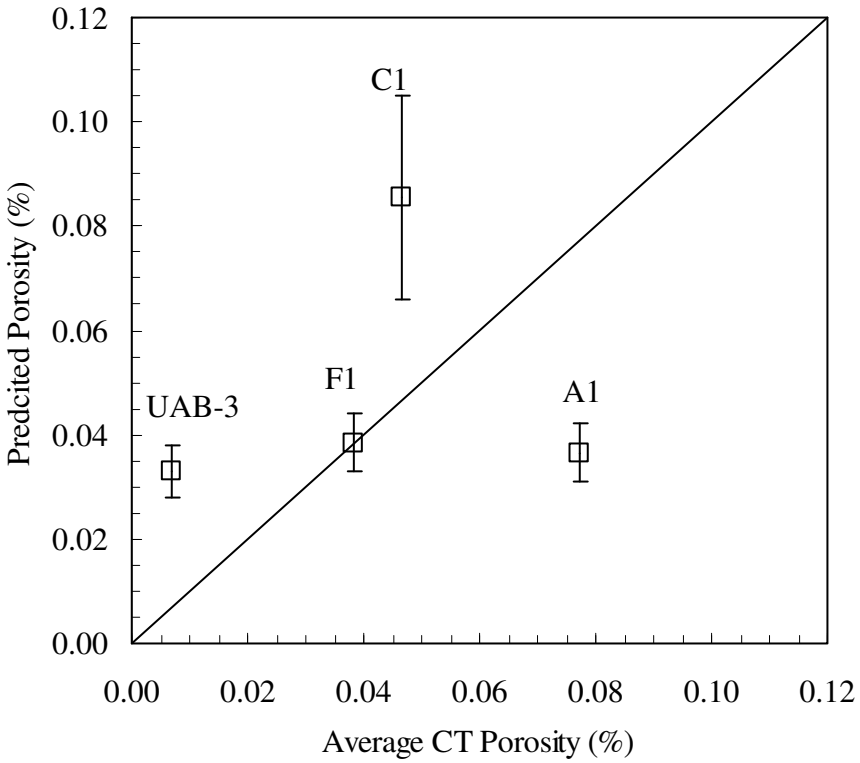

Figure 39 Predicted porosity within the specimen volumes versus average porosity in CT scans of specimens.

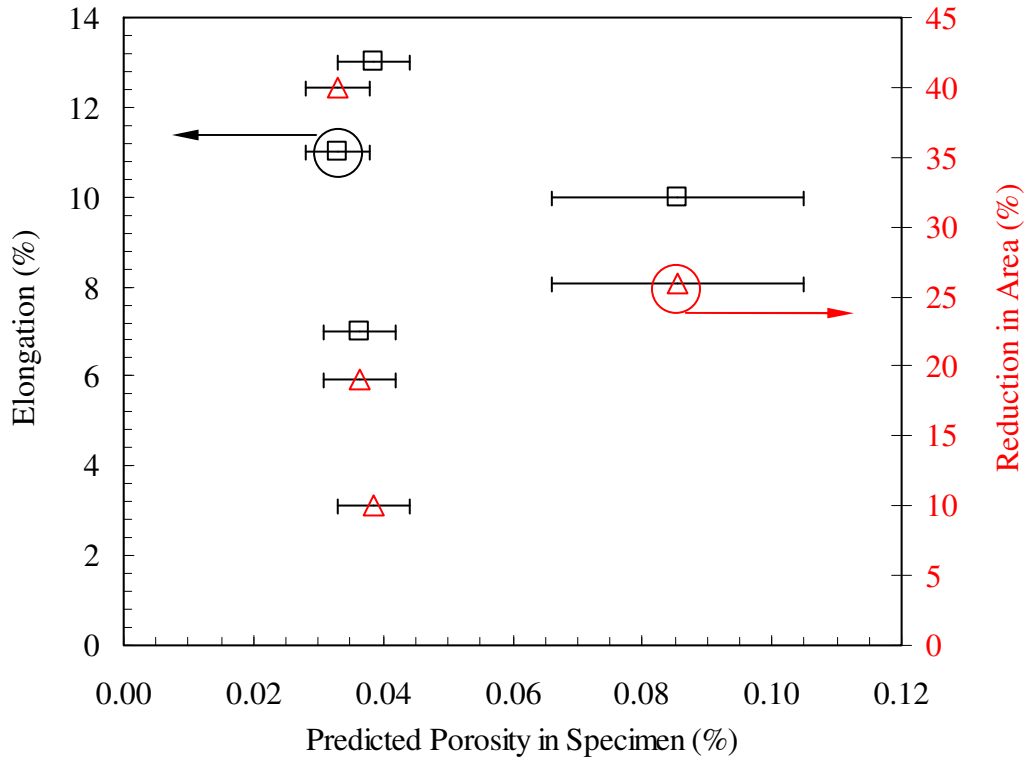

Figure 40 *EL%* and *RA%* plotted versus the predicted porosity in the CT scanned specimens.

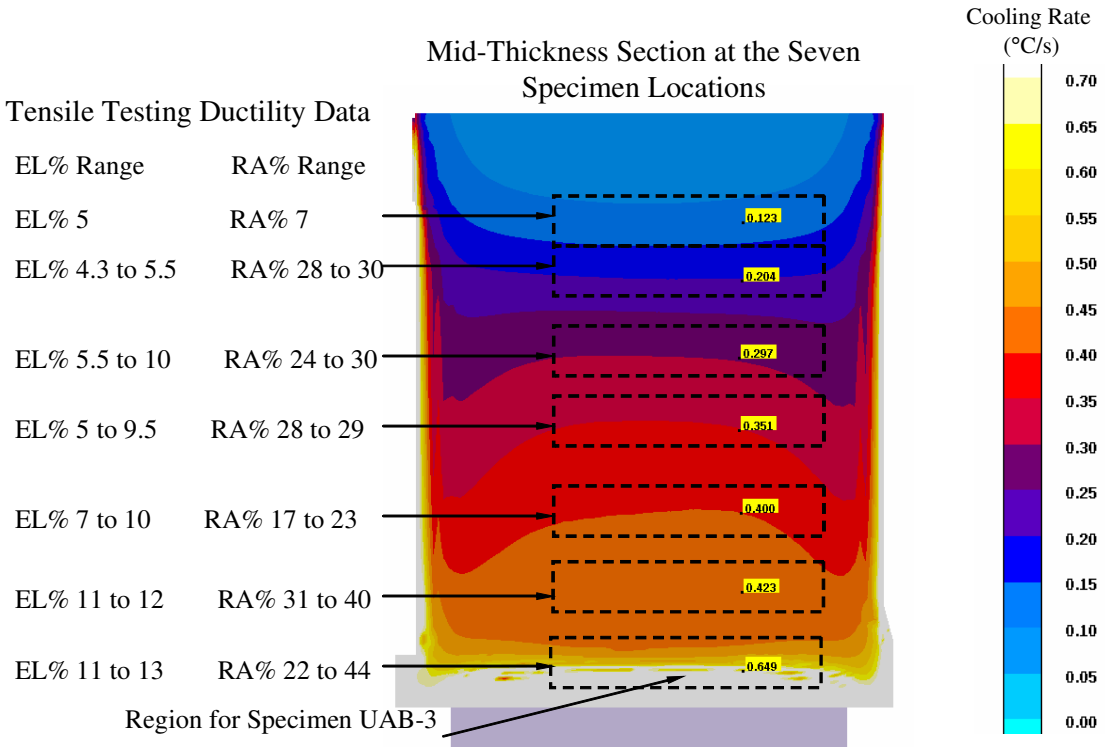

Figure 41 Predicted cooling rates at the seven wedge casting specimen locations and the ranges of ductility measurements from tensile testing from the locations.

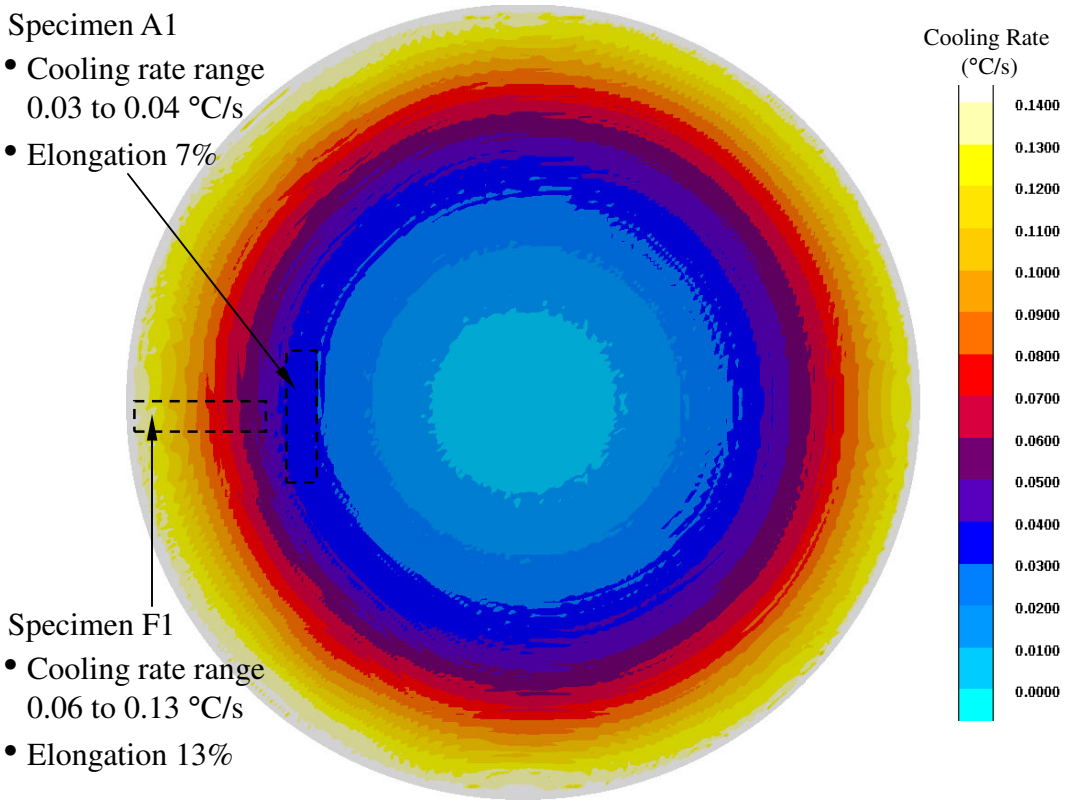

Figure 42 Predicted cooling rates at specimen locations A1 and F1 in the tapered disc casting.

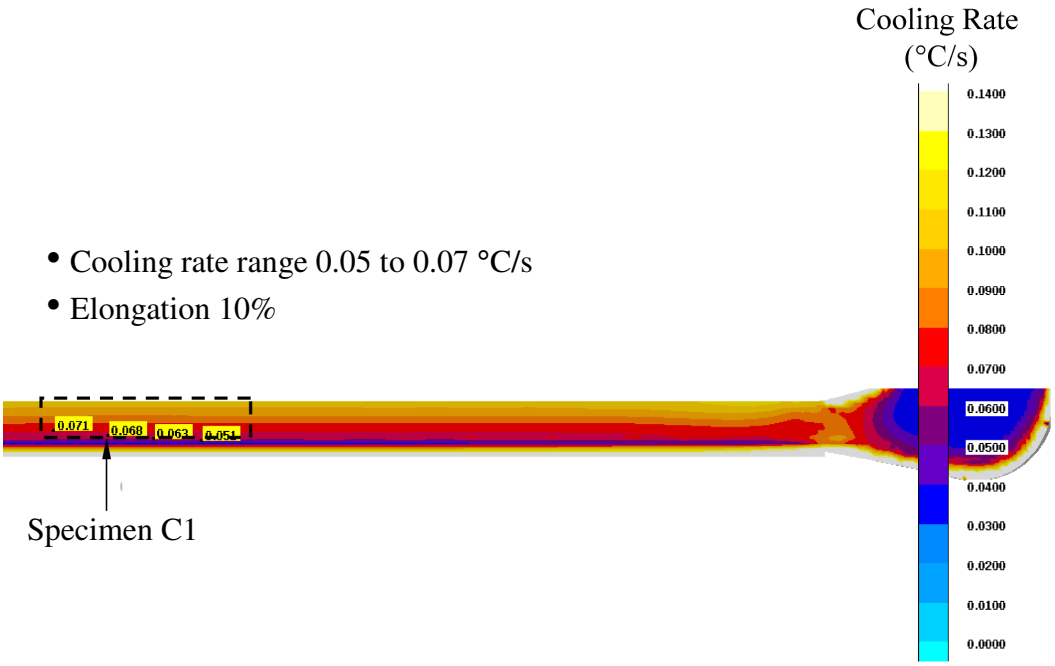

Figure 43 Predicted cooling rates at specimen location C1 in the 4' x 4' plate .

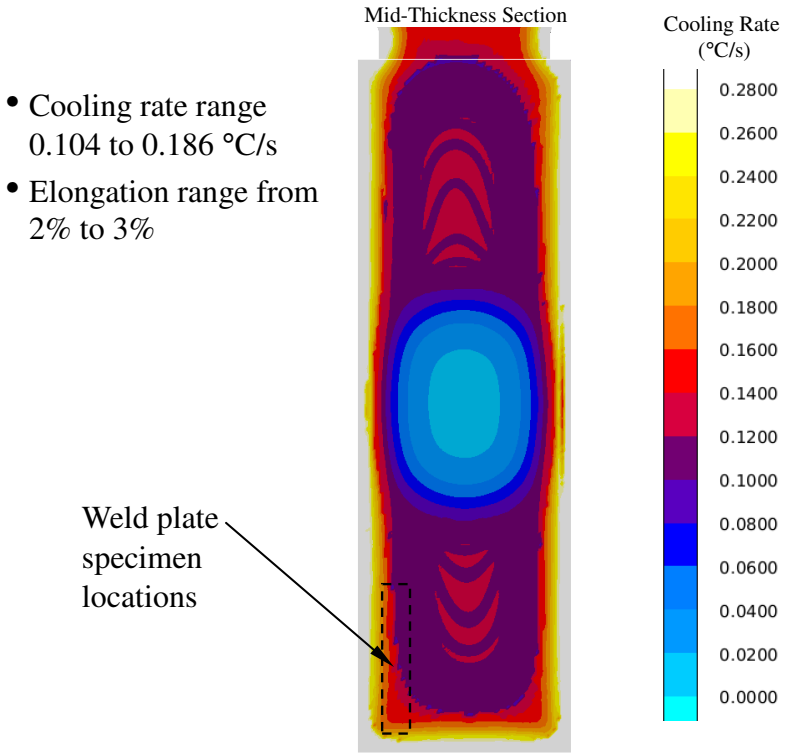

Figure 44 Predicted cooling rates at the weld plate casting tensile specimen locations.

$$EL\% = 10.6057(1 - \exp(-2.8742 \cdot \dot{T})) \quad (3)$$

This curve is plotted as the dashed line in Figure 45. Clearly the measured data (the symbols) in Figure 45 show that at low cooling rates the complete range of measured elongation are observed. It has been shown that porosity is also a variable that affects the ductility, but that all data presented here contains microporosity below 0.1%. It is also recommended that the predicted porosity should be below 0.04% in order to use Equation (3) for more confident elongation predictions.

Equation (3) has been applied in *MAGMAsoft* as a user result to predict elongation and optimize casting processes to produce the high strength steel given in Table I with increased confidence that the material will have the best possible ductility. A comparison between the measured elongation to failure and the predicted elongation from casting simulation is shown for all wedge, CT scanned and weld plate data in Figure 46. Overall, there is fairly good agreement between them with the weld plate data providing bounding data for low ductility. The predicted elongation appears to be on the conservative side at higher elongations and non-conservative at lower elongations. The high cooling rate casting data show that the prediction is conservative when the predicted elongation is about 10% or greater. The predicted results can be used in applications as indicating that for a level of 10% the casting is likely to have the best ductility possible. Note that in areas under risers a lower elongation will be predicted despite the lower porosity level. For the high strength steel used here, there is anecdotal evidence of this in some casting applications. However, a controlled study needs to be undertaken to demonstrate that low cooling rate is the variable responsible for ductility loss under risers for this high strength steel.

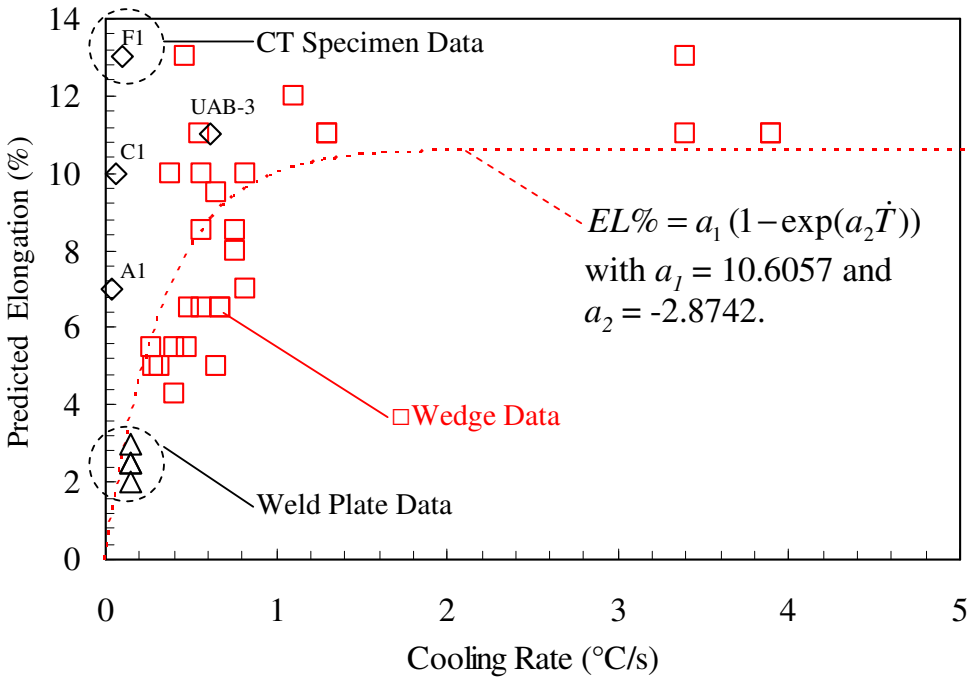

Figure 45 Elongation of high strength steel specimens from all castings vs. predicted cooling rates with best fit curve (red dashed line). CT scan specimens are diamonds, wedge casting data are red squares and weld plate data are black triangles.

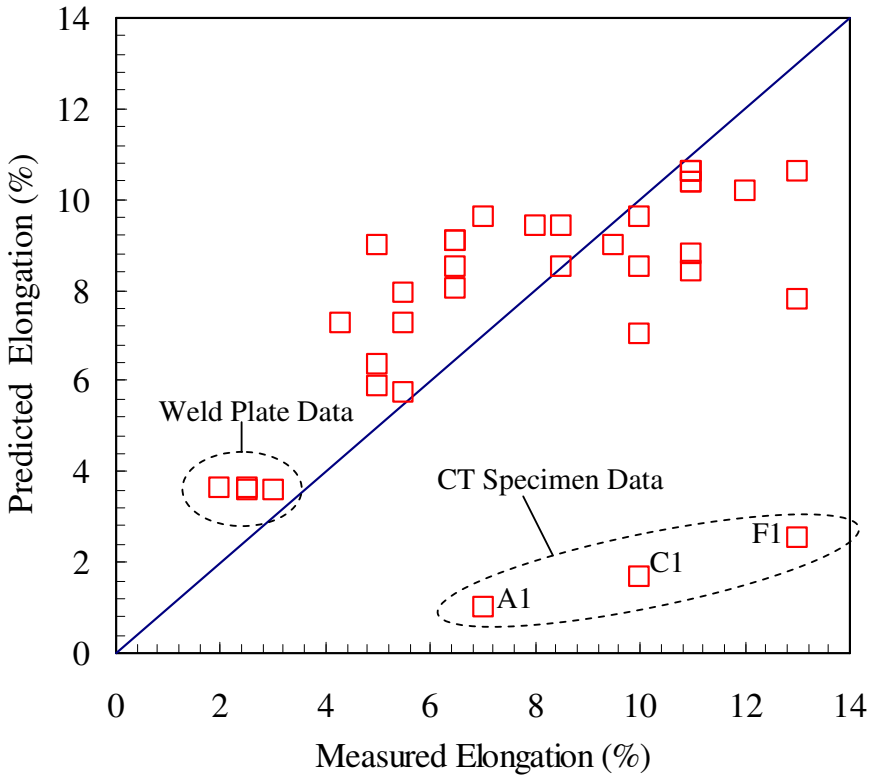

Figure 46 Predicted versus measured elongation for all tensile specimens.

The elongation predictor is useful in comparing the effects and tradeoffs between cooling rate (microstructure and SDAS) and porosity level on ductility for casting designs and rigging configurations using this high strength steel.

Results Section 2: Mold Materials for Increased Cooling Rates and Ductility

Measured and Predicted Temperatures Steel Shot Molds and Shot-Specialty Sand Mixes

Using the weld plate casting rigging shown in Figure 5, six types of drag molds were instrumented with thermocouples and cast at an SFSA member foundry. Two thermocouples were place in the castings and two in the mold material for each type of mold material investigated. Platinum-platinum rhodium thermocouple sensors (B-type) were built by the authors for the metal temperature measurements, and K-type thermocouples used for the mold measurements. Using the measured temperature data, the relative chilling capabilities of the mold materials can be compared. In addition to analyzing the experimental data, numerous iterative casting simulations were performed using MAGMAsoft, where the temperature dependent mold properties in the simulations were modified such that agreement was obtained between measured and predicted temperatures. This iterative/comparative process for determining simulation properties is referred to as *inverse modeling*. These resulting properties for the mold material types can then be used in development of casting processes to better control and increase cooling rates to achieve optimum steel properties using the cooling rate dependent ductility prediction in Equation (3).

The six mold material castings that were instrumented with thermocouples are referred to as Casting 1 through Casting 6 as described below:

- Casting 1 – used an all silica sand mold, referred to also as a "control case" casting, its results are used to determine steel properties for all experiments and silica mold properties.
- Casting 2 – used steel drag chills 2" thick covering the whole drag surface, consider it the best possible case for chilling the casting.
- Casting Case 3 – drag uses 2" facing mold is steel shot with highest density possible covering entire drag mold
- Casting Case 4 – drag is steel shot and chromite sand mix 50/50 by volume
- Casting Case 5 – drag is steel shot and zircon sand mix 50/50 by volume
- Casting Case 6 – drag has 1" facing mold of steel shot and then backed by 50% of the area covered with 1" chills.

The mold material experiments were cast using the weld plate pattern shown in Figure 5. Two types of mold material were cast in each mold box as seen in Figures 47 to 49. Mold material Casting 1 and Casting 2 were poured in one mold box as seen in Figure 47, Castings 3 and 6 were poured in another mold box as shown in Figure 48, and mold material Castings 4 and 5 were poured in another mold box as shown in Figure 49. The order of pouring was Castings 1 and 2 cast together in 1st mold box poured, Castings 4 and 5 cast together in 2nd mold box poured, and Castings 3 and 6 cast together in 3rd mold box poured. As shown in Figures 47 to 47, for each casting-mold type combination four thermocouples were used to record metal and mold temperatures. In each case, the two thermocouples (TCs) were placed in the metal, with one in the plate under the feeder (labeled TC1) and the second metal TC at plate mid-thickness and mid-length to the plate end (labeled TC2). The TCs placed in the mold material on the drag side of the casting were similarly positioned with one in the drag-side mold under the feeder (labeled TC3) and one in the mold mid-length to the plate end (labeled TC4). For Casting 2 in Figure 47, note that the drag mold TCs were positioned at the outer surface of the solid steel chills, and were not embedded in the solid chills. Note in setting up the experimental measurements it was not possible to place the metal thermocouples identically at the same locations in each casting due to variability in drilling the molds and variations in the lengths of the TCs used. Though not identically positioned in all castings, the metal TC positions in the experiments were known within 1 mm since their positioning was carefully measured in the mold cavity. This variation in position is clear if one looks closely at the positions of the TC1 and TC2 positions in the castings in Figures 47 to 49.

After the experiments were performed, the temperature measurements for the control casting (Casting 1) were used to determine the temperature dependent metal and silica mold properties which gave the best agreement between measured and simulated temperatures. These resulting metal and silica mold properties would be used in the simulations that followed for all the mold materials. The Casting 1 measured and predicted TC data are given in Figure 50, where

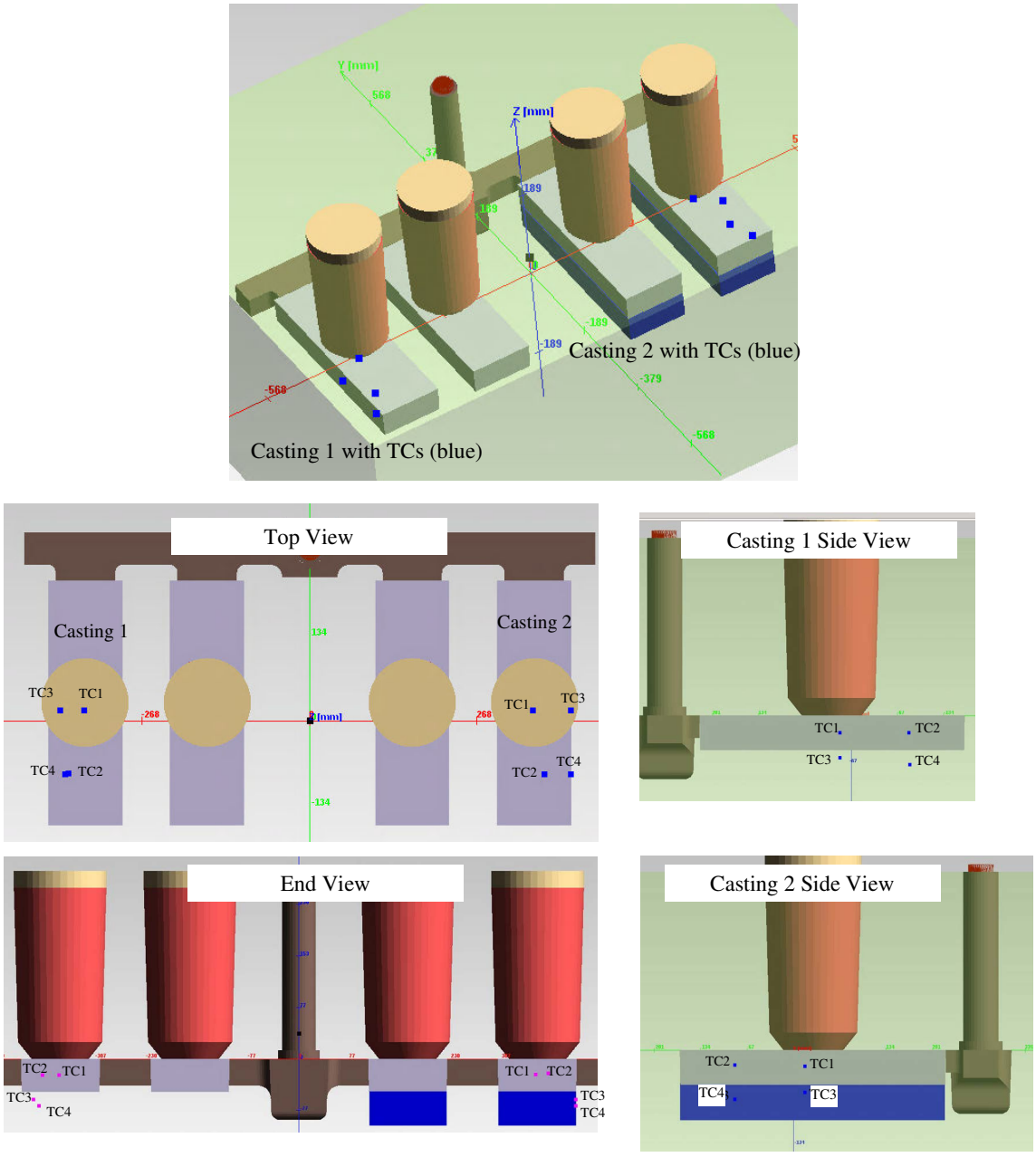

Figure 47 Casting simulation model geometry of Castings 1 and 2 mold box with the four thermocouple positions indicated by blue points and labeled in each TC1 through TC4.

red curves will denote measured temperatures and black curves predicted temperatures. In the temperatures-time plots for all mold materials that follow this coloring convention is followed. As seen in Figure 50 (and all similar figures that follow), the TCs use solid lines to denote TC1 in the metal and TC3 in the mold, and dashed lines denote TC2 in the metal and TC4 in the mold. This coloring and line type convention are also indicated in all temperature-time plots for the mold material measurements and predictions in Figures 50 through 55. Looking at the Casting 1 results in Figure 50, from the first mold box poured, there was not much superheat measured. In the authors' experience with using inverse modeling to determine casting

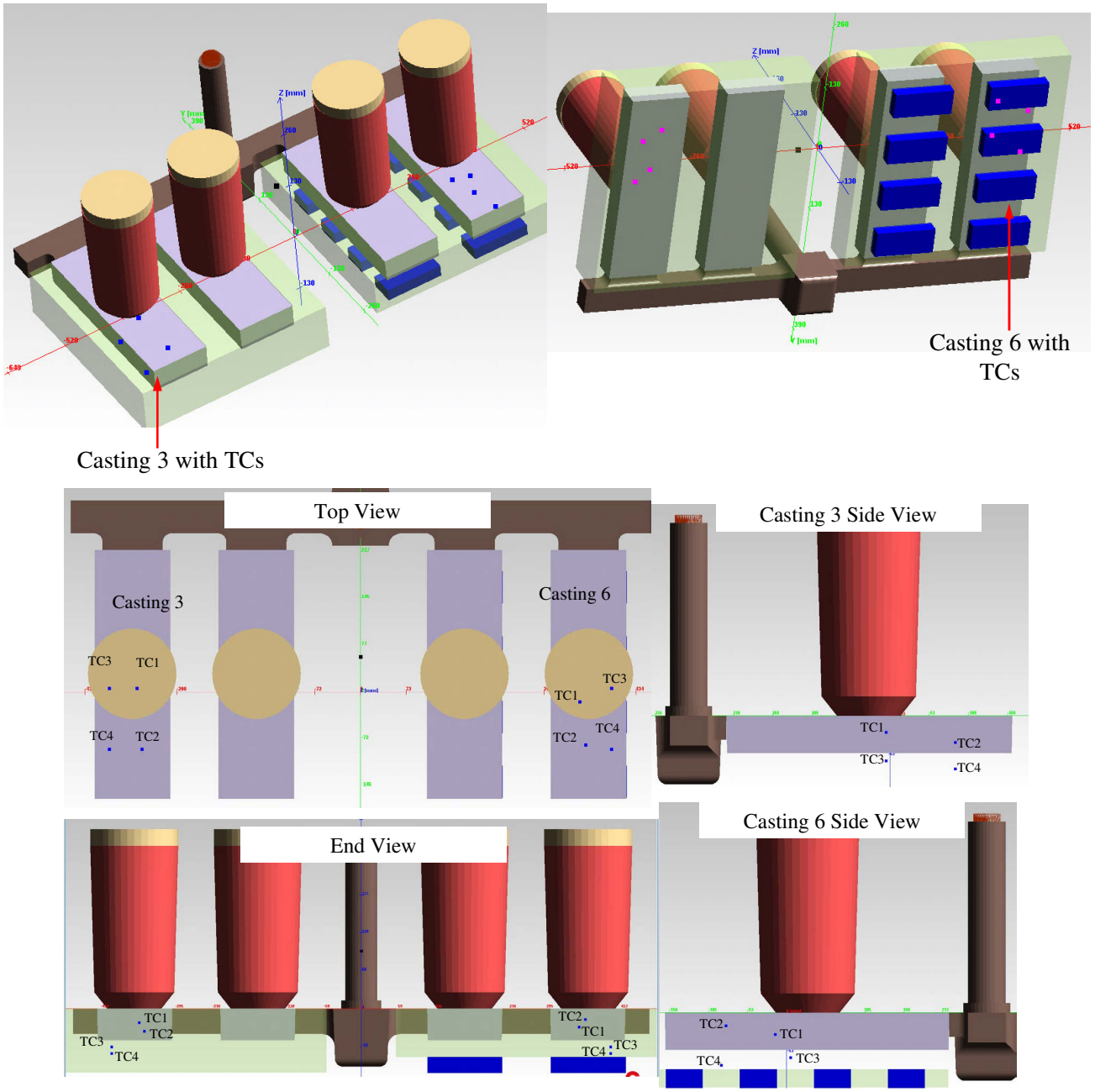

Figure 48 Casting simulation model geometry of Castings 3 and 6 mold box with the four thermocouple positions indicated by blue points and labeled in each TC1 through TC4.

simulation properties, it is advantageous to capture the cooling down of the liquid metal from at least 10°C to 20°C of superheat so the liquidus temperature and start of solidification is clearly delineated. Despite this issue, the properties determined for the metal and mold produced good agreement for Casting 1 seen in Figure 50. Similarly, the Casting 2 results between predictions and measurements for TC2, TC3, and TC4 look excellent for the solid steel drag chill. For this casting, the TC1 data in Figures 51 (a) and (b) clearly show the failure of that sensor on initial heating resulting in a lower, erroneous, temperature measurement compared to the simulation.

The

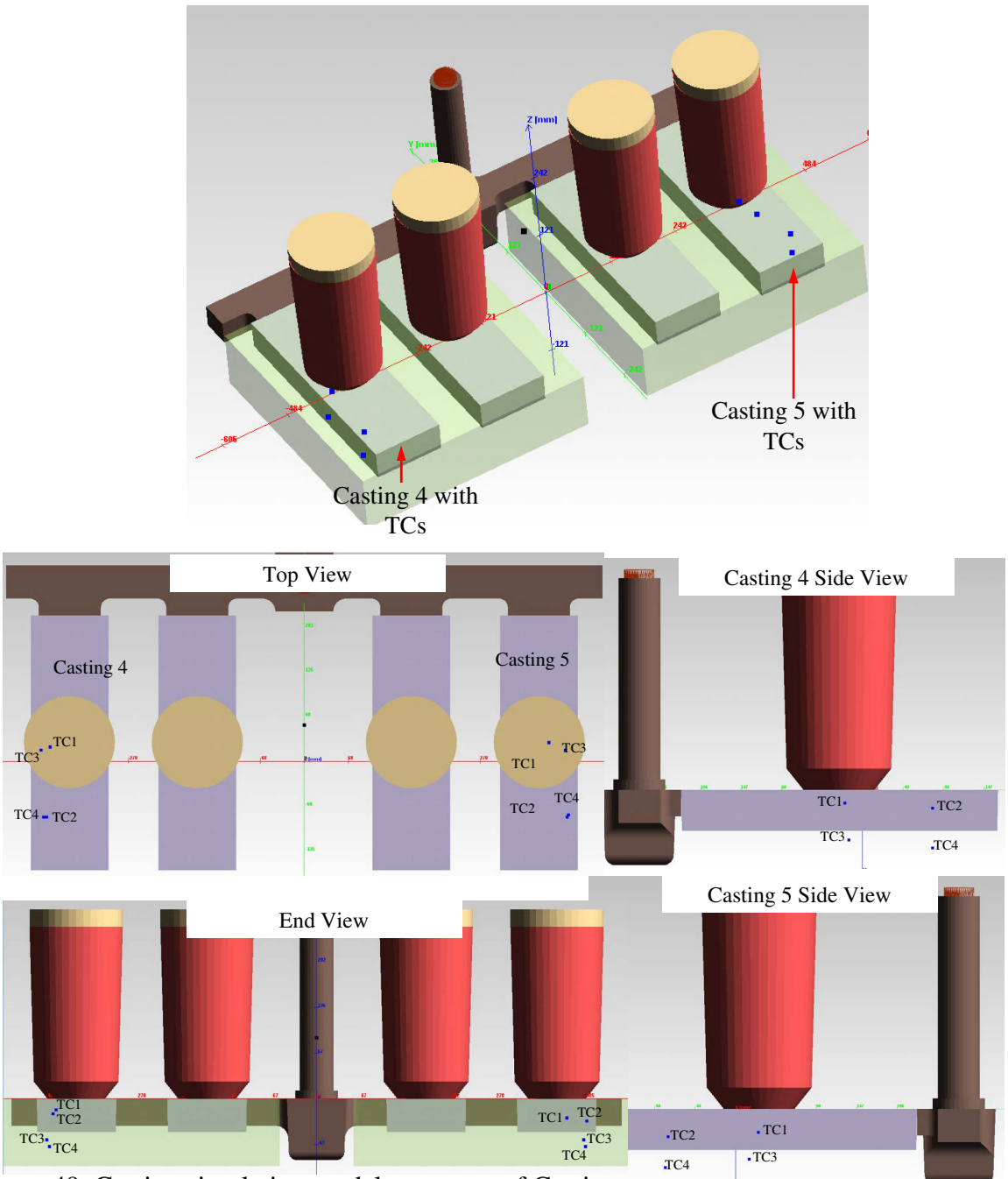

Figure 49 Casting simulation model geometry of Castings 4 and 5 mold box with the four thermocouple positions indicated by blue points and labeled in each TC1 through TC4.

solid steel chill data from the *MAGMAsoft* database was used to produce these results, and they give good agreement as seen in Figure 51.

The steel shot chill material was used as the drag mold in Casting 3. For this case, the mold properties were determined such that excellent agreement with measurement is observed at the metal TCs in Figure 52. The temperature at TC4 in the mold appears to be overpredicted. The

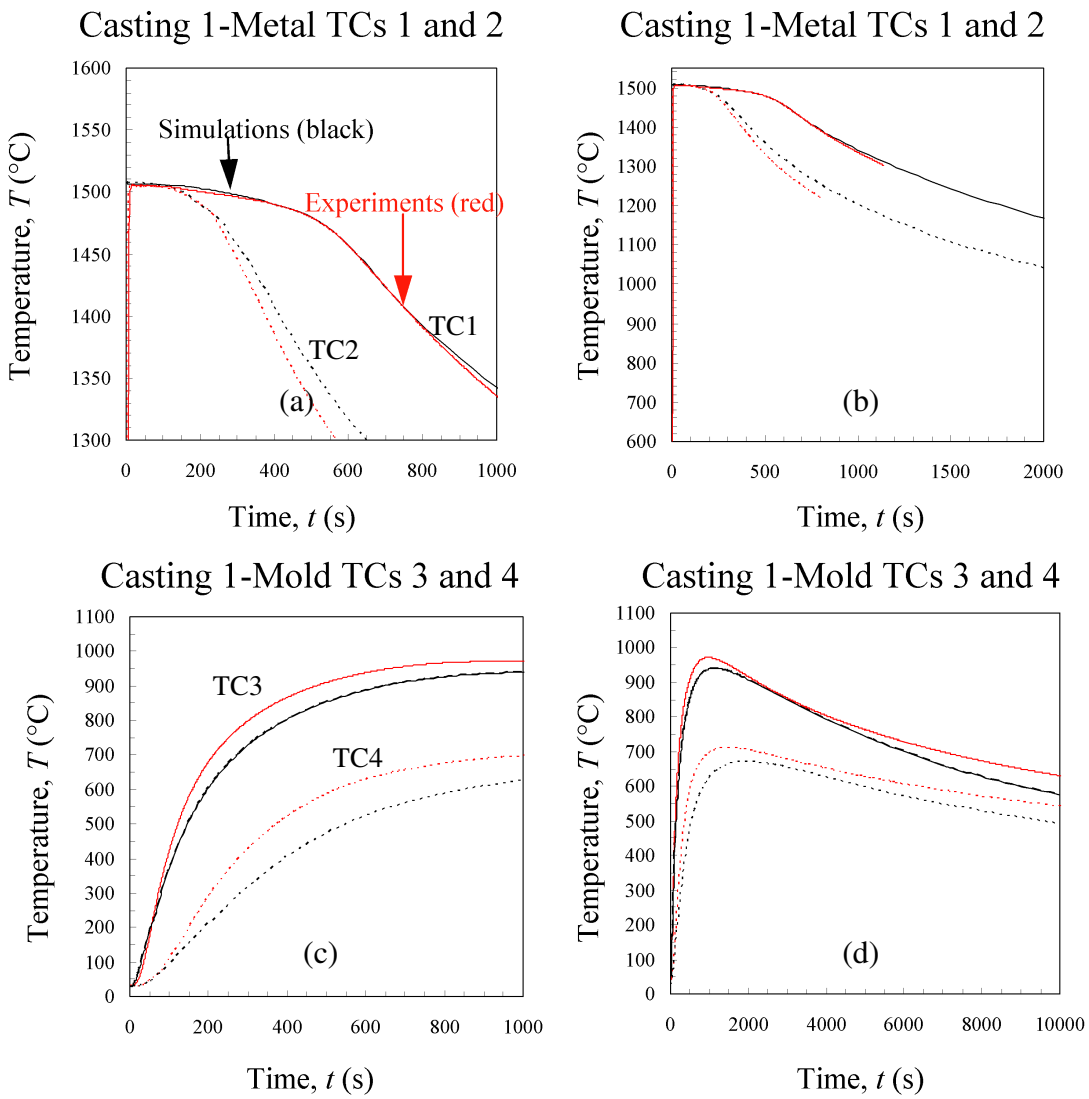

Figure 50 Measured and predicted TC data for control experiment Casting 1 with (a) and (b) showing metal data and (c) and (d) showing mold data on short and long time scales, respectively. Red curves denote measurements and black curves denote predictions.

steel shot mold proved to be a difficult material to drill when placing the TCs in the mold. The additional force used in drilling probably resulted in the drill bit wandering, and resulted in sensor positioning error for TC4. It was determined that the agreement with the measured metal TCs was more important to have than the overpredicted temperature at TC4.

Temperature-time plots for the steel shot sand mold mixed materials are given in Figures 53 and 54. Unfortunately, the metal sensor wires for the steel shot and chromite sand 50/50 mix material (Casting 4) TCs were burned by liquid steel splashing on them. Work then focused on determining mold properties resulting in excellent agreement with the mold TC measurements for Casting 4, which was clearly achieved as seen in Figures 53 (c) and (d). For the steel shot and zircon sand 50/50 mix material (Casting 5), the metal TC2 failed in a manner similar to TC1 in Casting 2, and resulted in lower than actual temperature measurements for TC2. Fortunately TC1

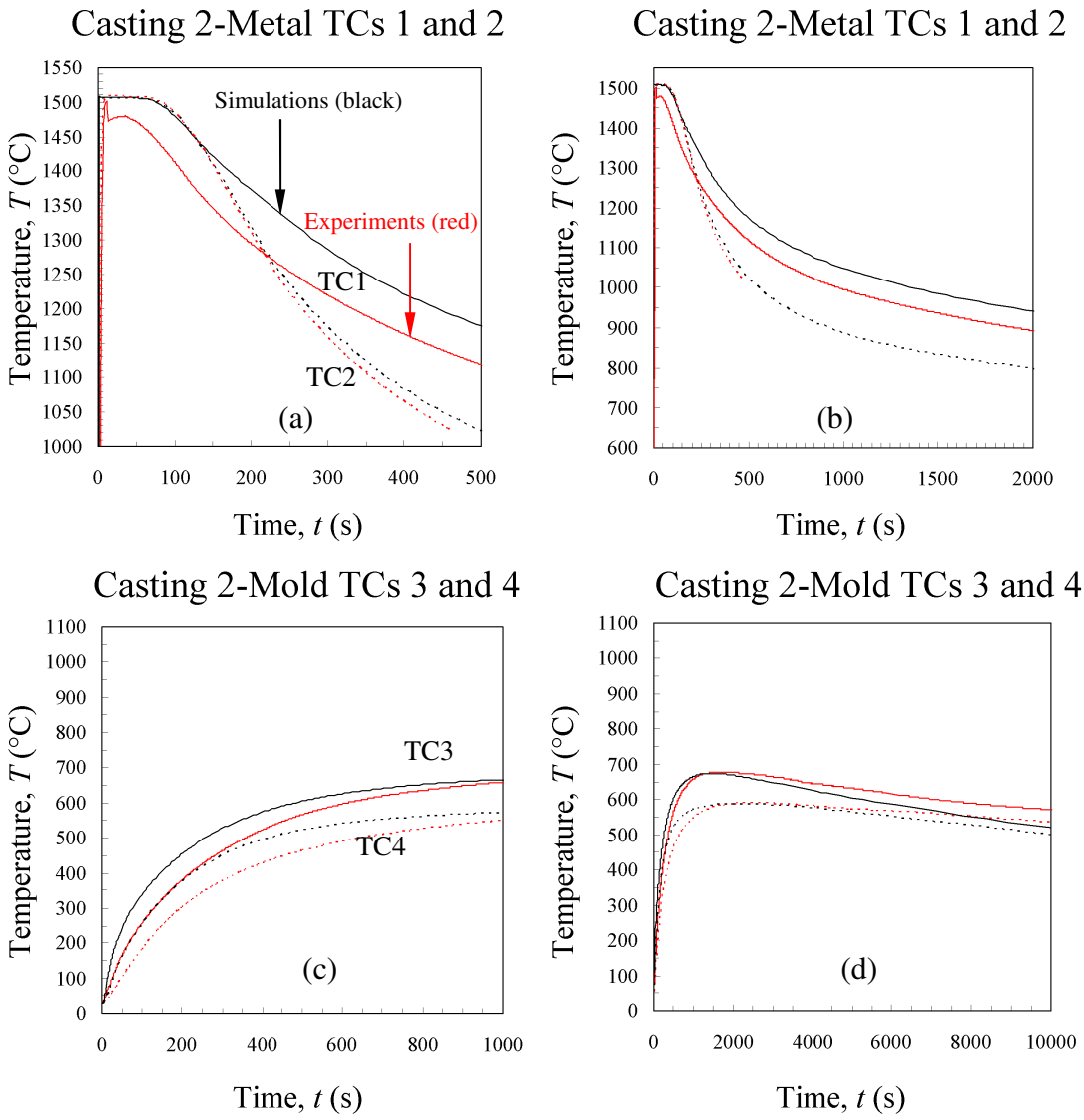

Figure 51 Measured and predicted TC data for solid chill mold experiment Casting 2 with (a) and (b) showing metal data and (c) and (d) showing mold data on short and long time scales, respectively. Red curves denote measurements and black curves denote predictions.

in Casting 5 survived long enough (about 400 second) to provide data that agrees well with the predictions as seen in Figures 54 (a) and (b). The mold properties determined for the steel shot and zircon sand 50/50 mix also result in good agreement with the mold measurements at TC3 and TC4 as seen in Figures 54 (c) and (d) with TC3 slightly over predicted.

The measured and predicted TC data for Casting 6 with drag having 1" facing mold of steel shot and backed by 50% of the area covered with 1" chills are shown in Figure 55. The metal TC data in Figure 55 (a) and (b) demonstrate good agreement with measurement. This agreement is supported as well by the behavior of the two TCs cooling behavior relative to each other. The measured and predicted TC2 data (dashed lines) in Figure 55 (a) and (b) initially cool slower than the TC1 data, but then at around 300 seconds the TC2 data crosses below the TC1

data. This behavior seems to be capturing that the chill's influence on the data at TC2 occurs later in solidification since it is positioned closer to the cope surface than the chilled drag side. Also the chills are effective early in the solidification process at TC1, but the proximity of the feeder to TC1 keeps it hotter later on in the process.

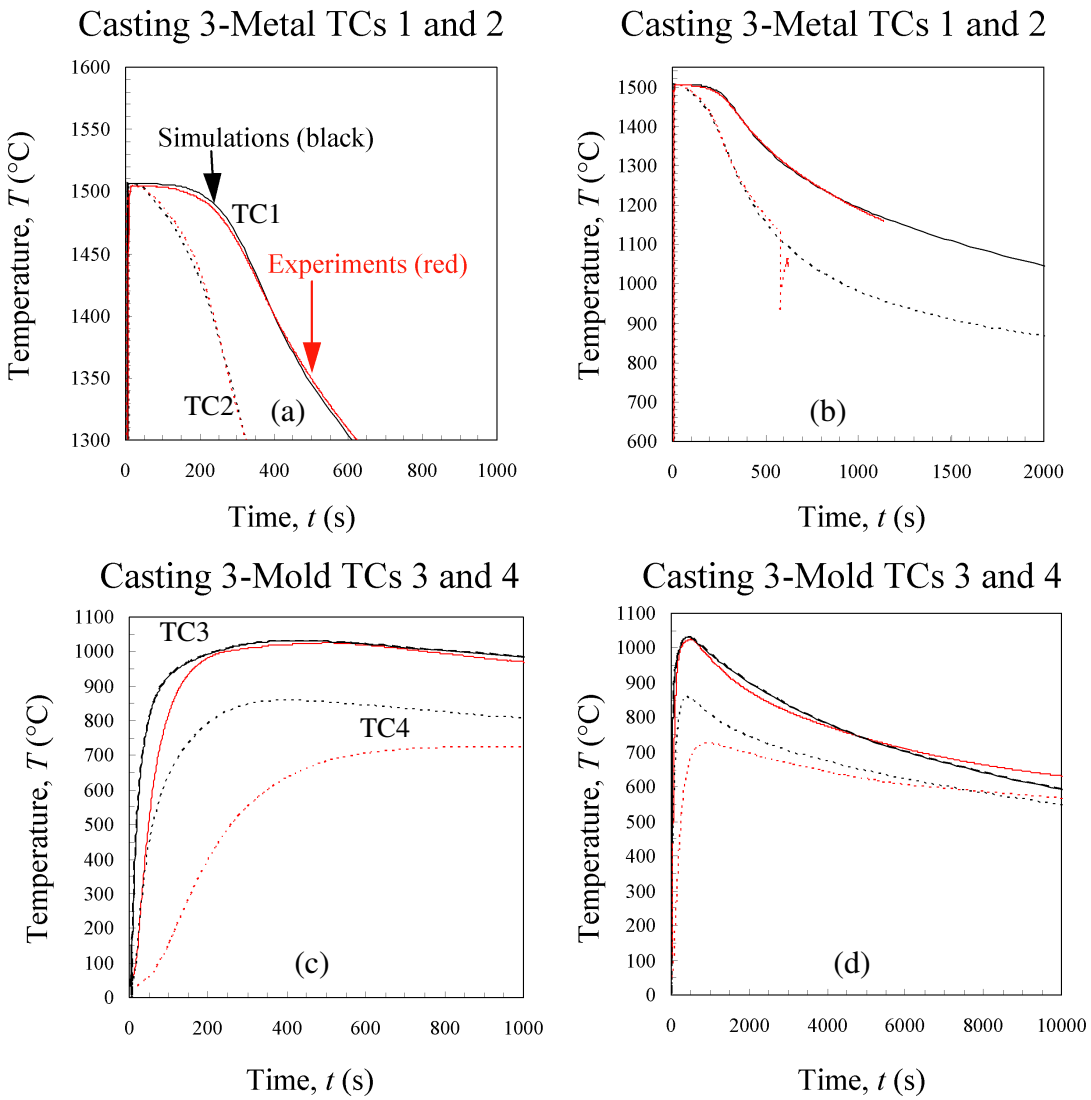

Figure 52 Measured and predicted TC data for steel shot drag mold experiment Casting 3 with (a) and (b) showing metal data and (c) and (d) showing mold data on short and long time scales, respectively. Red curves denote measurements and black curves denote predictions.

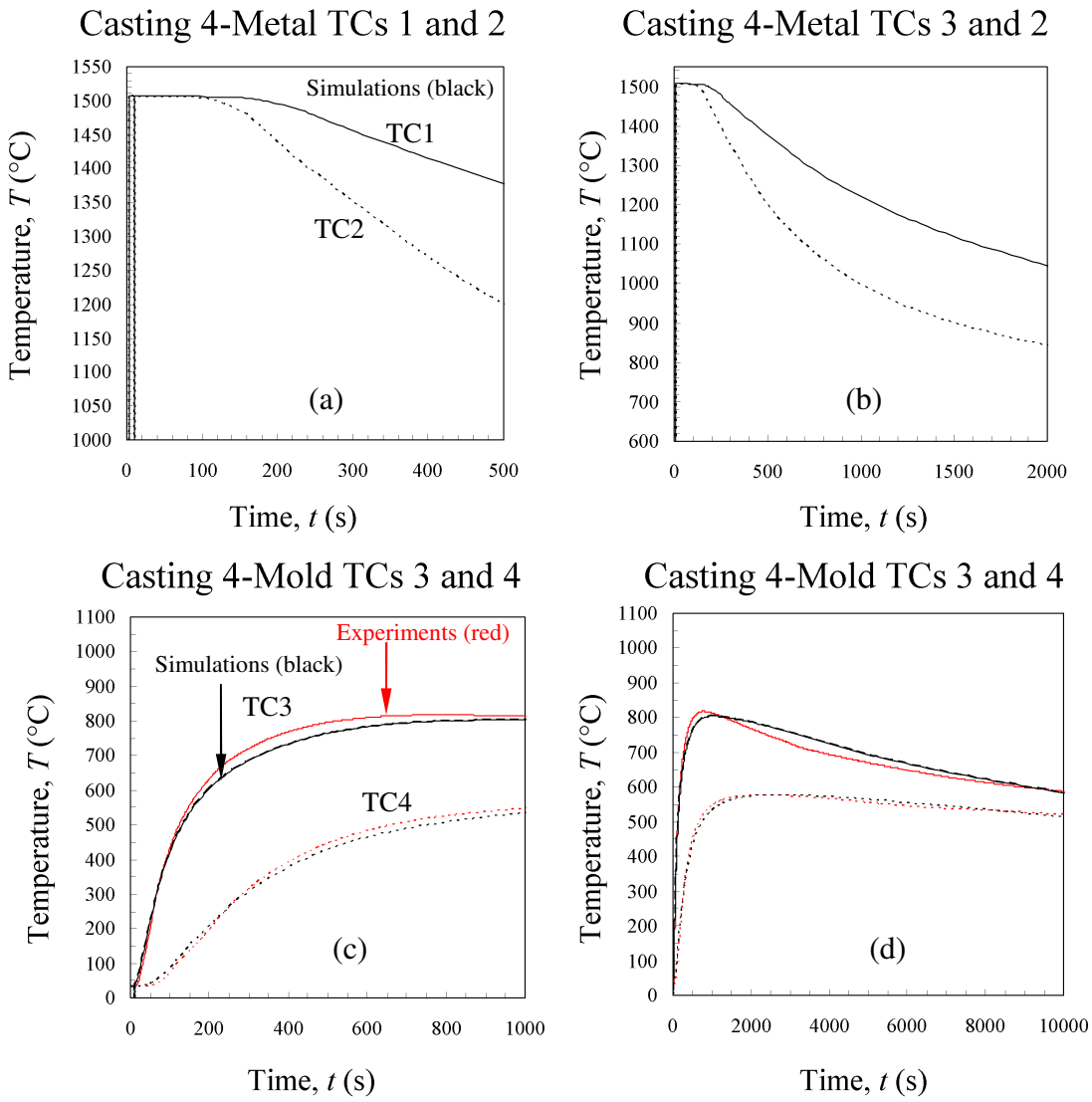

Figure 53 Measured and predicted TC data for steel shot and chromite sand 50/50 mix Casting 4 with (a) and (b) showing metal data and (c) and (d) showing mold data on short and long time scales, respectively. Red curves denote measurements and black curves denote predictions.

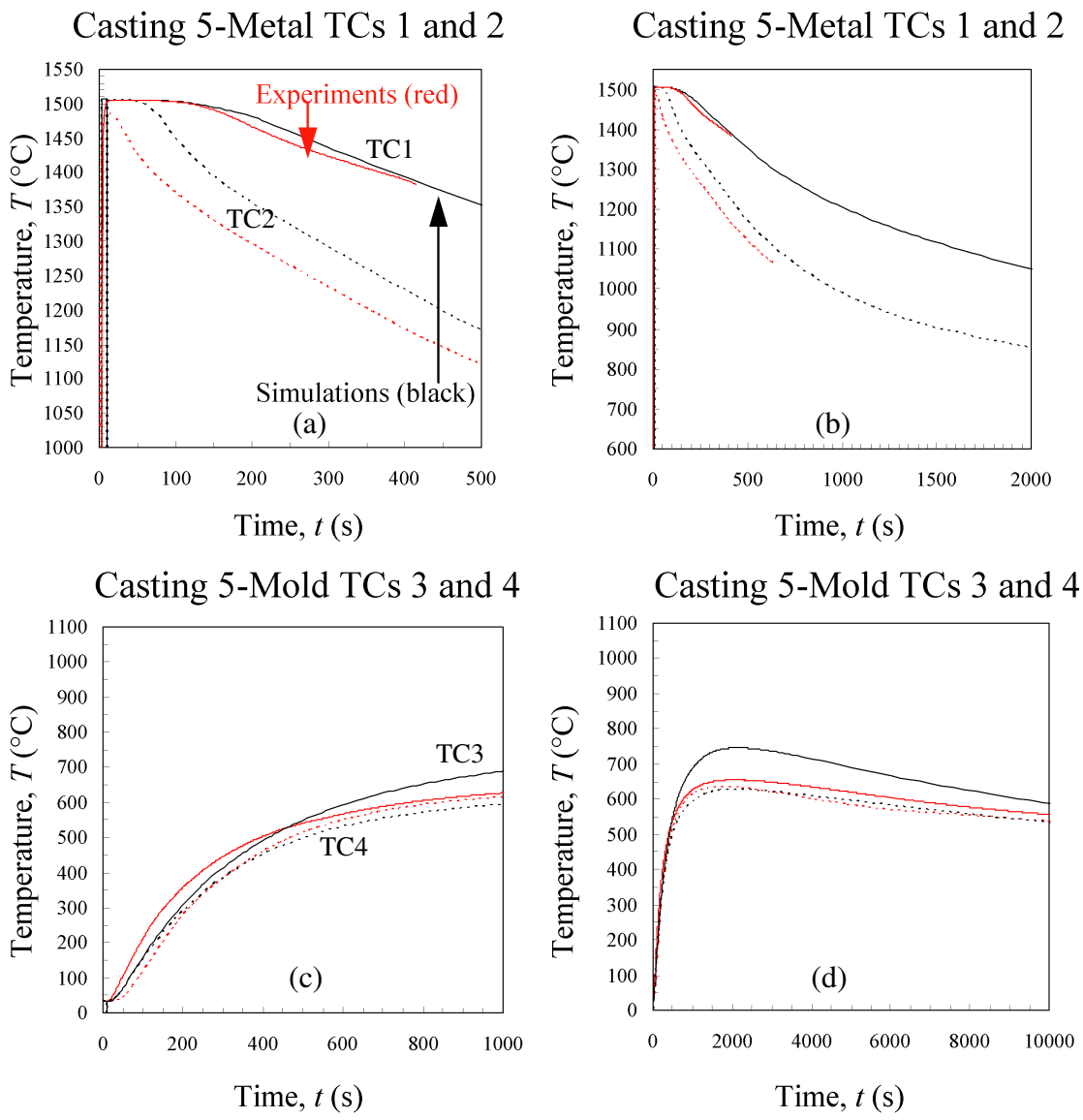

Figure 54 Measured and predicted TC data for steel shot and zircon sand 50/50 mix Casting 5 with (a) and (b) showing metal data and (c) and (d) showing mold data on short and long time scales, respectively. Red curves denote measurements and black curves denote predictions.

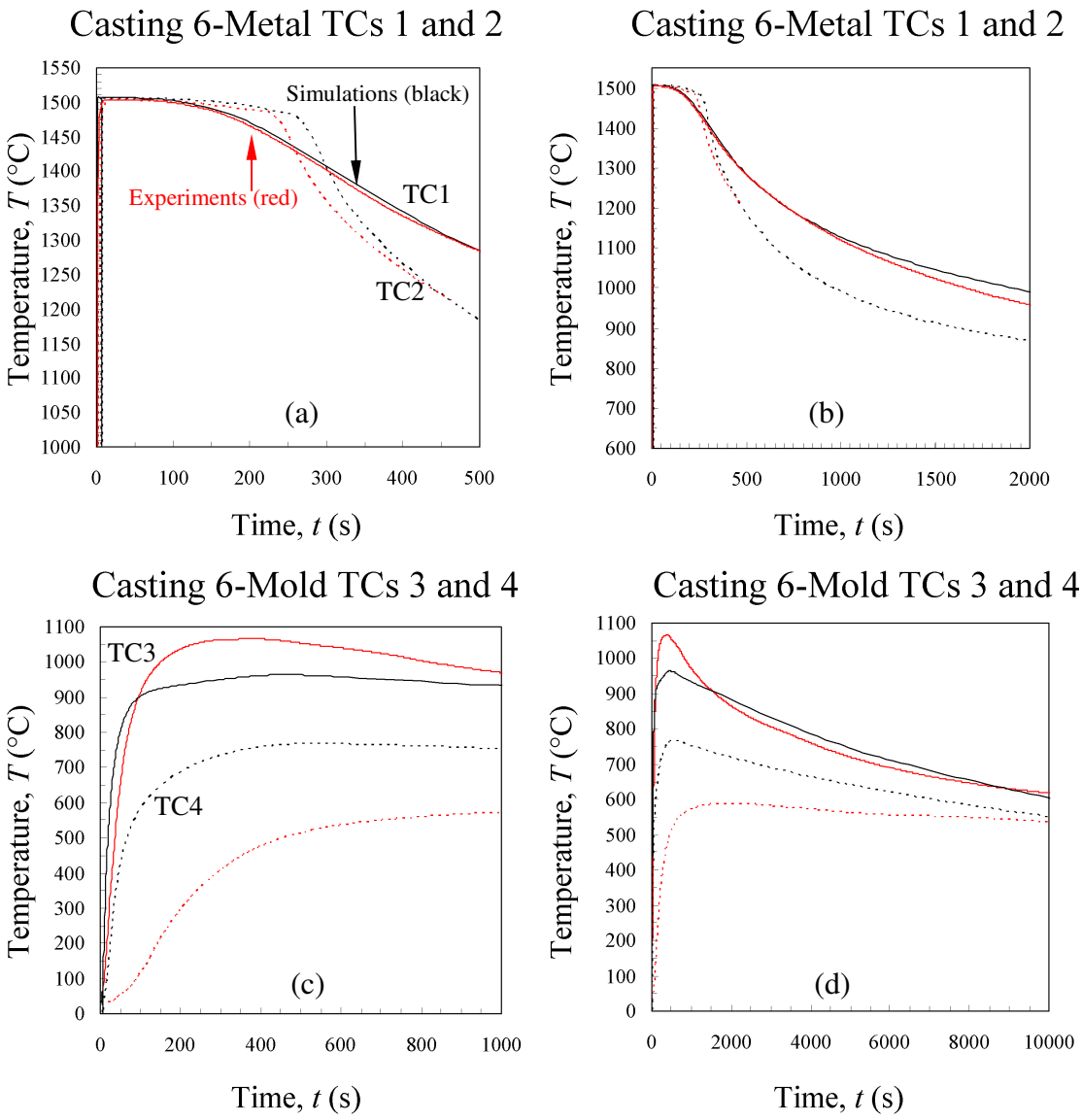

Figure 55 Measured and predicted TC data for Casting 6 with drag having 1" facing mold of steel shot and backed by 50% of the area covered with 1" chills. Note that (a) and (b) show metal data and (c) and (d) show mold data on short and long time scales, respectively. Red curves denote measurements and black curves denote predictions.

The temperature dependent chill and mold material properties determined by inverse modeling of the experiments are compared in Figures 56 and 57 using their thermal and heat diffusivity data, respectively. Thermal diffusivity is defined as the thermal conductivity k divided by the volumetric heat capacity (the product of density ρ and specific heat c_p). Thermal diffusivity is the ratio of material's thermal conductance to its ability to store heat energy for a given temperature change. It is a measure of the speed a thermal front will move through a substance. The thermal diffusivity plotted in Figure 56 show solid steel and steel shot to be the most effective materials at transporting heat through them. The heat diffusivity is the product $k\rho c_p$ and is a measure of the chill material's ability to exchange heat with the casting since it

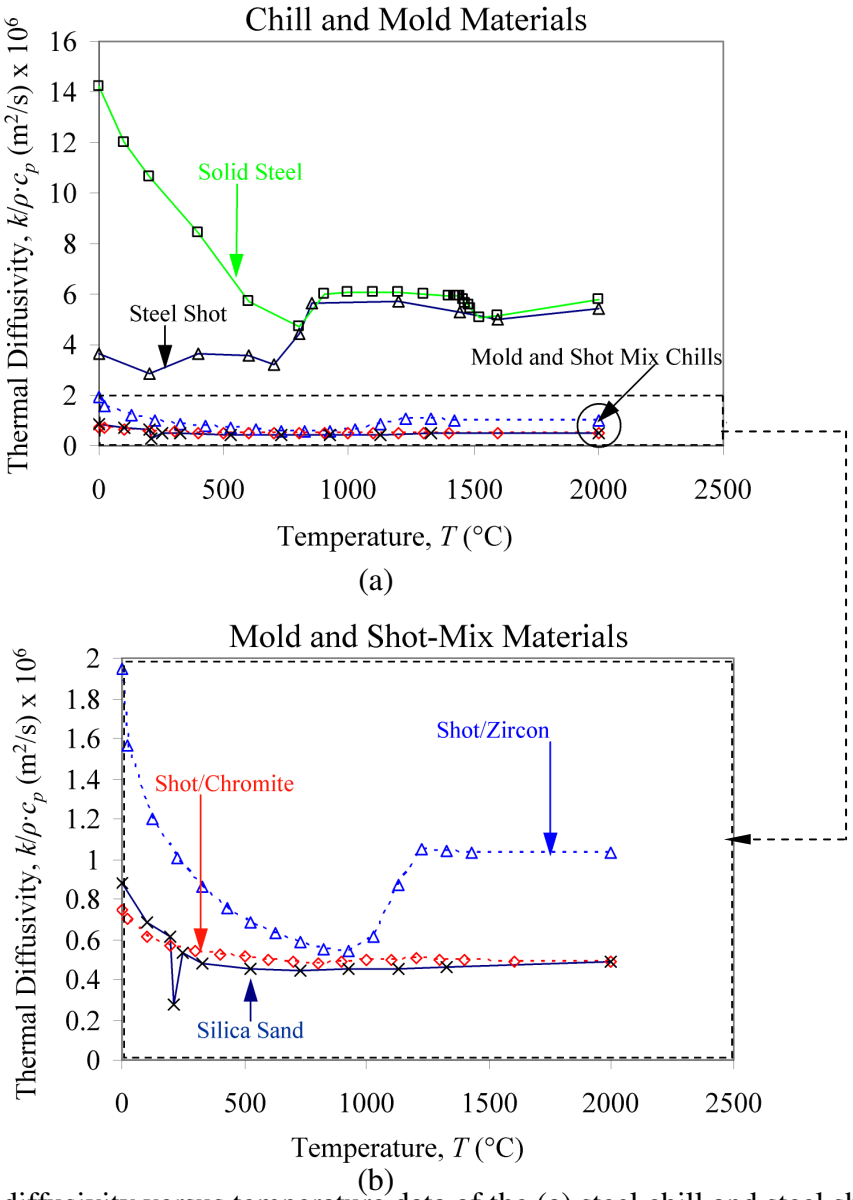

Figure 56 Thermal diffusivity versus temperature data of the (a) steel chill and steel shot, and (b) the silica mold and steel shot/sand mix mold materials determined from inverse modeling of the experiments.

combines the thermal conductance with the thermal storage capacity. From the heat diffusivity data in Figure 57, the steel shot is no more effective than the steel shot mixes. From Figure 56 and 57, solid steel should out perform all materials and the silica sand mold under perform all materials investigated regardless of the temperature ranges and conditions in the cooling of the casting. The temperature dependent heat transfer coefficients between the casting and mold or chill material found here to give the best agreement between measured and predicted temperatures are shown in Figure 58.

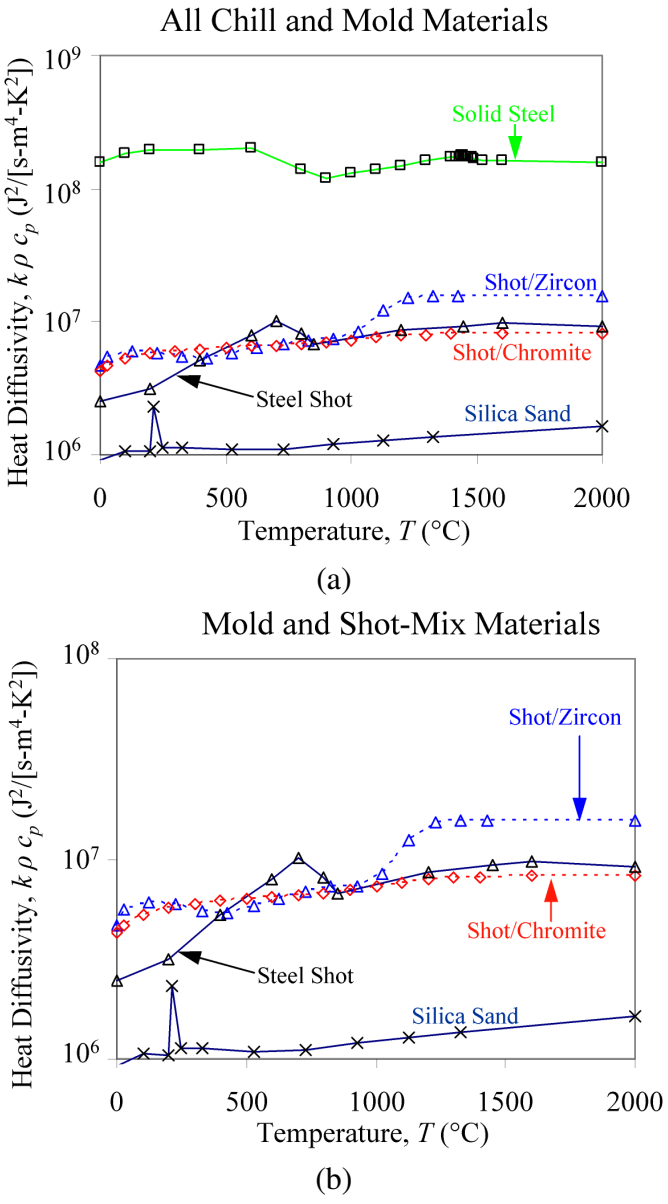

Figure 57 Heat diffusivity versus temperature data of (a) all chill and mold materials, and (b) the silica mold, steel shot and shot/sand mix materials determined from inverse modeling of the experiments.

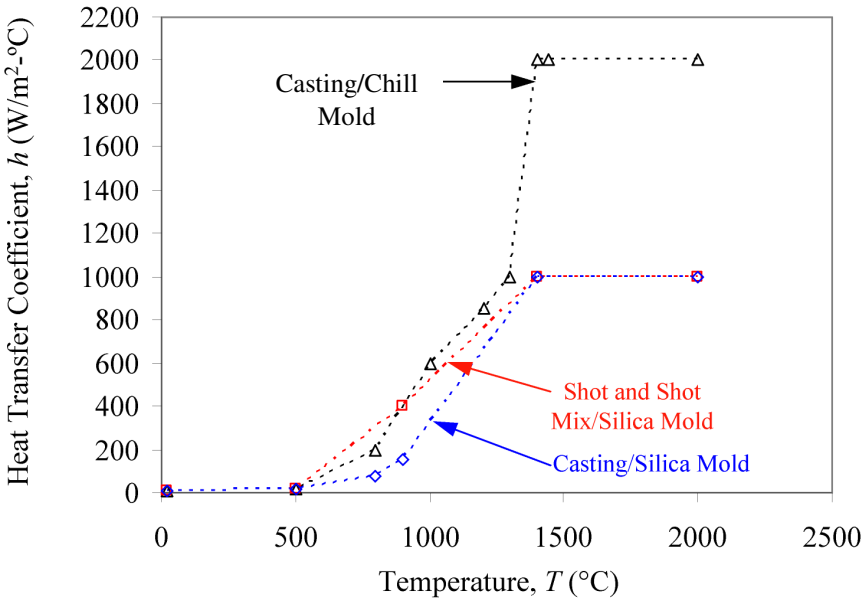

Figure 58 Temperature dependent heat transfer coefficients determined by inverse modeling to give best agreement with experimental temperature measurements for the silica mold, chill mold, and shot and shot/sand molds.

Using the temperature dependent properties, the relative abilities of the different mold material to increase solidification cooling rates in castings can be demonstrated using casting simulation. Also the ability of the mold materials to effect an improvement on the ductility of the high strength steel can be compared using Equation (3). The weld plate castings were used in this comparison of the effectiveness of the mold materials. The mold material in this study is used on the drag side of the plate with the rest of the mold taken as silica sand. The chromite and zircon mold properties used are from the *MAGMAsoft* database. As shown in Figure 59, the simulated thermocouple locations used in this mold material comparison study are under the feeder (see TC1 Figure 59 (a)) and at the mid-length of plate (see TC2 Figure 59 (b)). Unlike the experimental thermocouples, the positions virtual thermal couples TC1 and TC2 used in this mold material comparison study are unchanged for one mold material to the next. The cooling curves in the metal can be directly compared. Cooling curves at TC1 in Figure 59 (c) and at TC2 in Figure 59 (d) are given for the seven mold materials considered in this mold material study. The seven materials considered here are (in order of effectiveness in increasing the solidification cooling rate): steel chill (solid), steel shot, 50/50 mix of steel shot and zircon, 50/50 mix of steel shot and chromite (note the shot mixes are very close in performance with each other), zircon mold, chromite mold (note zircon and chromite are almost identical to each other), and silica sand mold. The silica mold has a noticeable drop off in chilling performance over zircon and chromite. It is also clear that using a 50/50 mix of shot and specialty sand can give a big boost in performance over specialty sands, and are nearly as good as using steel shot. The shot/sand mixes may offer practical advantages over using a mold made entirely from steel shot in terms of easier mold-ability and better surface finish. The steel shot beads tend to fuse with the casting surface. The steel shot mold materials have an advantage over the solid steel chills in that they can be molded to contour the casting surface, and they nearly perform as well as solid chills.

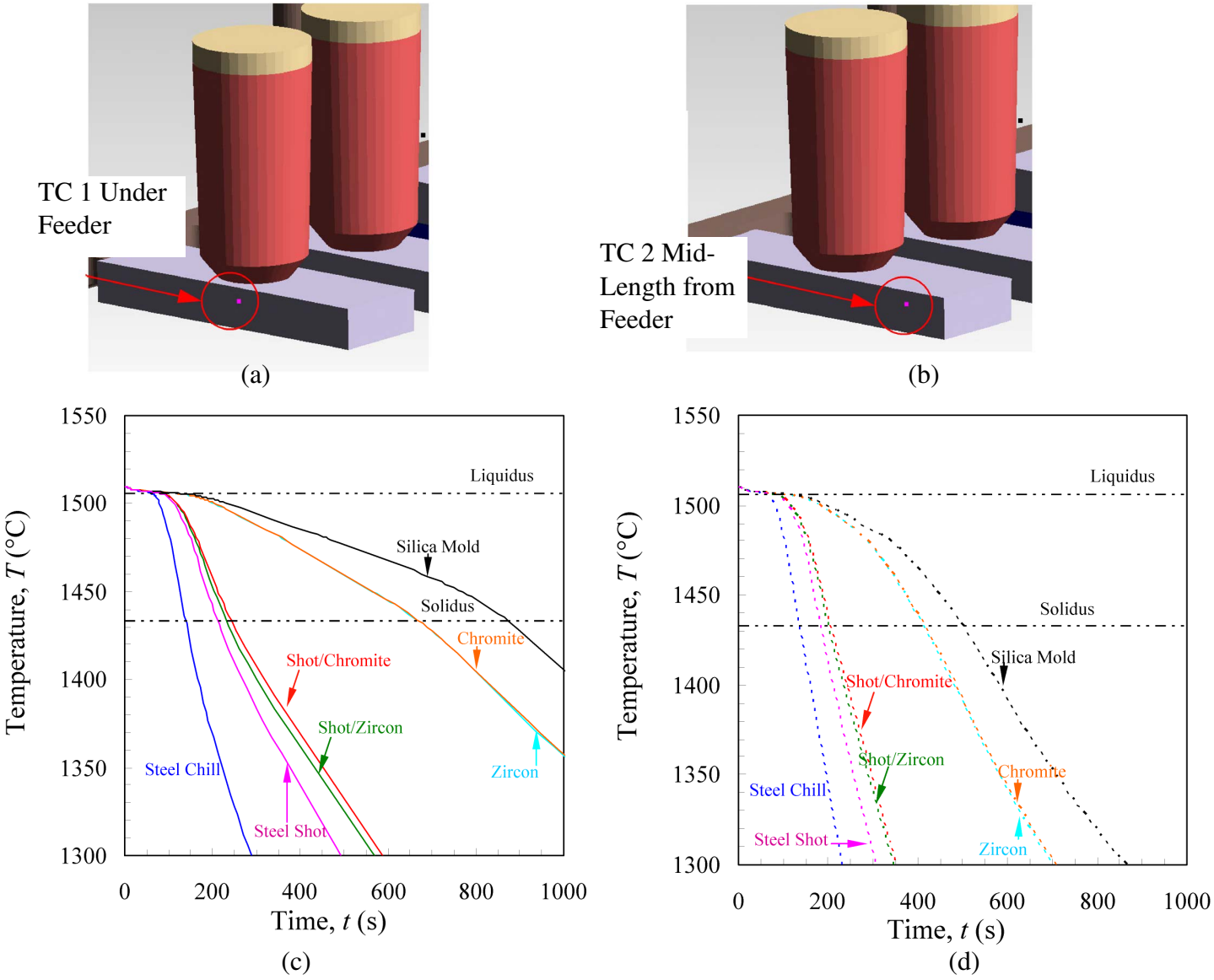

Figure 59 Thermocouple locations used in mold material comparison study, (a) under feeder TC1 and (b) at mid-length of plate TC2. Cooling curves at (c) TC1 and (d) TC2 for the seven mold materials.

The predicted solidification cooling rates and the predicted elongation to failure at the TC locations from Figure 59 are given in Figure 60. The biggest improvement in cooling rate over the silica mold is seen at TC1 for the solid chill where the cooling rate is increased nearly by a factor of 10, and at TC2 the comparison in cooling rate for these two materials shows an increase in cooling rate by a factor of 5. In terms of elongation, the silica mold has about 2.5% at TC1 and 4.5% at TC, and for the solid steel chill the elongation at both TCs is 10%. Because of the non-linear dependency of elongation with the cooling rate, the steel shot and steel shot mix mold materials have predicted elongations nearly at the level of the solid chill ranging from 8% to 9.25%. The elongation for the steel shot molds are 2 to 3 times the predicted elongation of the high strength steel cast in the silica sand mold.

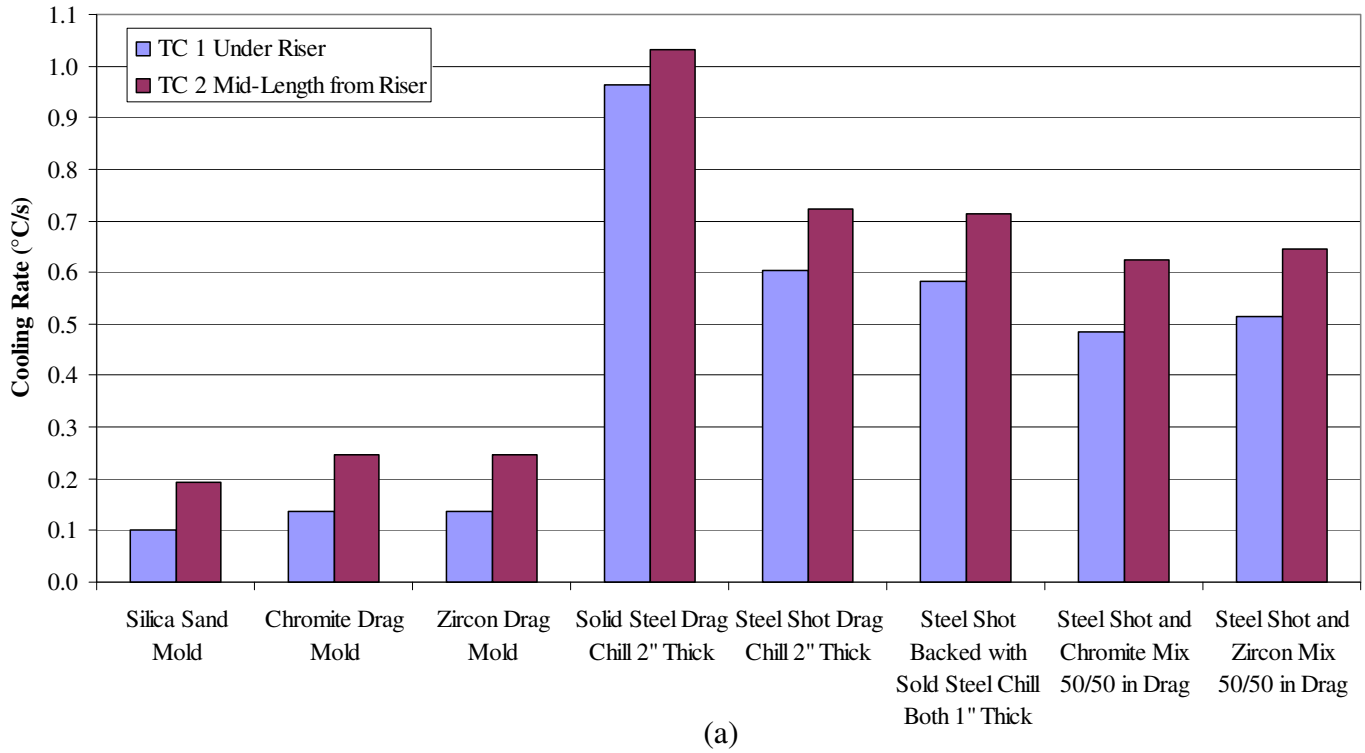

(a)

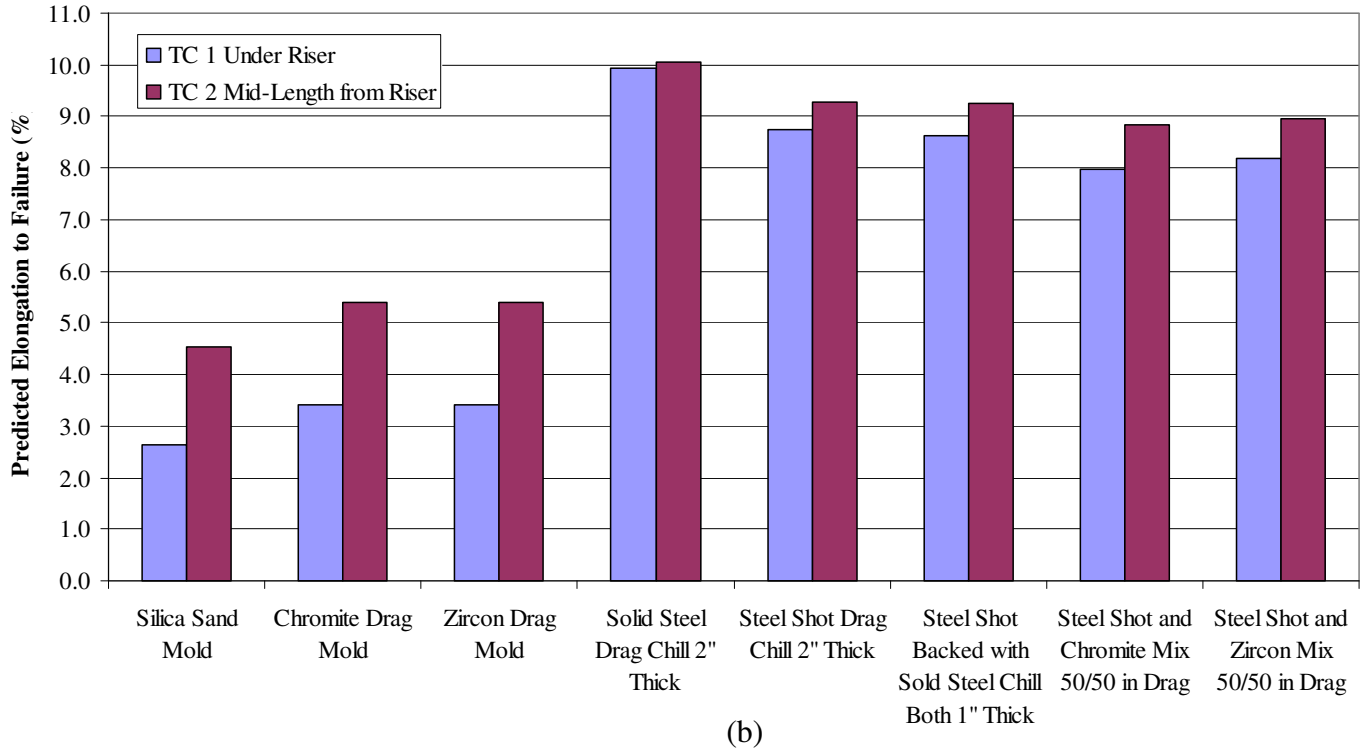

(b)

Figure 60 Effect of drag mold material on prediction of (a) cooling rate and (b) elongation at thermocouples under feeder (TC1) and mid-way to plate end (TC2) at the mid-thickness of a 2” thick plate section for a cast high strength steel.

Recall that both thermocouples TC1 and TC2 in this simulation study of mold materials are at the middle of the 2" thick plate. Cooling rates will increase and ductility will increase in material closer to the drag surface. It is envisioned that foundry engineers working with designers of high strength steel components can use steel chills and moldable sheet shot chill materials to improve ductility at key stress hot spots. Such highly stressed areas are usually at the surface of components where the chill can also have the greatest impact. There are always the conventional benefits of using chills; chills improve directional solidification and reduce porosity. Both effects will increase the load bearing and fatigue endurance capabilities of high strength steel castings.

Conclusions

Tensile and microscopy measurements on high strength steel specimens produced from casting trials and experiments show that its mechanical performance and ductility are dependent upon porosity level and cooling rate during solidification. After consideration of the variables influencing the mechanical performance of this high strength steel, ductility (as expressed by the elongation to failure) was identified as the key mechanical property responsible for limiting the material's performance. For the high strength steel used here, the data show that ductility is particularly sensitive to even relatively low levels of porosity for the high strength steel investigated, below 0.1%. The data also show that if an elongation to failure of 10% or greater is desired, the porosity should be limited to 0.04% or less. The effect of cooling rate on ductility was investigated. The tensile data specimen material were taken from castings produced over a range of solidification cooling rates, from 0.03 to 4 °C/s. Cooling rate versus tensile data indicate that a cooling rate of about 0.08 °C/s or greater results in acceptable ductility with an elongation of about 10% or greater. It is proposed that this results because of the finer microstructure and secondary dendrite arm spacing (SDAS) of less than 100 μm. There may be a size-effect such as discussed regarding Figure 1 (b) where larger pore sizes result in more damage under a given load for a given average porosity level. This suggests a possible influence of cooling rate on pore size distributions for a given porosity level. However, there is insufficient data here to shown whether the microstucture could be influencing or providing a limitation on the pore sizes in the distribution of microporosity. Micro X-Ray computed tomography (CT) was performed on four specimens and those results suggest this as a possibility.

After image analysis is performed on the CT data, the microporosity distributions were visualized. Clearly from Figures 28 to 30, the appearance of the porosity size distributions can be quite different at similar average porosity levels. The specimens in those figures correspond to foundry casting trial material with little or no control of the cooling rate. In order to investigate relationships between cooling rate, SDAS, porosity level and pore size distributions on tensile properties, specimens cast with more control of solidification cooling rates are needed, in addition to additional tensile data and accompanying CT data that includes pore size characterization. Here, the CT data was processed to yield quantitative data on the cross sectional porosity distribution along the specimen gage lengths. Analysis of this gives the porosity in the fractured regions of the specimen as 30% to 63% greater than the overall specimen average porosity. Ductility measurements did show a strong trend of increasing

ductility with decreasing porosity measured using CT. The results that even a small increase in average CT measured porosity can reduce the ductility. As shown in Table III, CT measured porosity levels of 0.04%, 0.05% and 0.08% give elongation to failures of 13%, 10% and 7%, respectively.

Solidification cooling rate was identified as the most important variable affecting elongation that can be accurately predicted in casting simulation. Therefore, an elongation to failure prediction based on the cooling rate was developed. The prediction of elongation from casting simulation is a valuable tool in casting process design when using this high strength steel in components where superior performance is needed. The casting process can be optimized to have material with the best possible mechanical performance where it is structurally required.

To provide a means for increasing cooling rates and better control of solidification conditions, temperature dependent chill and mold material properties are determined by inverse modeling of casting experiments. Properties are determined and compared for: solid steel chills, molds made from steel shot, steel shot mixed 50/50 by volume with chromite sand, and steel shot mixed 50/50 by volume with zircon sand, and silica sand mold as the baseline for comparison. A study was performed predicting the ability of the mold materials to increase cooling rate and the resulting ductility. The results from the study show that for a 2" thick casting section, and at a point at the mid-thickness of the section for comparison, it is found that for this high strength steel the resulting elongation to failure for the various mold materials are: 2.5% for silica mold, 10% for solid steel chill, 8.75% for steel shot mold, and 8% for the steel shot/specialty sand mixes. It is envisioned that foundry engineers working with designers of high strength steel components can use steel chills and moldable sheet shot chill materials to improve ductility at key stress hot spots. Such highly stressed areas are usually at the surface of components and these are areas where chills can have the greatest impact on improving mechanical performance.

Acknowledgements

This work has been supported under the Steel Founders' Society of America (SFSA) program on Casting and Advanced Steel Technology that has been funded by the Army Research Laboratory under the provisions of cooperative agreement W911NF-12-2-0033. The authors gratefully acknowledge Professors Robin Foley, John Griffin and Charles Monroe at the University of Alabama-Birmingham for performing the wedge casting experiments, providing temperature data from them for modeling validation, and performing optical microscopy measurements for the data presented and analyzed here. The authors also gratefully acknowledge Mr. Terrell Webb and Professor David Van Aken at the Missouri University of Science and Technology (MS&T) for providing measurements and data from their ASPEX SEM imaging system that are also presented here. For their execution of the steel shot mold material casting trials and allowing us to successfully record the necessary temperature data, authors gratefully recognize Bradken-Atchison and in particular our point of contact there for the trials, Mr. Travis Unzicker.

References

1. Van Aken, D. C., Webb, T. O., Foley, R. D. and Griffin, J. A., "Porosity and Cleanliness Limitations on High Strength Steels," in *Proceedings of the 69th SFSA Technical and Operating Conference*, Paper No. 5.5, Steel Founders' Society of America, Chicago, IL, 2015.

2. Hardin, R.A., and Beckermann, C., "Effect of Porosity on Deformation, Damage, and Fracture of Cast Steel," *Metall. Mater. Trans. A*, Vol. 44A, 2013, pp. 5316-5332.

3. Wang, Q. G, "Microstructural Effects on the Tensile and Fracture Behavior of Aluminum Casting Alloys A356/357," *Metall. Mater. Trans. A*, Vol. 34A, pp. 2887-2899, 2003.

4. Ceschini, L., Morri, A., Morri, A., and Pivetti, G., "Predictive Equations of the Tensile Properties Based on Alloy Hardness and Microstructure for an A356 Gravity Die Cast Cylinder Head," *Materials and Design*, Vol. 32, pp.1367–1375, 2011.

5. Osorio, W. R., Goulart, P. R., Santos, G. A., Neto, C. M., and Garcia, A., "Effect of Dendritic Arm Spacing on Mechanical Properties and Corrosion Resistance of Al 9 Wt Pct Si and Zn 27 Wt Pct Al Alloys," *Metall. Mater. Trans. A*, Vol. 37A, pp. 2525-2538, 2006.

6. Shabani, M. O. and Mazahery, A, "Prediction of Mechanical Properties of Cast A356 Alloy as a Function of Microstructure And Cooling Rate," *Archives of Metallurgy and Materials,* Vol. 56, Num. 3, pp. 671-675, 2011.

7. Turhal, M. S. and Savaskan, T., "Relationships between Secondary Dendrite Arm Spacing and Mechanical Properties of Zn-40Al-Cu Alloys," *Journal of Materials Science*, Vol. 38, pp. 2639 – 2646, 2003.

8. Bannantine, J. A., Comer, J. J. and Handrock, J. L., *Fundamentals of Metal Fatigue Analysis*, Prentice Hall, Englewood Cliffs, N.J., pp. 124-135, 1990.

9. Hardin, R.A., and Beckermann, C., "Prediction of the Fatigue Life of Cast Steel Containing Shrinkage Porosity," *Metall. Mater. Trans. A*, Vol. 40A, 2009, pp. 581-597.

10. Foley, R. D., Griffin, J. A., and Monroe, C. A., University of Alabama-Birmingham, SFSA research program communication.

11. Van Aken, D. C., and Webb, T. O., Missouri University of Science and Technology, SFSA research program communication.

12. Carlson, K.D., and Beckermann, C., "Prediction of Shrinkage Pore Volume Fraction Using a Dimensionless Niyama Criterion," *Metall. Mater. Trans. A*, Vol. 40A, pp. 163-175, 2009.

13. Won, Y.M. and Thomas, B.G., "Simple Model of Microsegregation during Solidification of Steels," *Metall. Mater. Trans. A*, Vol. 32A, pp. 1755–1767, 2001.

14. Rasband, W.S., *ImageJ*, U. S. National Institutes of Health, Bethesda, Maryland, USA, http://imagej.nih.gov/ij/, 1997-2016.